Electron-vibron effects in interacting quantum dot systems

DISSERTATION

zur Erlangung des
DOKTORGRADES DER NATURWISSENSCHAFTEN (DR. RER. NAT.)
der Fakultät für Physik
der Universität Regensburg

vorgelegt von
ABDULLAH YAR** aus **EIDAK,
NWA, KPK, PAKISTAN
im July 2012

Electron-vibron effects in interacting quantum dot systems

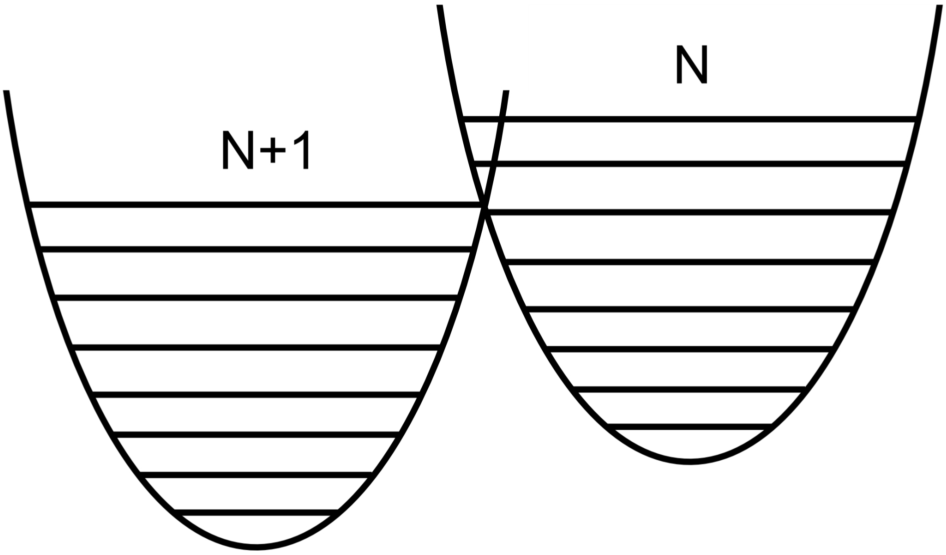

DISSERTATION

Promotionsgesuch eingereicht am:	18.01.2012
Die Arbeit wurde angeleitet von:	Prof. Dr. Milena Grifoni
Prüfungsausschuß:	
Vorsitz:	Prof. Dr. Dominique Bougeard
Erstgutachten:	Prof. Dr. Milena Grifoni
Zweitgutachten:	Prof. Dr. Klaus Richter
	Prof. Dr. Tilo Wettig
Datum des Promotionskolloquiums:	17.07.2012

Contents

Chapter 1

Introduction

In this chapter, the general concepts and various aspects of nanoelectromechanical systems (NEMS) are introduced. We briefly highlight NEMS as recent emerging suitable candidates for a host of potential applications in nanotechnology and fundamental science. We then focus on the transport properties, hysteretic behavior, spectrum and Franck-Condon couplings of particular kinds of NEMS. The focus and the structure of the thesis is outlined at the end of this chapter.

1.1 NEMS

> "If you have nanoelectromechanical systems [NEMS]
> with mobile parts, the Casimir force will be attractive,
> and the parts will stick together," R. Decca

On 29th December 1959, Richard P. Feynman held his famous talk at an American Physical Society meeting at Caltech "There's Plenty of Room at the Bottom" [1] which later on motivated the very conceptual foundations of nanotechnology. Some of the ideas discussed in his visionary talk clearly suggest the important role of manipulating the mechanical degree of freedom at the nanoscale. Consequently, NEMS based systems have been of considerable interest in the area of nanotechnology. NEMS can be realized in a variety of different flavors, e.g, with single molecule junctions [2–6], suspended and laterally confined two dimensional electron gases [7], silicon [8], or suspended graphene [9]. NEM devices exploit the interplay between electrical and mechanical degrees of freedom at nanoscale. This characteristic feature makes them interesting both from technological applications and fundamental research point of view. These systems also exhibit pronounced quantum mechanical effects such as zero point motion [10]. Because of their very high mechanical frequency, they can be used in a new form of mechanical computers. From the fundamental science point of view, they can serve as useful tools to probe directly the basic laws of quantum mechanics. In general, nanoelectromechanical systems have very high mechanical quality factors (Q-factor) normally in the range of $10^3 - 10^5$, remarkably higher than those of electrical resonant circuits [11]. These attributes make them prospective candidates for promising technological applications such as ultrafast sensors, extremely sensitive mass and position detectors, actuators, optical switches, turning mirrors, regulating electric current devices, and signal processing components. Out of the broad range of potential applications of nanoelectromechanical systems in various fields, we outline a few which are more relevant to the findings of this thesis.

1.1.1 Nanoscale resonator

Nanoscale resonators are small size devices that oscillate at high frequencies with many potential applications [12–14]. Here we present a carbon nanotube based resonator which was experimentally demonstrated by Steele *et al.* [15]. The device consists of a suspended carbon nanotube connected to two metallic leads and capacitively coupled to a gate electrode as shown in Fig. 1.1. In operation, the nanotube is excited into mechanical oscillation by applying an ac voltage to a nearby antenna. The resonance frequency of the tube is tuned with a gate voltage. The electric field created by the gate electrode pulls the nanotube toward the gate, increasing its length which produces more tension in the tube. Consequently, the nanotube starts to oscillate, populating the bending mode. It was observed in the experiment that the dc current through the tube is influenced by the resonator motion. This effect is a hallmark of electron-vibron interaction that can strongly affect the transport properties of nanoelectromechanical systems. Another visible evidence of such an interaction is that a shift in resonance frequency was observed in the measurement of frequency-voltage characteristics. This shift can only occur if an extra electron tunnels to the nanotube which can be detected in a quite high quality factor range, typically, when it exceeds 10^5. Moreover, mechanical damping and unusual nonlinear mechanical behavior were also observed in the experiment which can be associated with a transfer of energy to electrons in the tunneling event. All these effects clearly show that mechanical and electrical degrees of freedom are strongly coupled in NEM devices.

1.1.2 NEM memory cell

The experimental realization of this device was achieved by Jang *et al.* [16]. The device consists of a source, drain and a gate electrode as sketched in Fig. 1.2. From the source electrode, a vertically aligned multiwalled carbon nanotube (MWCNT) with a certain diameter was grown and coated with a dielectric layer of $\mathrm{SiN_x}$ and a metal layer of Cr to engineer a CNT-insulator-metal (CIM) capacitor. As a working principle, the source is electrically grounded, while the drain and gate electrodes are connected to a constant positive voltage such that the gate is at higher voltage than the drain. When the setup is provided with a positive bias, the carbon nanotube on the drain experiences a repulsive electrostatic force from the gate electrode since both are at positive voltage and an attractive force from the source lead. As a result, the nanotube bends until it makes contact with the metallic lead on the capacitor, see Fig. 1.2(b). During the contact, a transient current flows from the nanotube at the drain to the CIM capacitor and consequently the transferred charge can be used to

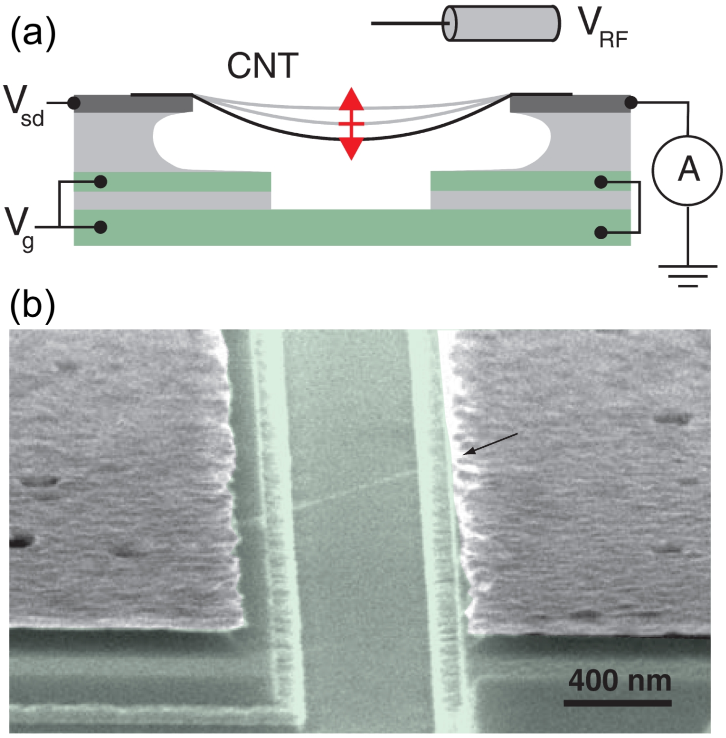

Figure 1.1: (a) Schematic diagram of a high-Q mechanical resonator based on suspended carbon nanotube. It can be driven into oscillation by applying a periodic radio frequency potential to a nearby antenna. The resonator motion is detected by its influence on a dc current through the nanotube. (b) Electron micrograph of the device where the arrow specifies the position of the nanotube. This figure is taken from [15].

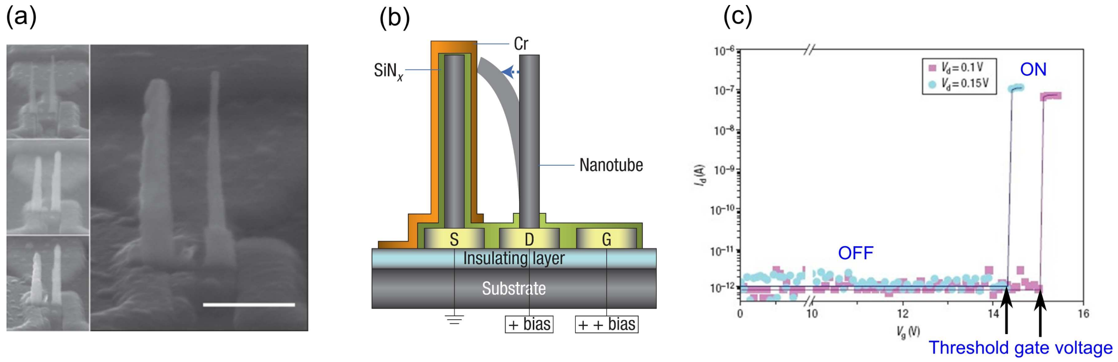

Figure 1.2: Schematic representation of NEM memory device. (a) Scanning electron micrographs. (b) NEM switched capacitor structure based on vertically aligned multi-wall carbon nanotubes. (c) Current-voltage characteristics of the memory setup. This figure is taken from [16].

store some information. In the absence of gate voltage, the electrostatic force which is responsible for the deflection of the drain MWCNT vanishes and the nanotube comes back to the vertical aligned configuration and thus exhibits 'OFF' state. In this way, a carbon nanotube based switched capacitor structure defines excellent 'ON' and 'OFF' states. NEM devices are suitable candidates for memory applications due to their well-defined 'ON-OFF' states and fast switching dynamics. The switching speed of the device is characterized by the natural oscillating frequency of the MWCNT on the drain electrode which is significantly high because of the large Young's modulus of rigidity of CNTs. A closer analysis of the I-V characteristics of this memory device reveals that the current between source and drain increases sharply above a threshold voltage and then becomes saturated, see Fig. 1.2(c). This very sharp sub-threshold slope indicates that a very small difference in voltage can switch the device between 'ON' and 'OFF' states leading to low power consumption. This characteristic feature makes NEM memory devices attractive for technological applications.

1.1.3 Quantum shuttle device

The shuttle device is a particular kind of NEMS which has an oscillating object of nanometer size that transfers electrons one-by-one between source and drain electrodes. One such device can be a single-molecule transistor as shown in Fig. 1.3 which was experimentally produced by Park *et al.* [5]. The C_{60}-molecule was placed between two gold electrodes using a break junction technique. The entire setup is in turn placed on a SiO_2 insulating layer on top of a doped silicon wafer functioning as a gate electrode, see Fig. 1.3(a), which controls the electrostatic potential of the C_{60} molecule. The operation of the device can be based on the centre-of-mass oscillation of the C_{60} molecule within the Lennard-Jones like confinement potential that binds it to the gold surface as depicted in Fig. 1.3(b). Such a potential can be well approximated by a harmonic potential near the equilibrium position. Electron transport can occur through the device if a bias voltage is applied between the source and drain contacts. Thus an extra electron tunneling from the source to the C_{60}-molecule compresses the C_{60}-surface bond due to the interaction between the C_{60} ion and its image charge induced on the metal surface. The C_{60}-molecule comes back to equilibrium position upon tunneling of the electron out to the drain electrode and consequently the molecule is set into oscillation. The vibrational excitations can be readily observed in the I-V characteristics. The mechanism involved in this process basically mimics a Franck-Condon process that usually occurs in electron-transfer and light-absorption processes in molecules where the vibrational excitations are induced by electron tunneling to or off the molecule [17]. It turns out that on one hand, this scientific achievement provides an evidence of strong coupling between the mechanical and electrical degrees of freedom in NEM devices. On the other hand, the existence of quantized nano-mechanical oscillations (excitations) of the C_{60} molecule against the gold surface observed in the experiment justifies the law of quantum mechanics regarding the existence of discrete energy levels at nanoscale.

Another experimental realization of a quantum shuttle device was achieved by Erbe *et*

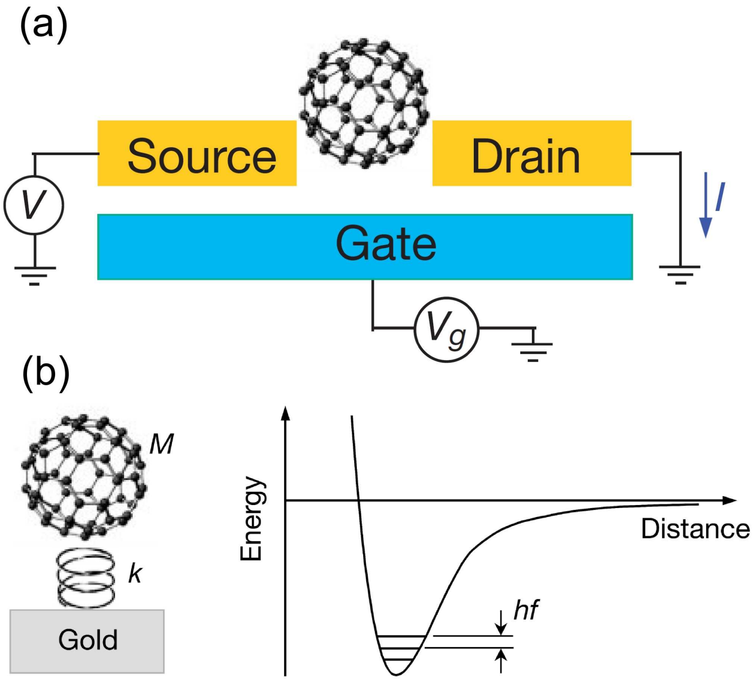

Figure 1.3: (a) Sketch of a single-C_{60} transistor. (b) Typical presentation of the centre-of-mass oscillation of a C_{60} molecule used in the experiment by Park *et al.*, where the molecule is considered as a body of mass M attached to a spring with spring constant k. On the right, the confinement potential that binds the C_{60} molecule to the gold surface which can be well approximated by a harmonic potential near the equilibrium position, and the corresponding quantized nano-mechanical excitations with energy hf are shown. This figure is taken from [5].

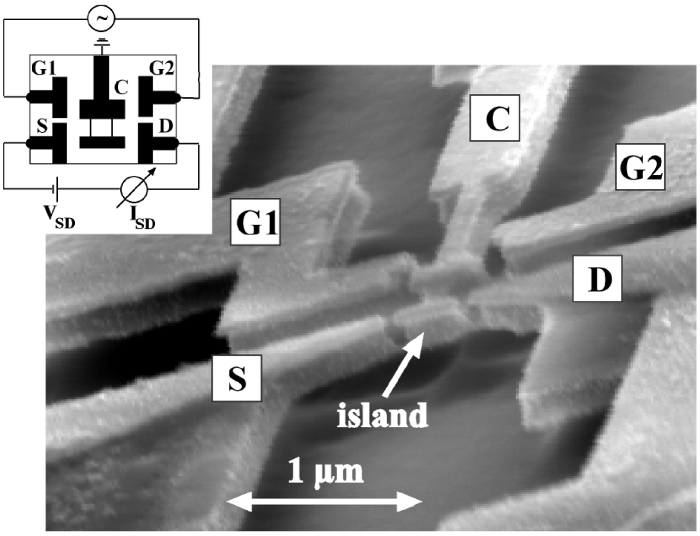

Figure 1.4: Electron micrograph and schematic circuit diagram (inset) of a nanomechanical quantum shuttle device. The cantilever can be set into back and forth motion by applying an ac voltage to the two driving gates G1 and G2. Electrons can be shuttled from source (S) to drain (D) through the island on top of the cantilever if a bias voltage is applied across the leads. This figure is taken from [18].

al. [18]. The device consists of a quantum island on top of a cantilever between source and drain contacts as depicted in Fig. 1.4. The island is electrically kept isolated from the rest of the grounded cantilever which is capacitively coupled to two driving gates G_1 and G_2 as shown in the inset of Fig. 1.4. The cantilever can be set into oscillations if an ac voltage is applied to the gates and consequently the island comes alternatively close to the source (S) and drain (D) leads and thus allows the electron transport through the island. Upon applying a bias voltage across the leads, a current can be driven through the device. It was detected in the experiment that resonant mechanical motion can be excited if the frequency of the driving voltage coincides with the eigenfrequency of the cantilever. In this situation, the current through the device exhibits distinct features which can be observed in the I-V characteristics. These are the main vibrational signatures reported in this experiment. Hence, this experimental achievement also sheds light on the fact that vibrational modes significantly affect the electronic transport due to electron-vibron interaction.

1.2 NEMS in molecular electronics

Molecular electronics deals with the study of electronic and thermal transport characteristics of circuits in which single molecules or their combination are used as basic building blocks [19]. These novel molecular building blocks in turn can, for example, serve as switches, gates, rectifiers or memory elements for many important applications. From the fundamental science point of view, molecular electronics opens a new area of research to study the conduction mechanisms at the smallest scale, where the physics is entirely dominated by quantum mechanical effects. The small size features of molecular circuits in combination with other interesting electrical, mechanical, thermal, and optical properties can lead to many new physical phenomena. In addition, molecular junctions can be used to probe fundamental aspects of electron transfer.

From a technological perspective, molecular electronics proposes to use molecules as basic elements for a wide variety of potential applications. NEMS are emerging as strong candidates for intriguing applications in nanotechnology and fundamental science due to their remarkable electrical and mechanical properties. It turns out that based on their promising features, NEMS can give rise to a new revolutionary field of research in molecular electronics.

1.3 NEMS attributes in spintronics

Spintronics is a recent emerging field of science that exploits the spin degree of freedom in addition to conventional electronics. An interesting aspect in spintronics would be to engineer a memory-storage device based on spin manipulation. The investigation of spin manipulation in quantum dots and single molecules is also at the core of experimental [20,21] and theoretical [22] physics in the field of spintronics. Experimentally, spin states of single atoms and molecules have been studied by using different techniques, e.g., spin-polarized scanning-tunneling spectroscopy [23,24]. Such experimental achievements have inspired controlled switching of the spin states of a single electron by the application of an external voltage. This leads to single-spin memory effects. Another possibility of single-spin manipulation may be achieved via NEMS, based on the interplay between charge, spin, and vibron degrees of freedom. The combination of polaron-memory mechanism and spin-dependent tunneling leading to a single-spin memory effect was even proposed in a recent work [25]. Due to their novel properties, NEMS are expected to serve as active candidates for spin-memory characteristics in spintronics.

1.4 Thesis outline

This thesis is organized as follows: In the first part, we discuss the transport theory of interacting quantum dots in the stationary limit. More precisely, in Chapter 2, we develop a non-equilibrium transport theory for a generic quantum dot weakly coupled to metallic leads using a density matrix approach. We derive a Generalized Master Equation (GME) that describes the dynamics of the quantum dot system. We analyze in detail the rate equations, populations of the many-body states, and current that govern the dynamical properties of the system. Chapter 3 is dedicated to the transport properties of a generalized Anderson-Holstein model system, where a single molecular level is coupled to many vibrational modes. We investigate gate asymmetry and negative differential conductance (NDC) features. We also derive the conditions to explain the NDCs effects.

In the second part (Chapter 4) of this thesis, we investigate the transport characteristics in a polaron model system in the nonstationay limit where memory effects can be observed. Particularly, bistability of the many-body states, quantum switching and hysteretic behavior of the system are explored. A time-dependent master equation is solved and the necessary conditions based on time scales are discussed. The DC-case is presented as a special case of the time-dependent master equation where the effect of asymmetric voltage drop across the leads will be examined.

In the third part, the band structure, vibrational modes, spectrum and Franck-Condon couplings of single wall carbon nanotubes (SWCNTs) are discussed. This part is organized such that in Chapter 5, the electronic band structure of armchair metallic single wall carbon nanotubes is introduced. The wave function of electrons and Hamiltonian of the noninteracting armchair SWCNTs at low energy is presented. The different possible vibron modes are also discussed. A low-energy theory of interacting suspended SWCNTs quantum dots in the weak tunnel coupling regime is developed in Chapter 6. In particular, we investigate the dependence of the spectrum and Franck-Condon factors on the geometry of the junction in the presence of several vibronic modes. We also analyze the selection rules for the excitations of different plasmon-vibron modes via electronic tunneling processes. Diagonalization of the system Hamiltonian and the resulting Franck-Condon couplings will be presented. Finally, the conclusions are drawn in Chapter 7.

Part I
Transport theory of interacting quantum dots

Chapter 2

Vibration-mediated transport theory of quantum dots

Quantum transport through nanoscale devices has gained a considerable interest in the recent years. On one hand, interesting features in the current voltage characteristics like Coulomb blockade, spin blockade, Kondo effect, negative differential conductance or Franck-Condon effects associated with different kinds of excitations that can be of electronic or vibrational nature have been studied extensively by different experimental and theoretical approaches. On the other hand, bistability, quantum switching and memory effects are investigated in nanojunctions. The study of transport properties provides not only the transport mechanism but also the detail of the spectrum of eigenstates of the system. Several experimental approaches are used to probe the electronic structure and transport properties of molecules and quantum dots, e.g., scanning tunneling microscopy [26,27], electromigration technique [28,29], mechanically controllable break junctions technique [30–32]. Similar to the wide variety of such experimental techniques, many theoretical approaches for the study of transport properties in quantum dot systems are used in the scientific community. One promising numerical approach to study the electronic structure and quantum transport in nanostructures is the ab initio density functional theory (DFT) method combined with nonequilibrium Green's function techniques [19, 33–36]. This technique provides valuable information about the electronic structure, vibrational frequencies, atomization energies, ionization energies, electric and magnetic properties, molecule and lead-molecule interface structure, etc. In particular, it is appropriate to study quantum transport when the central system is strongly coupled to the lead contacts. Another theoretical approach commonly employed to the description of tunneling through the molecules and quantum dots is based on the Generalized Master Equation (GME) for the reduced density operator of the dot. This technique works very well when the quantum dot is weakly coupled to the electrodes via tunnel barriers. In this approach, the time evolution of the many-body states of the dot is taken into account, while the effects of the leads are integrated out by taking a trace over the lead degrees of freedom. This approach is appropriate to treat exactly the strong interactions on the quantum dot. This technique is the focus of this work which will be explained in more detail. In the following we

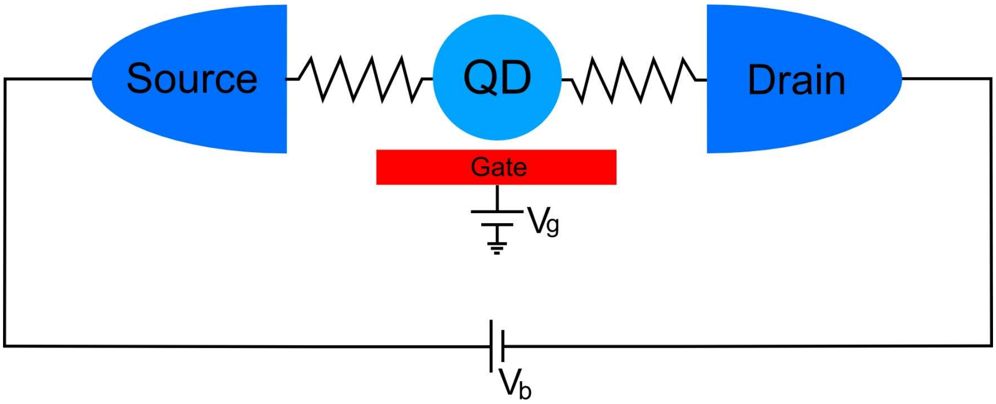

Figure 2.1: Schematic diagram of a quantum dot setup. Source and drain contacts are weakly coupled to the dot via tunnel junctions, the latter being coupled to a vibrational mode. The electrostatic potential of the dot is modulated by a capacitively coupled gate electrode.

introduce the essential dynamical factors that play a significant role in the quantum transport mechanism.

2.1 Quantum dots

In this chapter, we introduce the concept of quantum dots and analyze briefly the transport theory of these devices. A quantum dot is a small electronic island where the electron dynamics is confined in all three spatial directions leading to significant quantum mechanical quantization effects. Interestingly, in this size regime, the system dimension is comparable or even smaller than the phase coherence length of the intrinsic charge carriers [37–39]. Due to the ultra-small length scales, the Coulomb interaction between the electrons gets importance and can give rise to many intricate effects in the transport characteristics of a quantum dot system [40–42]. Moreover, quantum dots are extremely sensitive to the influence of vibrational modes. They couple to vibrational degrees of freedom and show several striking effects as observed in many experiments [43–45]. Quantum dots are characterized by a discrete vibrational spectrum, exhibiting pronounced signatures in the current-voltage characteristics of nanojunctions [46]. Different kinds of quantum dot setups have been realized in many ways, for instance, semiconductor dots manufactured by submicron fabrication techniques, carbon nanotubes, nanoparticles, metal particles or even small organic molecules. Upon coupling a quantum dot to electrodes via tunnel barriers, a current can be driven through the device if a finite voltage is applied across the source and drain contacts. Quantum dot setups provide potential opportunities to explore the internal electronic structure of complex systems. It is important because the electronic transport characteristics strongly depend on the energy spectrum as well as on the structure of the dot eigenstates. In this chapter, we present a short review of the electronic structure and transport properties of a generic interacting quantum dot system coupled to vibrational mode. To proceed further, in the following we discuss the general aspects of nanoelectromechanical quantum dot systems.

2.2 Electron-vibron interaction effects

The electronic transport is strongly influenced by vibrational modes in nanoelectromechenical systems due to the coupling between mechanical and electrical degrees of freedom [47–49]. A detailed analysis of quantum transport theory reveals that one can identify different regimes for electron-vibron interaction where various vibrational signatures are expected to be observed. More detail can be found in [19, 50] and references therein. Based on the relative coupling between electronic and vibronic degrees of freedom, the transport phenomena can be classified into one of the three distinct regimes: (a) weak coupling, (b) intermediate coupling, and (c) strong coupling.

In the weak electron-vibron coupling regime, a small inelastic current is induced by the vibrational modes that basically constitutes corrections to the elastic current. In particular, this inelastic current shows well-defined signatures at energies of the vibrational modes associated with neutral molecules inside the nanojunctions. In this limit, the tunneling time is much smaller than the time that an electron requires to interact with a vibrational mode. In this situation, the electron-electron Coulomb interaction is usually treated within the framework of a mean field level approach and a perturbative expansion is made in the electron-vibron interaction.

In the intermediate electron-vibron coupling regime, transient polarons are generated on the junction. However, dephasing is not fast enough and consequently a simple kinetic description of the problem cannot be performed. In this coupling limit, the approximation of lowest-order expansion (LOE) in the electron-vibron coupling constant does not work and needs further improvement of the perturbation theory to include higher order terms in the expansion. To solve this problem, many different theoretical approaches are used in the scientific community. One standard approach is the self-consistent Born approximation (SCBA) [51–55] where the lowest-order Feynman diagrams are taken into account in the LOE by considering the full Green's functions. However, in this approach important contributions of some higher-order diagrams like vertex corrections are neglected in summing up certain diagrams up to infinite order. Hence, it works well rather in the weak electron-vibron coupling limit. Another approach is the unitary polaron transformation [56] in the single-vibron model [52,57,58]. This transformation is employed to decouple the electron-vibron interaction Hamiltonian which renormalizes the electronic coupling elements. The renormalized electronic coupling contains then the effects of electron-vibron interaction to all orders. However, this approach is appropriate for rather strong electron-vibron coupling.

In the strong electron-vibron coupling regime, vibrational effects can dominate the transport properties of molecular nanojunctions. For example, for moderate values of the electronic coupling to the leads, the electron-vibron interaction can give rise to pronounced current steps in a resonant situation. These current signatures can provide very useful spectroscopic information on the vibrational modes associated with the molecule in different charge states. The impact of vibrons on the transport properties increases with both the electron-vibron coupling and the time that electrons reside in the molecular quantum dots. The former factor cannot be easily controlled, while the latter one is easy to tune via the length of the dot or the dot-electrode coupling. In other words, in the weak tunnel coupling limit, the electrons on the dot have enough time to interact strongly with vibrational modes giving rise to the polaron formation which is basically a mixed state where an electron is dressed by a vibronic cloud [56]. Thus in the weak tunnel coupling regime, the transport is dominated by the Coulomb blockade effects, while the electron-vibron coupling leads to the appearance of sidebands in the I-V characteristics [43,45]. All the above mentioned approaches can successfully explain many vibrations induced effects, like the appearance of vibron sidebands, which is the principal vibrational signature in resonant transport processes. However, all these reported different theoretical approaches are approximate and the exact description of vibrational effects in the transport calculations for arbitrary strength of the electron-vibron interaction remains an open issue for further research, at least in nonequilibrium situations. There are other factors which play an important role in determining the effects of vibronic modes on the transport characteristics of quantum dots. For example, temperature crucially affects the transport mechanism. Low temperature favors the coherent transport through quantum dot systems, whereas high temperature significantly increases the occupation probabilities of vibronic states leading to a strong reduction of the inelastic scattering length and thus makes the transport completely incoherent [19, 50]. The length of the dot is another important factor that has significant impact on the transport properties of quantum dots, with longer dots favoring incoherent transport.

2.3 Sequential tunneling and Coulomb blockade

Sequential tunneling is a quantum mechanical phenomenon which corresponds to a transfer of a single electron onto or out of the quantum dot. A typical setup for this process consists of metallic source and drain contacts with a continuous density of states weakly coupled via tunneling junctions to a quantum dot with discrete energy spectrum. In addition, the quantum dot may be be coupled to vibrational mode as shown in Fig. 2.1. In order to modulate the electrostatic potential of the dot and hence control the average number of electrons, the dot is capacitively coupled to a gate electrode. In this thesis, we focus on gate controlled sequential transport across quantum dots of nanoelectromechanical systems in the weak tunnel coupling regime. In this limit, electrons can tunnel between the dot and the leads in such a way that the time between two consecutive tunneling events is large compared to the duration of a tunneling event so that the number of electrons on the dot is well defined. In the weak tunnel coupling regime, a perturbation theory in the tunneling amplitude between the quantum dot and electrodes is appropriate in electronic transport. In particular, such a perturbative treatment is valid if the tunneling-induced level width $\hbar\Gamma$ is small compared to the thermal energy $k_\mathrm{B}T$ of the system. The lowest order in this expansion leads to sequential tunneling. It is also known from transport theory that sequential tunneling is dominant as long as the dot electrochemical potential is located between the Fermi energies of the leads. The tunneling process satisfies Pauli exclusion principle and energy conservation. When a tunneling event takes place, the charge on the quantum dot abruptly changes by a quantized amount $e = -1.60217646 \times 10^{-19}\ C$.

The corresponding change in the Coulomb energy can be conveniently described in terms of the capacitance of the dot. Such a capacitance C can be associated with a quantum dot within the framework of the constant-interaction model (appropriate for weakly tunnel coupled quantum dots) if the details of the involved many body processes are ignored. An additional charge changes the electrostatic potential of the quantum dot by the charging energy $E_C = \frac{e^2}{C}$. The charging energy becomes very important when it exceeds the thermal energy $k_\mathrm{B}T$ of the system. Particularly, at low temperature, i.e., $E_C \gg k_\mathrm{B}T$, the transport characteristics of the quantum dot are significantly influenced by the charging energy. If the tunnel coupling of the central system to the electrodes is weak enough such that the wave function of the electrons is entirely localized inside the dot, then the number of charge particles on the dot is quantized. It means that the quantum fluctuations in the number of electrons due to tunneling events through the barriers are small compared to the time scale of the measurement. In this situation, the number of electrons on the dot can only be changed by tunneling of a single electron onto or out of the dot. That is why a quantum dot device is usually called single electron transistor (SET) [59] because the underlying transport mechanism can be described in terms of single electron tunneling events. Thus a SET setup always contains a definite integer number of electrons. At fixed gate voltage V_g, tunneling of an electron onto the dot is allowed only if the charging energy is compensated by the applied external bias voltage. The transport process can be easily understood if the dynamics is described in terms of the electrochemical potentials of the leads and dot as sketched in Fig. 2.2. The leads are considered to be in thermal equilibrium and relax very fast into the equilibrium state after a tunneling event. Tunneling of an electron can take place if a transport channel is available in the bias window. For this purpose, a bias voltage V_b is applied across the source and drain contacts which induces a difference in their electrochemical potentials. Defining the electrochemical potentials of source and drain electrodes as μ_s and μ_d, respectively, we follow the convention, $\mu_\mathrm{s} > \mu_\mathrm{d}$, with $\mu_\mathrm{s} = \mu_\mathrm{d} + eV_\mathrm{b}$. The electrochemical potential of the quantum dot μ is determined by N, the number of electrons on the dot, and is modulated by an external gate voltage. For simplicity, if the energy spectrum of the electron eigenstates in the dot is taken continuous, the addition of an electron on the dot changes μ by E_c, i.e.,

$$\mu(N+1) = \mu(N) + E_c. \tag{2.1}$$

Tunneling of an electron onto the dot occupied by N electrons can occur only if the condition

$$\mu_\mathrm{s} > \mu(N+1) \tag{2.2}$$

is satisfied. Similarly, tunneling out of the dot in the charge state $N+1$ to the drain is possible if the condition

$$\mu(N+1) > \mu_\mathrm{d} \tag{2.3}$$

is fulfilled. The resulting condition for an electron to tunnel from source to the dot and then to the drain reads

$$\mu_\mathrm{s} > \mu(N+1) > \mu_\mathrm{d}. \tag{2.4}$$

In this situation, a transport channel is available and current can flow through the device. In a similar way, the cycle is repeated and the charge transport through the quantum dot can be obtained as observed in the experiments. Thus the conditions described by Eqs. (2.2) and (2.3) lead to two threshold straight lines in each dot resonance situation in a bias-gate plane, separating regions of suppressed current from those with finite current. For a sequence of resonances such that the dot is filled with different number of electrons, one gets generically a diamond-shaped pattern as shown in Fig. 2.3, traditionally known as stability diagram. However, if the above conditions are not satisfied, then the dot resides in a stable charge state and charge transport is forbidden. In this case, the system is said to be in Coulomb blockade. The diamond-shaped regions are conventionally called Coulomb diamonds. It follows that inside the diamond, transport is blocked. The electrochemical potentials of the electrodes and the quantum dot in blockade and resonance situations are presented in Fig. 2.2. Moreover, the excitations corresponding to vibrational modes appear as excitation lines running parallel to the Coulomb diamond edges which can be viewed as vibrational sidebands, see Fig. 2.3. In each line, a new vibronic excited state enters the bias window, creating an additional transport channel. It appears as a step-wise increase of the current and a corresponding peak in the differential conductance. The transport characteristics of a quantum dot system are significantly influenced by two characteristic energies $\hbar\Gamma$ and $k_\mathrm{B}T$. Particularly, the line widths in the plot of differential conductance are characterized by the larger one of these energies. Indeed, in the Coulomb blockade regime it should be the second one [19, 39]. It implies that sharp transition lines and thus accurate spectroscopic information about the structure of the system can be obtained at low temperatures and in the weak tunnel coupling regime.

2.4 Discrete energy spectrum

Based on finite size, quantum dot exhibits discrete energy spectrum. For the observation of charging effects and discrete energy spectrum, an important energy scale is the energy level spacing ΔE, i.e., the separation between the discrete energy states of the quantum dot. In order to resolve these levels, the spacing must be much larger than the thermal energy $k_\mathrm{B}T$. Temperature also plays an important role in the energy levels quantization of the system. Thus depending on the charging energy E_c and level spacing ΔE, one can find the following different regimes [39]:

1. $E_c \ll k_\mathrm{B}T$: In this regime, one cannot observe the effects arising from the discrete nature of the energy spectrum.
2. $E_c \gg k_\mathrm{B}T \gg \Delta E$: This is usually known as the classical Coulomb blockade regime because Coulomb oscillations can be observed. In more detail, upon sweeping the gate voltage V_g, the build up of the induced charge will be compensated in periodic intervals by tunneling of discrete charges onto the quantum dot from the leads. Such a competition between continuously induced charge and discrete compensation leads to the so-called Coulomb oscillations which can be readily observed in the measurement of the current or differential conductance as

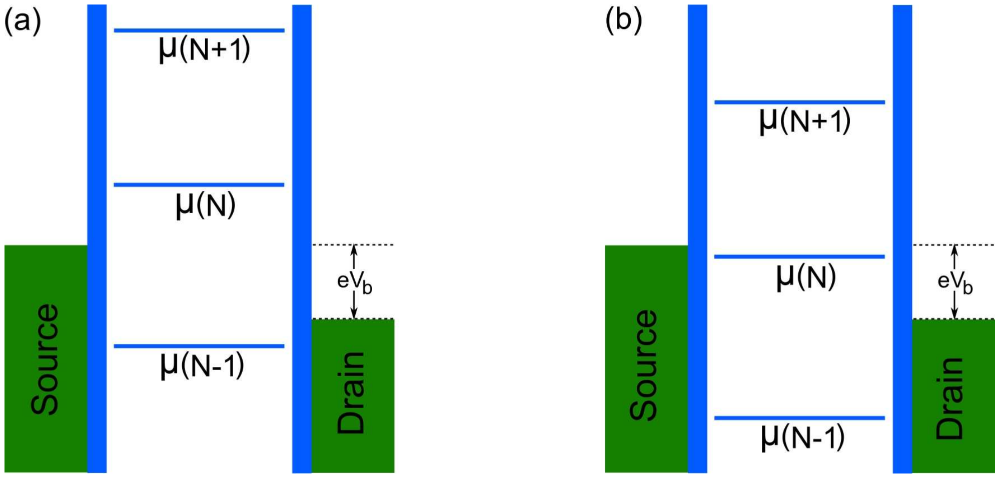

Figure 2.2: Schematic representation of the electrochemical potential profiles of the leads and of a generic quantum dot. The dot is characterized by a spectrum with quantized levels. The electrochemical potentials of the levels are measured with respect to the Fermi energy of either electrode (source or drain) in the absence of external bias voltage. The source electrochemical potential is denoted by μ_{s}, whereas the drain by μ_{d}. (a) Coulomb blockade situation where the N-particle electrochemical potential of the quantum dot is not in the transport window between μ_{s} and μ_{d}. (b) A situation where sequential tunneling of an electron from source to drain can occur by adjusting the gate voltage such that the electrochemical potential of the dot comes into the transport window.

a function of gate voltage at fixed bias (source-drain) voltage. However, thermal fluctuations can smear out the effects arising from the discrete energy levels.

3. $E_c, \Delta E \gg k_{\mathrm{B}}T$: This is the so called quantum Coulomb blockade regime. In this regime, both the charge and energy level quantization can be observed. In this thesis, we will focus on this regime.
4. $E_c, \Delta E \gg \hbar\Gamma$: Such a discretization depends on the coupling of the dot to the electrodes. The energy excitation spectrum can only be resolved if the above condition is fulfilled.

2.5 Franck-Condon blockade

This kind of blockade in the I-V characteristics appears in quantum transport through interacting quantum dots as a manifestation of electron-vibron interaction. The conclusions of various experimental results show that electron-vibron interaction has profound consequences on the transport characteristics of quantum dot systems [43–45]. The differential conductance as a function of gate and bias voltage is shown in Fig. 2.3 using the generalized master-equation approach. In this plot, one can clearly see that at low bias the Coulomb diamond edges are separated from one another which implies that transport via low-lying vibronic states is strongly suppressed. In this section, we are interested to explain the basic mechanism involved in this kind of transport suppression. Theory of Franck-Condon blockade shows that strong electron-vibron coupling can qualitatively affect the sequential tunneling dynamics [57, 58, 60, 61]. In the presence of strong electron-vibron interaction, the displacements of the potential

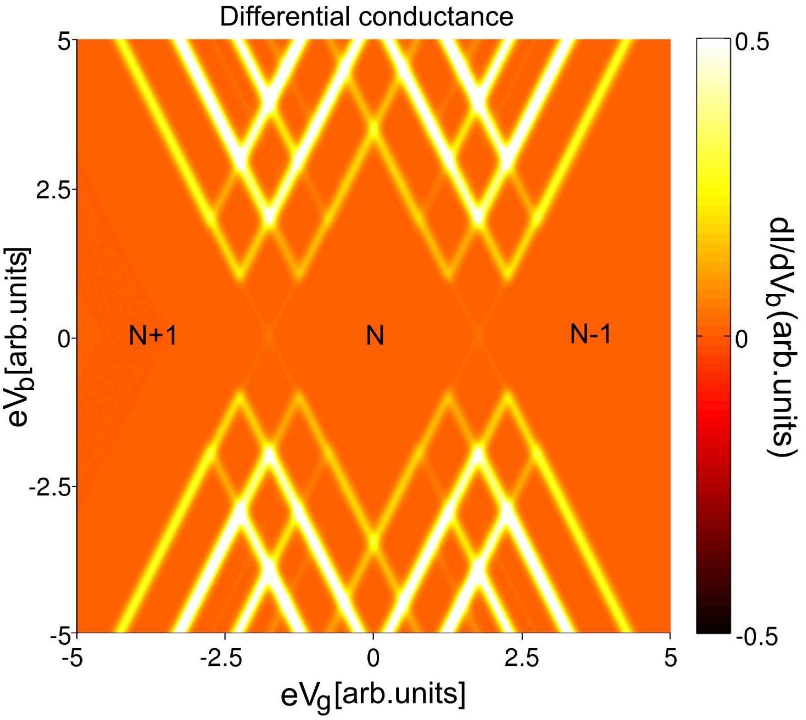

Figure 2.3: Stability diagram, differential conductance as a function of gate and bias voltage, which shows Coulomb diamonds for a generic quantum dot of a nanoelectromechanical system (NEMS). In the diamond shaped region around $V_\mathrm{b} = 0$ and $V_\mathrm{g} = 0$ the current is zero because of Coulomb blockade, while the suppression of the conductance at the charge degeneracy points represents the Franck-Condon (FC) blockade. The excitation lines running parallel to the Coulomb diamond edges denote the vibrational sidebands.

surfaces for the molecule in the N or $N+1$-particle states are large compared to the quantum fluctuations of the nuclear configuration in the vibrational ground state. Consequently, the overlap between low-lying vibronic states is exponentially small. This leads to a low-bias suppression of the sequential transport which is usually known as Franck-Condon blockade [57, 58]. In addition, a closer analysis of the transport characteristics shows that FC blockade cannot be lifted by means of a gate voltage, in contrast to other blockades like Coulomb blockade. Low bias suppression of the transport channels and hence FC blockade can be better understood by studying the Franck-Condon factor since the current suppression originates from the behavior of the FC matrix elements which determine the rates. This factor basically describes the wave-function overlap between different vibronic states participating in a particular transition. It provides very important information about the quantum mechanics of the quantum dot and strongly influences the transport properties of a single-molecule junction. In Fig. 2.4(a), the FC factor is depicted where one can identify the outer maxima, conventionally known as Condon parabola [17, 61, 62]. In the classically allowed region the FC factor is described by

$$m \geq \frac{(m' - m)^2}{4\lambda^2}, \tag{2.5}$$

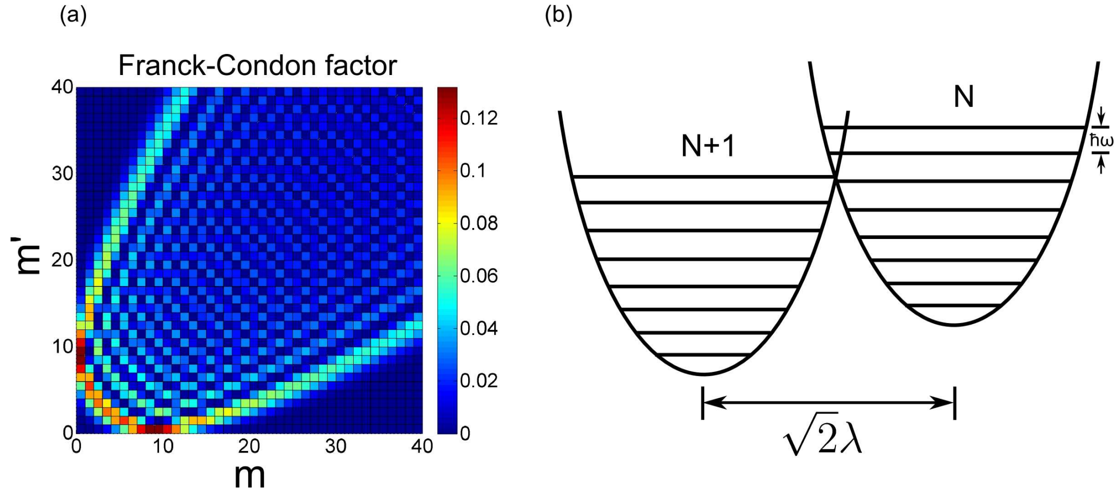

Figure 2.4: (a) Franck-Condon factor (FC) as a function of the vibrational numbers m and m'. (b) Schematic representation of the effective nuclear potentials for the N- and $N+1$-particle electronic states of the quantum dot system which define the overlap between low-lying vibronic states in the sequential tunneling process. The vibronic excitations exhibit harmonic spectrum with energy difference of $\hbar\omega$ between consecutive levels. The $N+1$-particle nuclear potential minimum is shifted by $\sqrt{2}\lambda$.

where m, m' are the vibrational numbers and λ is the electron-vibron dimensionless coupling constant. When the above relation is an equality, it represents a parabola in the (m, m') plane whose *axis of symmetry* makes an angle of $\pi/4$ with the m-axis. It contains very important information about the geometrical configuration of the system. It takes into account the fact that the stable nuclear configuration is shifted when the eigenstate of the dot is occupied, see Fig. 2.4(b). In principle, the Condon-parabola separates the classically forbidden and allowed regions. Fig. 2.4(a) reveals that the FC-factor is nonzero only in the classically allowed region where the classical orbits of the nuclear motion in the shifted potentials intersect in phase-space [17, 61, 62]. Within a quasi-classical envelope, the FC-factor oscillates with the vibronic numbers m and m' on the scale of the square of electron-vibron coupling constant [63]. The global maxima on the two axes can be determined as: $m \approx \lambda^2, m' = 0$ and $m' \approx \lambda^2, m = 0$. For very small electron-vibron coupling constants such that, $\lambda \to 0$, the Condon parabola narrows down to a single line, $F_{mm'} \to \delta_{mm'}$ where $F_{mm'}$ is the Franck-Condon factor. In the classically forbidden region, the FC-factor is extremely small. It implies that in the weak electron-vibron coupling regime, $\lambda \ll 1$, transitions mostly occur along the diagonal $m \to m'$. In the intermediate coupling limit, $\lambda \approx 1$, the distribution of transition rates becomes wider, and slightly non-diagonal transitions are enhanced. For strong electron-vibron coupling, $\lambda \gg 1$, the distribution widens enough and a gap of exponentially suppressed transitions between low-lying vibronic states opens [19, 57, 61]. Moreover, the vibronic excitation spectrum has harmonic nature which means that whenever the change in vibronic number $m' - m$ associated with N- and $N+1$-particle states enters the resonance condition, then transitions between all the states with the same difference $m' - m$ become allowed at a single resonance. It has remarkable consequences on the vibration-assisted transport because a single-electron transition can trigger a significant population of high vibrational excited states.

2.6 Generalized Master Equation

We pointed out at the beginning of this chapter that, similar as for the experimental techniques, many theoretical approaches are used for the investigation of transport properties of nanojunctions. One standard numerical approach is the combination of ab initio methods like density functional theory (DFT) with nonequilibrium Green's function techniques [33, 64] which can successfully explain the structure and transport characteristics of nanoscale devices, particularly, in the case of strong tunnel coupling. However, this approach cannot describe the transport properties of a system in the weak tunnel coupling regime where it cannot capture properly the effects induced by the Coulomb interactions. Other theoretical approaches that can solve the many body transport problems are numerical renormalization group (NRG) or the density matrix renormalization group (DMRG) schemes [65]. These techniques can successfully describe the dynamics of quantum systems within a wide parameter range. However, they are appropriate to solve only the problems related to simple models with a few number of degrees of freedom due to the complexity and large computational costs of these techniques. The Pauli-master equation description [66–68] is also a standard approach to the investigation of transport across a quantum dot system which is well separated from electronic reservoirs by large tunneling junctions. The occupation probabilities, current and other transport quantities can be calculated up to second order in the tunnel coupling [66] via rate equations using Fermi's Golden rule. However, in this approach the coherences, i.e., off-diagonal elements of a density matrix describing the dynamics of the many-body states of the dot are neglected. On the other hand, for more complex systems with degenerate states [69–75] and/or non-collinearly magnetic polarized leads [76–80], the non-diagonal elements of the density matrix play crucial role in the transport and can cause many quantum effects, e.g., interference [81], spin procession [82] and thus cannot be neglected. This approach to the description of the dynamics of the system fails because the Pauli rate equations are invariant under unitary transformations within the degenerate eigenstates of the quantum dot. Hence, the solution of a generalized master equation for the full density matrix coupling diagonal (populations) and off-diagonal (coherences) elements of the quantum-dot is required. Here we derive the equation of motion for the reduced density matrix (RDM) to lowest non-vanishing order in the tunneling Hamiltonian. In the weak tunnel coupling limit, the dynamics is extensively studied within the approach of Liouville equation method (see e.g., Refs. [69–71, 73, 75, 76, 81, 83–85]). The method is based on the well known Liouville equation for the time evolution of the density matrix of the full system consisting of the leads and generic quantum dot. In the following, we briefly introduce the basic concepts of a generalized master equation approach which takes into account electron transfer across the quantum dots up to second order in the tunnel coupling and includes all possible tunneling processes. We start in Sec. 2.7 with a model Hamiltonian of a generic quantum dot system which is coupled to a vibrational mode and weakly bridged between two metallic leads as depicted in Figure 2.1. Sec. 2.8 is dedicated to the solution of master equation in weak tunnel coupling regime. In Sec. 2.9, we point out the role played by the secular approximation in the presence of degenerate states of the system. In particular, it reduces the number of non-vanishing elements of the density matrix, as it sets to zero all coherences between non-degenerate states. Sec. 2.10 is devoted to the determination of current through the quantum dot system.

2.7 Model Hamiltonian

Consider a model system consisting of a generic quantum dot weakly coupled to leads and capacitively coupled to a gate electrode. In addition, the dot is also coupled to a vibrational mode as shown in Fig. 2.1. The overall system can be described by the Hamiltonian

$$\hat{H} = \hat{H}_{\text{sys}} + \hat{H}_{\text{s}} + \hat{H}_{\text{d}} + \hat{H}_{\text{T}} + \hat{H}_{\text{ext}}, \tag{2.6}$$

where $\hat{H}_{\text{sys}}$ represents an interacting system with known many-body eigenstates. It contains the dot Hamiltonian, vibron Hamiltonian, and the electron-vibron interaction Hamiltonian, i.e.,

$$\hat{H}_{\text{sys}} = \hat{H}_{\text{dot}} + \hat{H}_{\text{v}} + \hat{H}_{\text{e-v}}. \tag{2.7}$$

$\hat{H}_{\text{s/d}}$ in Eq. (2.6) describes the isolated metallic source and drain contacts as a Fermi gas of noninteracting quasi-particles given by

$$\hat{H}_{\alpha} = \sum_{\sigma\kappa} \varepsilon_{\alpha\sigma\kappa} \hat{c}^{\dagger}_{\alpha\sigma\kappa} \hat{c}_{\alpha\sigma\kappa}, \tag{2.8}$$

where $\hat{c}^{\dagger}_{\alpha\sigma\kappa}$ $(\hat{c}_{\alpha\sigma\kappa})$ creates (annihilates) a quasi-particle in a state κ with spin σ and energy $\varepsilon_{\alpha\sigma\kappa}$ in lead $\alpha = \text{s/d}$. The transfer of electrons between the leads and the central system is taken into account by the tunneling Hamiltonian

$$\hat{H}_{\text{T}} = \sum_{\alpha=\text{s,d}} \sum_{\sigma l \kappa} \left(t_{\alpha l} \hat{d}^{\dagger}_{l\sigma} \hat{c}_{\alpha\sigma\kappa} + t^{*}_{l\alpha} \hat{c}^{\dagger}_{\alpha\sigma\kappa} \hat{d}_{l\sigma} \right), \tag{2.9}$$

where $\hat{d}^{\dagger}_{l\sigma}$ creates an electron on the dot with spin σ and l degree of freedom. The coupling between quantum dot and leads is parametrized by the tunneling matrix elements $t_{\alpha l}$. For simplicity, we assume that the tunneling amplitude $t_{\text{s/d},l}$ of lead s/d is independent of the momentum $\hbar\kappa$ of the lead state. The first term in the above equation describes tunneling into, while the second term tunneling out of the dot. The condition for weak coupling requires that the tunneling induced level width $\hbar\Gamma$ should be small compared to the thermal energy $k_{\text{B}}T$. Finally, $\hat{H}_{\text{ext}}$ denotes the energy dependence of the system on the external voltage sources controlling the electrochemical potentials of the leads and the dot.

2.8 Dynamics of the reduced density matrix

In this section, we briefly demonstrate the derivation of the equation of motion for the reduced density matrix (RDM) to lowest nonvanishing order in the tunneling

Hamiltonian. In the derivations presented in this chapter, we mainly follow [86, 87]. Before the interaction $\hat{H}_\mathrm{T}$ is switched on at time $t = t_0$, with t_0 being some reference time, the system is unperturbed and the full density matrix $\hat{\rho}(t_0)$ is the direct product of the initial state $\hat{\rho}_\mathrm{sys}(t_0)$ of the quantum dot and the equilibrium state $\hat{\rho}_\mathrm{s/d}$ of the leads. Later on when the perturbation is switched on, at time $t > t_0$, correlations of the order of the tunnel coupling [86] between the leads and quantum dot is induced by the interaction, causing $\hat{\rho}(t_0)$ to deviate from the factorized form. Hence, we can calculate the time evolution of $\hat{\rho}(t)$ in the interaction picture as

$$\hat{\rho}(t) = \hat{U}_\mathrm{I}(t, t_0)\hat{\rho}(t_0)\hat{U}_\mathrm{I}^\dagger(t, t_0), \tag{2.10}$$

where the time evolution operator $\hat{U}_\mathrm{I}(t, t_0)$ is described by

$$\hat{U}_\mathrm{I}(t, t_0) = e^{\frac{i}{\hbar}\left(\hat{H}_\mathrm{sys}+\hat{H}_\mathrm{s}+\hat{H}_\mathrm{d}\right)(t-t_0)}e^{-\frac{i}{\hbar}\left(\hat{H}_\mathrm{sys}+\hat{H}_\mathrm{s}+\hat{H}_\mathrm{d}+\hat{H}_\mathrm{T}\right)(t-t_0)}. \tag{2.11}$$

Using Eqs. (2.10) and (2.11), we obtain the well known Liouville equation in the form

$$i\hbar\frac{\partial\hat{\rho}^I(t)}{\partial t} = \left[\hat{H}_\mathrm{T}^I(t), \hat{\rho}^I(t)\right], \tag{2.12}$$

which can also be expressed as

$$\hat{\rho}^I(t) = \hat{\rho}^I(t_0) - \frac{i}{\hbar}\int_{t_0}^{t}\mathrm{d}t'\left[\hat{H}_\mathrm{T}^I(t'), \hat{\rho}^I(t')\right]. \tag{2.13}$$

Substitution of Eq. (2.13) in Eq. (2.12) yields

$$\dot{\hat{\rho}}^I(t) = -\frac{i}{\hbar}\left[\hat{H}_\mathrm{T}^I(t), \hat{\rho}(t_0)\right] + \left(\frac{i}{\hbar}\right)^2\int_{t_0}^{t}\mathrm{d}t'\left[\hat{H}_\mathrm{T}^I(t), \left[\hat{H}_\mathrm{T}^I(t'), \hat{\rho}^I(t')\right]\right], \tag{2.14}$$

where $\hat{H}_\mathrm{T}^I(t)$ is the tunneling Hamiltonian in interaction picture and can be described as

$$\begin{aligned}\hat{H}_\mathrm{T}^I(t) &= e^{\frac{i}{\hbar}\left(\hat{H}_\mathrm{sys}+\hat{H}_\mathrm{s}+\hat{H}_\mathrm{d}\right)(t-t_0)}\hat{H}_\mathrm{T}e^{-\frac{i}{\hbar}\left(\hat{H}_\mathrm{sys}+\hat{H}_\mathrm{s}+\hat{H}_\mathrm{d}\right)(t-t_0)}\\ &= \sum_{\alpha l\kappa\sigma}\left[t_{\alpha l}\hat{c}^\dagger_{\alpha\sigma\kappa}\hat{d}_{l\sigma}(t)e^{\frac{i}{\hbar}\varepsilon_{\alpha\sigma\kappa}t} + \mathrm{h.c.}\right].\end{aligned} \tag{2.15}$$

Since we are interested in the transport through the central systems, it is convenient to consider the RDM $\hat{\rho}^I_\mathrm{red}(t)$ of the dot, which can be obtained from $\hat{\rho}^I(t)$ by tracing out the lead degrees of freedom, i.e.,

$$\hat{\rho}^I_\mathrm{red}(t) = \mathrm{Tr}_\mathrm{leads}\left\{\hat{\rho}^I(t)\right\}. \tag{2.16}$$

The first term in Eq. (2.14) vanishes by taking the trace over the lead degrees of freedom. In general, the leads are considered as large systems compared to the quantum dot. Moreover, we consider the weak tunnel coupling regime, where the influence of the central system on the leads is only marginal. Thus we treat the leads as reservoirs of noninteracting electrons in thermal equilibrium and hence we can factorize the density matrix $\hat{\rho}^I(t)$ as

$$\begin{aligned}\rho^I(t) &= \rho^I_{\text{sys}}(t) \otimes \rho_s \rho_d + \theta(t-t_0) O(\hat{H}_{\text{T}}) \\ &:= \rho^I_{\text{sys}}(t) \otimes \rho_{\text{leads}} + \theta(t-t_0) O(\hat{H}_{\text{T}}).\end{aligned} \tag{2.17}$$

Here $\rho_{\text{s/d}} = \frac{1}{Z_{\text{s/d}}} e^{-\beta(\hat{H}_{\text{s/d}} - \mu_{\text{s/d}} \hat{\mathcal{N}}_{\text{s/d}})}$ denotes the thermal equilibrium grandcanonical distribution of lead s/d, $Z_{\text{s/d}}$ is the partition function, β the inverse of the thermal energy, $\hat{\mathcal{N}}_{\text{s/d}}$ the electron number operator, and $\mu_{\text{s/d}}$ is the electrochemical potential of lead s/d which depends on the applied bias voltage $\mu_{\text{s/d}} = \mu_0 \pm \frac{V_b}{2}$ with μ_0 is the equilibrium electrochemical potential. Accounting for the time-evolution of the leads creation/annihilation operators, Eq. (2.14) can be described as:

$$\begin{aligned}\dot{\hat{\rho}}^I_{\text{red}}(t) = -\sum_{l\alpha\sigma\kappa} \frac{|t_{\alpha l}|^2}{\hbar^2} \int_{t_0}^{t} \mathrm{d}t' \Big\{ & f\left(\varepsilon_{\alpha\sigma\kappa} - \mu_\alpha\right) \hat{d}_{l\sigma}(t) \hat{d}^\dagger_{l\sigma}(t') \hat{\rho}^I_{\text{red}}(t') e^{\frac{i}{\hbar}\varepsilon_{\alpha\sigma\kappa}(t-t')} \\ & + \left[1 - f\left(\varepsilon_{\alpha\sigma\kappa} - \mu_\alpha\right)\right] \hat{d}^\dagger_{l\sigma}(t) \hat{d}_{l\sigma}(t') \hat{\rho}^I_{\text{red}}(t') e^{-\frac{i}{\hbar}\varepsilon_{\alpha\sigma\kappa}(t-t')} \\ & - \left[1 - f\left(\varepsilon_{\alpha\sigma\kappa} - \mu_\alpha\right)\right] \hat{d}_{l\sigma}(t) \hat{\rho}^I_{\text{red}}(t') \hat{d}^\dagger_{l\sigma}(t') e^{\frac{i}{\hbar}\varepsilon_{\alpha\sigma\kappa}(t-t')} \\ & - f\left(\varepsilon_{\alpha\sigma\kappa} - \mu_\alpha\right) \hat{d}^\dagger_{l\sigma}(t) \hat{\rho}^I_{\text{red}}(t') \hat{d}_{l\sigma}(t') e^{-\frac{i}{\hbar}\varepsilon_{\alpha\sigma\kappa}(t-t')} + \text{h.c} \Big\}.\end{aligned} \tag{2.18}$$

In the derivation of the above equation we have used the relation: $\text{Tr}_{\text{leads}} \left\{ \hat{c}^\dagger_{\alpha\sigma\kappa} \hat{c}_{\alpha'\sigma'\kappa'} \hat{\rho}_{\text{s}} \hat{\rho}_{\text{d}} \right\} = \delta_{\alpha\alpha'} \delta_{\kappa\kappa'} \delta_{\sigma\sigma'} f\left(\varepsilon_{\alpha\sigma\kappa} - \mu_\alpha\right)$, where $f\left(\varepsilon_{\alpha\sigma\kappa} - \mu_\alpha\right)$ is the Fermi function, and cyclic property of the trace. By summing over κ we obtain the generalized master equation (GME) for the reduced density matrix in the form

$$\begin{aligned}\dot{\hat{\rho}}^I_{\text{red}}(t) = -\sum_{l\alpha\sigma} \frac{|t_{\alpha l}|^2}{\hbar^2} \int_{t_0}^{t} dt' \big\{ & F_\sigma\left(t-t', \mu_\alpha\right) \hat{d}_{l\sigma}(t) \hat{d}^\dagger_{l\sigma}(t') \hat{\rho}^I_{\text{red}}(t') \\ & + F_\sigma\left(t-t', -\mu_\alpha\right) \hat{d}^\dagger_{l\sigma}(t) \hat{d}_{l\sigma}(t') \hat{\rho}^I_{\text{red}}(t') \\ & - F^*_\sigma\left(t-t', -\mu_\alpha\right) \hat{d}_{l\sigma}(t) \hat{\rho}^I_{\text{red}}(t') \hat{d}^\dagger_{l\sigma}(t') \\ & - F^*_\sigma\left(t-t', \mu_\alpha\right) \hat{d}^\dagger_{l\sigma}(t) \hat{\rho}^I_{\text{red}}(t') \hat{d}_{l\sigma}(t') + \text{H.c.} \big\},\end{aligned} \tag{2.19}$$

where the correlation function $F_\sigma\left(t-t', \mu_\alpha\right)$ associated with lead α is determined, in the wide band limit, as: From Eq. (2.18) we can write

$$\begin{aligned}F_\sigma\big(t-t', \mu_\alpha\big) &= \sum_\kappa f\big(\varepsilon_{\alpha\sigma\kappa} - \mu_\alpha\big) e^{\frac{i}{\hbar}\varepsilon_{\alpha\sigma\kappa}(t-t')} \\ &= \int_{-\infty}^{\infty} \mathrm{d}\varepsilon_{\alpha\sigma} D_{\alpha\sigma} f\big(\varepsilon_{\alpha\sigma} - \mu_\alpha\big) e^{\frac{i}{\hbar}\varepsilon_{\alpha\sigma}(t-t')} \\ &= e^{i\frac{\mu_\alpha}{\hbar}(t-t')} \int_{-\infty}^{\infty} \mathrm{d}\varepsilon_{\alpha\sigma} D_{\alpha\sigma} f\big(\varepsilon_{\alpha\sigma}\big) e^{\frac{i}{\hbar}\varepsilon_{\alpha\sigma}(t-t')},\end{aligned} \tag{2.20}$$

where $D_{\alpha\sigma}$ is the density of states of lead α with spin σ at the Fermi level. To simplify the above equation, we use the following relation: $f\left(\varepsilon\right)=\frac{1}{2}\left(1+\frac{e^{-\frac{\beta\varepsilon}{2}}-e^{\frac{\beta\varepsilon}{2}}}{e^{-\frac{\beta\varepsilon}{2}}+e^{\frac{\beta\varepsilon}{2}}}\right)$. Hence

$$\begin{aligned} F_{\sigma}\big(t-t',\mu_{\alpha}\big) = \frac{D_{\alpha\sigma}}{2}e^{i\frac{\mu_{\alpha}}{\hbar}(t-t')}\Bigg[&\int_{-\infty}^{\infty}\mathrm{d}\varepsilon_{\alpha\sigma}e^{\frac{i}{\hbar}\varepsilon_{\alpha\sigma}(t-t')} \\ &+\int_{-\infty}^{\infty}\mathrm{d}\varepsilon_{\alpha\sigma}\tanh\left(-\frac{\beta\varepsilon_{\alpha\sigma}}{2}\right)e^{\frac{i}{\hbar}\varepsilon_{\alpha\sigma}(t-t')}\Bigg]. \end{aligned} \tag{2.21}$$

The first term leads to the result

$$\int_{-\infty}^{\infty}\mathrm{d}\varepsilon_{\alpha\sigma}e^{\frac{i}{\hbar}\varepsilon_{\alpha\sigma}(t-t')}=2\pi\hbar\delta\big(t-t'\big). \tag{2.22}$$

The simplified form of the second part in Eq. (2.21) reads:

$$\begin{aligned} &\int_{-\infty}^{\infty}\mathrm{d}\varepsilon_{\alpha\sigma}\tanh\left(-\frac{\beta\varepsilon_{\alpha\sigma}}{2}\right)e^{\frac{i}{\hbar}\varepsilon_{\alpha\sigma}(t-t')} \\ &=\int_{-\infty}^{\infty}\mathrm{d}\varepsilon_{\alpha\sigma}\tanh\left(-\frac{\beta\varepsilon_{\alpha\sigma}}{2}\right) \\ &\times\left\{\cos\left[\frac{\varepsilon_{\alpha\sigma}}{\hbar}(t-t')\right]+i\sin\left[\frac{\varepsilon_{\alpha\sigma}}{\hbar}(t-t')\right]\right\}. \end{aligned} \tag{2.23}$$

Due to symmetry the cosine component of the integral vanishes. One can further use the following relation:

$$\int_{0}^{\infty}\mathrm{d}x\sin(ax)\tanh\left(\frac{bx}{2}\right)=\frac{\pi}{b\tanh\left(\frac{\pi a}{b}\right)},\quad\text{for } a,b\in\mathbb{R}. \tag{2.24}$$

Using Eq. (2.24), one can evaluate Eq. (2.23) to be

$$\int_{-\infty}^{\infty}\mathrm{d}\varepsilon_{\alpha\sigma}\tanh\left(-\frac{\beta\varepsilon_{\alpha\sigma}}{2}\right)\sin\left[\frac{\varepsilon_{\alpha\sigma}}{\hbar}(t-t')\right]=-\frac{2\pi}{\beta\sinh\left[\pi\frac{(t-t')}{\hbar\beta}\right]}. \tag{2.25}$$

Putting all together, the correlation function acquires the final form, in the wide band limit, as

$$F_{\sigma}\left(t-t',\mu_{\alpha}\right)=\pi\hbar D_{\alpha\sigma}e^{i\frac{\mu_{\alpha}}{\hbar}(t-t')}\left\{\delta\left(t-t'\right)-\frac{i}{\hbar\beta\sinh\left[\pi\frac{(t-t')}{\hbar\beta}\right]}\right\}. \tag{2.26}$$

This function characterizes the correlation which exists on average between events where a lead electron is destroyed at time t' and another is created at time t. It thus provides very important information about the time scales which control the relaxation dynamics of the leads. Moreover, Eq. (2.26) indicates that the correlation function

$F_\sigma\left(t-t',\mu_\alpha\right)$ decays with the time difference $t-t'$ approximately as $\exp\left[-\pi\frac{(t-t')}{\hbar\beta}\right]$ on the time scale $\frac{\hbar\beta}{\pi}$. Since we are interested in the long-term dynamical behavior of the system, we set $t_0 \to -\infty$ in Eq. (2.19). Further, we replace t' by $t-t''$. We then apply the Markov approximation, where the time evolution of $\hat{\rho}^I_{\mathrm{red}}$ is taken only local in time, meaning we approximate $\hat{\rho}_{\mathrm{red}}(t-t'') \sim \hat{\rho}_{\mathrm{red}}(t)$ in Eq. (2.19). In general, the condition of time locality requires that $\Gamma \ll \frac{\pi}{\hbar\beta}$. Here we defined from Eq. (2.19) together with Eq. (2.26), $\Gamma_\alpha = \sum_{l\sigma}\frac{2\pi}{\hbar}|t_{\alpha l}|^2 D_{\alpha\sigma}$ as the bare transfer rates and $\hbar\Gamma = \sum_\alpha \hbar\Gamma_\alpha$ as the tunneling-induced level width. However, the Markovian approximation becomes exact in the long time limit $t\to\infty$ [88]. Finally, taking into account all these simplifications, the generalized master equation for the reduced density matrix reads

$$\begin{aligned}\dot{\hat{\rho}}^I_{\mathrm{red}}(t) = &-\sum_{l\alpha\sigma}\frac{|t_{\alpha l}|^2}{\hbar^2}\int_0^\infty \mathrm{d}t''\big\{F_\sigma\left(t'',\mu_\alpha\right)\hat{d}_{l\sigma}(t)\hat{d}^\dagger_{l\sigma}(t-t'')\hat{\rho}^I_{\mathrm{red}}(t)\\ &+F_\sigma\left(t'',-\mu_\alpha\right)\hat{d}^\dagger_{l\sigma}(t)\hat{d}_{l\sigma}(t-t'')\hat{\rho}^I_{\mathrm{red}}(t)\\ &-F^*_\sigma\left(t'',-\mu_\alpha\right)\hat{d}_{l\sigma}(t)\hat{\rho}^I_{\mathrm{red}}(t)\hat{d}^\dagger_{l\sigma}(t-t'')\\ &-F^*_\sigma\left(t'',\mu_\alpha\right)\hat{d}^\dagger_{l\sigma}(t)\hat{\rho}^I_{\mathrm{red}}(t)\hat{d}_{l\sigma}(t-t'')+\mathrm{h.c.}\big\}.\end{aligned} \tag{2.27}$$

Since the eigenstates of the system are known, it is convenient to calculate the time evolution of $\hat{\rho}^I_{\mathrm{red}}$ in the eigenstates of the system Hamiltonian $\hat{H}_{\mathrm{sys}}$. Let $|n\rangle$ and $|m\rangle$ be the eigenstates of $\hat{H}_{\mathrm{sys}}$ in the N, $N+1$ particle Hilbert spaces $\mathcal{H}_N$ and $\mathcal{H}_{N+1}$, respectively. Then it holds

$$\langle n|\hat{d}_{l\sigma}(t)|m\rangle := \left(\hat{d}_{l\sigma}(t)\right)_{nm} = \left(\hat{d}_{l\sigma}\right)_{nm} e^{\frac{i}{\hbar}(E_n-E_m)(t-t_0)},$$

where we have used the relation

$$\hat{H}_{\mathrm{sys}}|n\rangle = E_n|n\rangle$$

and

$$\hat{d}_{l\sigma}(t) = e^{\frac{i}{\hbar}\hat{H}_{\mathrm{sys}}(t-t_0)}\hat{d}_{l\sigma}e^{-\frac{i}{\hbar}\hat{H}_{\mathrm{sys}}(t-t_0)}.$$

2.9 Role of coherences and secular approximation

For a system with spectrum containing degenerate states, coherences exist between the degenerate states which make the problem quite complex. Specifically, the situation addressed in the next chapter, a large number of vibronic degenerate states contribute to transport at finite bias. Generally, a system residing in an n-dimensional Hilbert space is described by an $n\times n$ density matrix, the associated Liouvillian has dimension n^4. Hence, the inclusion of the full set of all possible second order contributions in Eq. (2.27) for any gate and bias voltage leads to a hard numerical task to solve the equation of motion even for systems with moderate number of quantum states. However, for most practical problems there exist some selection rules which allow us to set to zero certain elements of the density matrix from the beginning. The reason is that whenever two quantum states $|m\rangle$ and $|l\rangle$ of the system differ by some quantum number which is conserved in the total system (including the reservoirs), a coherence can be ignored. Thus in view of the above argumentation, Eq. (2.27) can be solved taking into account the following approximations:

(i) We assume that the system is in a pure charge state and hence the density matrix elements between states representing different charge state vanish, since the total charge is conserved. It implies that defining the reduced density matrix operator $\hat{\rho}$ on the Fock space of the quantum dot, one can neglect coherences (off-diagonal elements of the density matrix) between states with different particle number, since they are decoupled from the dynamics of the populations. As a result, $\hat{\rho}^{I}_{\text{red}}$ can be decomposed into block matrices $\hat{\rho}^{IN}_{\text{red}}$ describing the dot in N-particle state. Consequently, Eq. (2.27) can be expressed in the eigenbasis of $\hat{H}_{\text{sys}}$ as

$$\begin{aligned}
\dot{\rho}^{IN}_{nm}(t) = -\sum_{\alpha}\Bigg\{ &\sum_{j\in\{|N\rangle\}}\Bigg[\sum_{k\in\{|N+1\rangle\}}\Gamma^{(+)NN+1}_{\alpha,nkkj} + \sum_{i\in\{|N-1\rangle\}}\Gamma^{(+)NN-1}_{\alpha,niij}\Bigg]\rho^{IN}_{jm}(t)e^{\frac{i}{\hbar}E_{nj}(t-t_0)} \\
&+ \sum_{j'\in\{|N\rangle\}}\Bigg[\sum_{k\in\{|N+1\rangle\}}\Gamma^{(-)NN+1}_{\alpha,j'kkm} + \sum_{i\in\{|N-1\rangle\}}\Gamma^{(-)NN-1}_{\alpha,j'iim}\Bigg]\rho^{IN}_{nj}(t)e^{\frac{i}{\hbar}E_{j'm}(t-t_0)} \\
&- \sum_{k,k'\in\{|N+1\rangle\}}\Bigg[\Gamma^{(-)N+1N}_{\alpha,k'mnk} + \Gamma^{(+)N+1N}_{\alpha,k'mnk}\Bigg]\rho^{IN+1}_{kk'}(t)e^{\frac{i}{\hbar}(E_{nk}+E_{k'm})(t-t_0)} \\
&- \sum_{i,i'\in\{|N-1\rangle\}}\Bigg[\Gamma^{(-)N-1N}_{\alpha,i'mni} + \Gamma^{(+)N-1N}_{\alpha,i'mni}\Bigg]\rho^{IN-1}_{ii'}(t)e^{\frac{i}{\hbar}(E_{ni}+E_{i'm})(t-t_0)}\Bigg\},
\end{aligned} \tag{2.28}$$

where the quantities $\Gamma^{(p)NN\pm1}_{\alpha,k'mnk}$ represent the transition amplitudes between states with N and $N \pm 1$ particle states. For transition $N \rightarrow N+1$

$$\Gamma^{(p)NN+1}_{\alpha,k'mnk} := \sum_{\sigma l}\frac{|t_{\alpha l}|^2}{\hbar^2}\int_0^\infty \mathrm{d}t'' F_\sigma\left(pt'',\mu_\alpha\right)\left(\hat{d}_{l\sigma}\right)^{NN+1}_{k'm}\left(\hat{d}^\dagger_{l\sigma}(-pt'')\right)^{N+1N}_{nk}, \tag{2.29}$$

and for the transition $N \rightarrow N-1$

$$\Gamma^{(p)NN-1}_{\alpha,k'mnk} := \sum_{\sigma l}\frac{|t_{\alpha l}|^2}{\hbar^2}\int_0^\infty \mathrm{d}t'' F_\sigma\left(pt'',\mu_\alpha\right)\left(\hat{d}^\dagger_{l\sigma}\right)^{NN-1}_{k'm}\left(\hat{d}_{l\sigma}(-pt'')\right)^{N-1N}_{nk}. \tag{2.30}$$

In the above equations, we have used the notation

$$\left(\hat{d}_{l\sigma}\right)^{NN+1}_{km} := \langle k|\hat{d}_{l\sigma}|m\rangle, \tag{2.31}$$

where $|k\rangle$ and $|m\rangle$ are the eigenstates of $\hat{H}_{\text{sys}}$ with particle number N, $N+1$, respectively. The energy differences E_{nj} used in Eq. (2.28) are given by

$$E_{nj} = E_n - E_j.$$

(ii) Coherences between states with the same number of particles but with different energies can be neglected, when their energy difference is larger than the level width

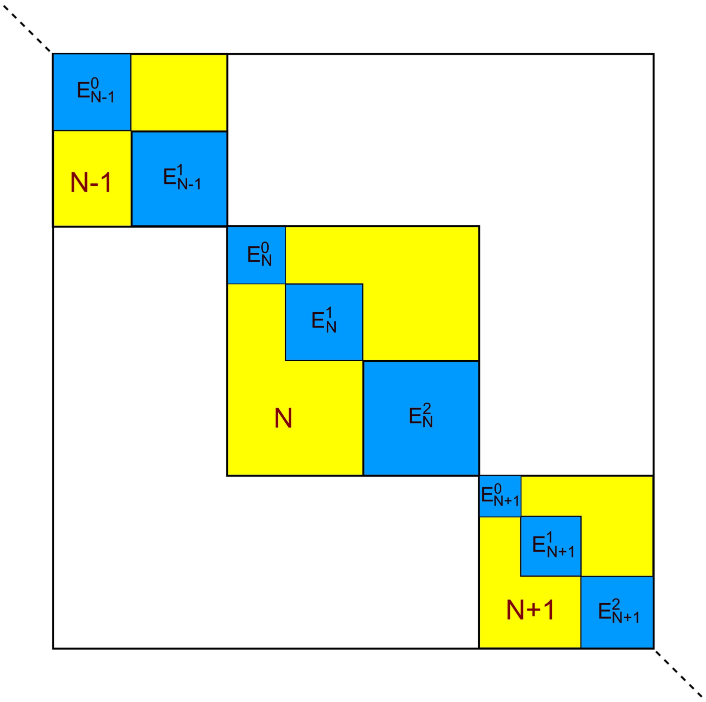

Figure 2.5: Schematic representation of the reduced density matrix in blocks form belonging to fixed charge N. Only coherences between states with the same number of particle and energy are retained.

$\hbar\Gamma$ [86]. In this case, they are irrelevant due to their rapid fluctuation compared to the dynamics of the system induced by the tunnel coupling. Coherences between quasidegenerate states can be retained if their energy difference is smaller than the tunneling induced level width. It means that the secular approximation allows us to retain only those terms in the equation of motion which have no oscillatory behavior with time t. From the system dynamics point of view, it implies that one can not resolve the evolution of $\hat{\rho}^I_{\mathrm{red}}(t)$ on time scales of $\hbar/(E_m - E_n)$, where E_m and E_n represent two distinct energy levels of the system Hamiltonian $\hat{H}_{\mathrm{sys}}$. From the first and second line of Eq. (2.28) the secular approximation leads to the conditions

$$E_n = E_j, \tag{2.32}$$

$$E_m = E_{j'}, \tag{2.33}$$

while the third and fourth line gives

$$E_n - E_k + E_{k'} - E_m = 0, \quad E_n - E_i + E_{i'} - E_m = 0. \tag{2.34}$$

If we select $E_n = E_m$, $E_n \neq E_m$ in Eq. (2.32) and Eq. (2.33), then indeed $E_m = E_j$, $E_m \neq E_j$ and $E_n = E_{j'}$, $E_n \neq E_{j'}$ must be fulfilled. Moreover, if $E_n = E_m$, $E_n \neq E_m$ in Eq. (2.34), then $E_{k,i} = E_{k',i'}$, $E_{k,i} \neq E_{k',i'}$ must hold. It follows that as a consequence of the secular approximation, in the equations of motion Eq. (2.28) the elements of the RDM between degenerate and non-degenerate states get decoupled [86, 87]. Since the current is determined by the dynamics of the populations of the many body states, it is convenient to focus on the time evolution of the degenerate matrix elements. Thus we can further divide $\hat{\rho}^I_{\text{red}}(t)$ into block matrices $\hat{\rho}^{IE_N}_{\text{red}}(t)$ restricted to the Hilbert space $\mathcal{H}_{E_N}$ spanned by the states with a particular energy level E_N and charge state N. A schematic representation of the resulting pattern of the RDM is given in Fig. 2.5. To be more compact, we can represent the equations of motion for $\hat{\rho}^{IE_N}_{\text{red}}(t)$ in Bloch-Redfield form [71, 86, 87]

$$\dot{\rho}^{I,E_N}_{nm}(t) = -\sum_{kk'} R^{E_N}_{nmkk'} \rho^{I,E_N}_{kk'}(t) + \sum_{M=N\pm 1} \sum_{E'} \sum_{kk'} R^{E_N E'_M}_{nmkk'} \rho^{I,E'_M}_{kk'}(t), \tag{2.35}$$

where the indices n, m, k, k' refer to the eigenstates of $\hat{H}_{\text{sys}}$ and k, k' runs over all degenerate states with fixed particle number. The Redfield tensors are given by

$$R^{E_N}_{nmkk'} = \sum_{\alpha=\text{s,d}} \sum_{M,E',j} \left(\delta_{mk'} \Gamma^{(+)E_N E'_M}_{\alpha,njjk} + \delta_{nk} \Gamma^{(-)E_N E'_M}_{\alpha,k'jjm} \right), \tag{2.36}$$

and

$$R^{E_N E'_M}_{nmkk'} = \sum_{\alpha,p=\pm} \Gamma^{(p)E'_M E_N}_{\alpha,k'mnk}, \tag{2.37}$$

where the quantities $\Gamma^{(p)E_N E'_M}_{\alpha,k'mnk}$ are transition rates from a state with N particles and energy E_N to a state with M particles and energy E'_M. Let us start with tunneling in, i.e., $N \to N+1$ process. Its transition rate is given by

$$\Gamma^{(p)E_N E'_{N+1}}_{\alpha,k'mnk} = \sum_{\sigma l} \frac{|t_{\alpha l}|^2}{\hbar^2} \left(\hat{d}_{l\sigma}\right)^{E_N E'_{N+1}}_{k'm} \left(\hat{d}^{\dagger}_{l\sigma}\right)^{E'_{N+1} E_N}_{nk} \int_0^\infty \mathrm{d}t'' F_\sigma\left(pt'', \mu_\alpha\right) e^{-p\frac{i}{\hbar}(E'_{N+1}-E_N)t''}, \tag{2.38}$$

whereas for the transition $N \to N-1$

$$\Gamma^{(p)E_N E_{N-1}}_{\alpha,k'mnk} = \sum_{\sigma l} \frac{|t_{\alpha l}|^2}{\hbar^2} \left(\hat{d}^{\dagger}_{l\sigma}\right)^{E_N E'_{N-1}}_{k'm} \left(\hat{d}_{l\sigma}\right)^{E'_{N-1} E_N}_{nk} \int_0^\infty \mathrm{d}t'' F_\sigma\left(pt'', \mu_\alpha\right) e^{-p\frac{i}{\hbar}(E'_{N-1}-E_N)t''}, \tag{2.39}$$

where we have used

$$\left(\hat{d}_{l\sigma}\right)^{E_N E'_{N+1}}_{km} := \langle k|\hat{d}_{l\sigma}|m\rangle, \tag{2.40}$$

which represents the matrix element of the dot electron operator $\hat{d}_{l\sigma}$ between the eigenstates of the system $|k\rangle$ and $|m\rangle$ with particle number N, $N+1$ and energy E_N, E'_{N+1}, respectively. Eq. (2.35) explicitly captures all the dynamical properties of the charge transport through the dot. In order to investigate the transport characteristics, it is convenient to determine a relation for a current.

2.10 Current

Current can be described as the net tunneling rate through a quantum dot in a specific direction at the source or drain contact. To determine the current through lead α, we calculate the current operator as [52]

$$\hat{I}_\alpha = \frac{\mathrm{d}\hat{\mathcal{N}}_\alpha}{\mathrm{d}t} = -\frac{\mathrm{i}}{\hbar}\left[\hat{H}_{\mathrm{T}\alpha}, \hat{\mathcal{N}}_\alpha\right], \tag{2.41}$$

where $\hat{H}_{\mathrm{T}\alpha}$ is the tunneling Hamiltonian of a particle between the quantum dot and lead α, whereas $\hat{\mathcal{N}}_\alpha = \sum_{\sigma\kappa} \hat{c}^\dagger_{\alpha\sigma\kappa}\hat{c}_{\alpha\sigma\kappa}$ is the particle number operator of lead α. Thus the current can be evaluated as

$$I_\alpha = \mathrm{Tr}_{\mathrm{sys}}\left\{\hat{I}_\alpha \hat{\rho}^I_{\mathrm{red}}(t)\right\}. \tag{2.42}$$

Substituting the values, Eq. (2.42) yields

$$I_\alpha = 2\alpha \mathrm{Re} \sum_{N,E,E'} \sum_{nkj} \left(\Gamma^{(+)E_N E'_{N+1}}_{\alpha,njjk} - \Gamma^{(+)E_N E'_{N-1}}_{\alpha,njjk}\right) \rho^{I,E_N}_{kn}. \tag{2.43}$$

where we have introduced the convention $\alpha = \mathrm{s}/\mathrm{d} = \pm 1$. In the above equation, the first term on the right side denotes the tunneling into the dot, while the second term represents tunneling out of the dot. In the steady state the current through the source must be equal to the current at the drain in order to avoid the net accumulation of charge on the quantum dot. In transport calculations we are often interested in long-term dynamical behavior of the system. Hence, we can determine the stationary current by replacing ρ^{I,E_N} with $\rho^{I,E_N}_{\mathrm{st}}$ in Eq. (2.43). Note that the above expression of the current explicitly takes into account the coherences of the RDM. In particular, coherences between states with the same number of particles but different energies can become important when the difference in their energies is of the same order of magnitude as the tunneling induced level width, while the coherences between states with different number of particles are decoupled from the dynamics of populations and eventually vanish exactly in the stationary limit. From a mathematical point of view, it is crucial to take into account the coherences in order to ensure the invariance of the transport calculations under any unitary transformation U_{E_N} within the Hilbert spaces $\mathcal{H}_{E_N}$ consisting of all the eigenstates of the system with a particular energy and particle number. Since the RDM is hermitian, there always exists an appropriate eigenbasis of the system Hamiltonian $\hat{H}_{\mathrm{sys}}$ in which all coherences are vanishing. However, for a complex system it is not trivial to find a priori the basis that diagonalizes the Hamiltonian of the system. In addition, this *diagonalizing basis* strongly depends on the energies provided to the system, particularly on the external voltage.

Chapter 3

Vibration-assisted transport through nanostructures

Vibrational modes strongly affect the transport characteristics of a quantum dot system. Pronounced vibrational signatures in electronic transport have been observed in many recent experiments on molecules [2–6] and single wall carbon nanotube quantum dots [43–45, 89]. In order to explain some of these features, specifically, negative differential conductances (NDCs) in the measured stability diagrams, we propose here in this chapter a theoretical model where a single molecule is coupled to several vibronic modes. The molecular quantum dot (QD) is further weakly coupled to source (S) and drain (D) contacts and capacitively coupled to a gate electrode, see Fig. 3.1. We address two different cases: (i) Symmetric setup (ii) Asymmetric setup. In the first case, the dot is symmetrically coupled to the leads, whereas in the second case one orbital degree of freedom is stronger coupled to the leads compared to the other. To proceed, we model the system Hamiltonian as below.

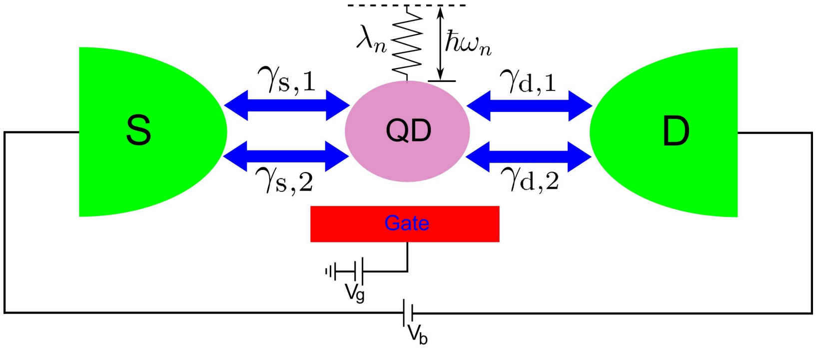

Figure 3.1: Transport setup with a generic multilevel quantum dot (QD) symmetrically coupled to source (S) and drain (D) contacts and capacitively coupled to a gate electrode. In addition, the dot is coupled to the nth vibrational mode with energy $\hbar\omega_n$ via a dimensionless coupling constant λ_n. $\gamma_{s/d,1}$ and $\gamma_{s/d,2}$ denote coupling constants of the orbital states 1 and 2 to the source and drain contacts, respectively.

3.1 Model Hamiltonian for the central system

In most cases the simple Anderson-Holstein model, where a quantum dot is coupled to a vibrational mode, has been studied [58, 60–62]. In this chapter, we consider a different situation in which we characterize the system by a generalized Anderson-Holstein model where two degenerate or quasidegenerate molecular levels are coupled to many vibrational modes. This model appropriately describes transport through vibrating quantum dots with a discrete electronic spectrum. Consequently, several energetic degenerate vibronic configurations arise which may contribute to transport at finite bias. Thus the Hamiltonian of the central system is modeled in the form

$$\hat{H}_{\mathrm{sys}} = \hat{H}_{\mathrm{mol}} + \hat{H}_{\mathrm{v}} + \hat{H}_{\mathrm{e\text{-}v}}, \tag{3.1}$$

where $\hat{H}_{\mathrm{mol}}$ describes two quasidegenerate levels whose Hamiltonian can be represented as

$$\hat{H}_{\mathrm{mol}} = \sum_{l\sigma} \varepsilon_l \hat{N}_{l\sigma} + \frac{U}{2}\hat{N}\left(\hat{N}-1\right), \tag{3.2}$$

where $l = 1, 2$ is the orbital and $\sigma =\uparrow, \downarrow$ is the spin degree of freedom. The operator $\hat{N}_{l\sigma} = \hat{d}^{\dagger}_{l\sigma}\hat{d}_{l\sigma}$ counts the number of electrons with spin σ in the orbital l. $\hat{N} = \sum_{l\sigma}\hat{N}_{l\sigma}$ is the total number operator. The orbital energy is $\varepsilon_l = \varepsilon_0\left[1 + (-1)^l\,\Delta\right]$, with Δ an orbital mismatch. The Coulomb blockade is taken into account via the charging energy U and we assume $U > \varepsilon_0$.
The vibron Hamiltonian is expressed as

$$\hat{H}_{\mathrm{v}} = \sum_{n\geq 1} \varepsilon_n \left(\hat{a}^{\dagger}_n \hat{a}_n + \frac{1}{2}\right), \tag{3.3}$$

where $\hat{a}_n(\hat{a}^{\dagger}_n)$ annihilates (creates) a vibron in the nth mode with energy $\varepsilon_n = \hbar\omega_n$. We assume that the energy of the nth mode is given by

$$\varepsilon_n = n\hbar\omega, \tag{3.4}$$

being an nth multiple of the energy $\varepsilon_1 = \hbar\omega$ of the fundamental mode as it is, for example, for longitudinal stretching modes in quantum wires and carbon nanotubes. Finally, the electron-vibron interaction Hamiltonian is describes as

$$\hat{H}_{\mathrm{e\text{-}v}} = \sum_{n\geq 1}\sum_{l\sigma} g_n \hat{N}_{l\sigma}\left(\hat{a}^{\dagger}_n + \hat{a}_n\right), \tag{3.5}$$

where g_n is the coupling constant for the nth vibronic mode.

3.1.1 Elimination of electron-vibron interaction

In order to solve the Hamiltonian of the system and obtain its spectrum, we decouple the electron-vibron interaction Hamiltonian by applying a unitary polaron transformation [56]. Explicitly, we set $\tilde{\hat{H}}_{\mathrm{sys}} \equiv e^{\hat{S}}\hat{H}_{\mathrm{sys}}e^{-\hat{S}}$, where

$$\hat{S} = \sum_{n\geq 1}\sum_{l\sigma} \lambda_n \hat{N}_{l\sigma}\left(\hat{a}^{\dagger}_n - \hat{a}_n\right) \tag{3.6}$$

and $\lambda_n = g_n/\hbar\omega_n$ is the dimensionless coupling constant associated with mode n. Note that $\lambda = \frac{g_1}{\hbar\omega_1}$ is the coupling constant of the fundamental mode. We assume $\lambda = 0.68,\ 0.83$ and 1.18 in the analysis of the spectrum, which is in the range of values observed e.g., in experiments on carbon nanotubes [43, 45, 89]. Under the polaron transformation the operator $\hat{d}_{\sigma l}$ is transformed as

$$\tilde{\hat{d}}_{l\sigma} = e^{\hat{S}}\hat{d}_{l\sigma}e^{-\hat{S}} = \hat{d}_{l\sigma}\hat{X}, \tag{3.7}$$

where $\hat{X} = \exp\left[-\sum_{n\geq 1}\lambda_n\left(\hat{a}_n^\dagger - \hat{a}_n\right)\right]$. In a similar way, the shifted vibronic operator is

$$\tilde{\hat{a}}_n = \hat{a}_n - \lambda_n\sum_{l\sigma}\hat{N}_{l\sigma}. \tag{3.8}$$

The transformed form of the system Hamiltonian is thus

$$\tilde{\hat{H}}_{\text{sys}} = \sum_{l\sigma}\tilde{\varepsilon}_l\hat{N}_{l\sigma} + \sum_{n\geq 1}\varepsilon_n\left(\hat{a}_n^\dagger\hat{a}_n + \frac{1}{2}\right) + \frac{\tilde{U}}{2}\hat{N}\left(\hat{N}-1\right), \tag{3.9}$$

where $\tilde{\varepsilon}_l = \varepsilon_l - \sum_n \frac{|g_n|^2}{\hbar\omega_n}$ is the renormalized orbital energy and $\tilde{U} = U - 2\sum_n\frac{|g_n|^2}{\hbar\omega_n}$ is the Coulomb repulsion modified by the vibron mediated interaction.
The eigenstates of the system are

$$|\vec{N},\vec{m}_v\rangle_1 := e^{-\hat{S}}|\vec{N},\vec{m}_v\rangle. \tag{3.10}$$

where $\vec{N} = (N_{1\uparrow}, N_{1\downarrow}, N_{2\uparrow}, N_{2\downarrow})$ and $N_{l\sigma}$ the number of electrons in the branch $(l\sigma)$. Note that $N = \sum_{l\sigma}N_{l\sigma}$ defines the total number of electrons on the dot. For later purposes we indicate the ground state and first excited state with 0 electrons as, see Fig. 3.3(b)

$$\begin{aligned} |0,0\rangle &:= |\vec{0},\vec{0}\rangle_1, \\ |0,1\rangle &:= |\vec{0},\vec{m}_v = (1,0,0,...)\rangle_1, \end{aligned} \tag{3.11}$$

The first excited state with 0 electron contains one vibronic excitation in the first mode, i.e., $\vec{m}_v = (1,0,0,...)$. In a similar way, we define the ground states and first excited states with $N = 1$ electron. For zero orbital mismatch one has fourfold degeneracy, see again Fig. 3.3(b), i.e.,

$$\begin{aligned} |1_k,0\rangle &:= |\vec{1}_k,\vec{0}\rangle_1, \quad k = 1,2,3,4, \\ |1_k,1\rangle &:= |\vec{1}_k,\vec{m}_v = (1,0,0,...)\rangle_1, \end{aligned} \tag{3.12}$$

where $\vec{1}_k \in \left\{(1,0,0,0),(0,1,0,0),(0,0,1,0),(0,0,0,1)\right\}$. We note that both for $N = 0$ and $N = 1$ the second excited states are vibronically degenerate for the dispersion relation Eq. (3.4), then the configurations $\vec{m}_v = (2,0,0,...)$ and $\vec{m}_v = (0,1,0,...)$ have the same energy. For finite orbital mismatch $\Delta \neq 0$, the orbital degeneracy is broken. The case $0 < \varepsilon_0 \Delta < \hbar\omega$ is illustrated in Fig. 3.9(b). The corresponding states are:

$$\begin{aligned}
|1_{kg}, 0\rangle &:= |\vec{1}_{kg}, \vec{0}\rangle_1, \quad k = 1, 2,\\
|1_{ke}, 0\rangle &:= |\vec{1}_{ke}, \vec{0}\rangle_1, \quad k = 1, 2,\\
|1_{kg}, 1\rangle &:= |\vec{1}_{kg}, \vec{m}_v = (1, 0, 0, ...)\rangle_1,\\
|1_{ke}, 1\rangle &:= |\vec{1}_{ke}, \vec{m}_v = (1, 0, 0, ...)\rangle_1,
\end{aligned} \tag{3.13}$$

and $\vec{1}_{kg} \in \{(1, 0, 0, 0), (0, 1, 0, 0)\}$, $\vec{1}_{ke} \in \{(0, 0, 1, 0), (0, 0, 0, 1)\}$.

3.2 Generalized master equation for unpolarized quantum dots

In the case of high degeneracy of the spectrum, the appropriate technique to treat the dynamics of the system in the weak coupling regime is the Liouville equation method for the time evolution of the density matrix of the total system consisting of the leads and the dot. The detailed analysis and derivation can be found in Chapter 2 where the generalized master equation given by Eq. (2.35) was derived for a generic quantum dot. In order to determine the specific form of the Bloch Redfield tensors $R^{E_N}_{nmkk'}$ and $R^{E_N E'_M}_{nmkk'}$ we need to find the values for the transition amplitudes $\Gamma^{(p)E_N E'_M}_{\alpha,k'mnk}$ given by Eqs. (2.38) and (2.39). Note that for the special case to be considered in this chapter, we have to take into account that if $N = 0$ then $M = 1$, while if $N = 4$ then $M = 3$. To solve the system we need to calculate the matrix elements of the dot electron operators in the eigenbasis of $\hat{H}_{\text{sys}}$. In the following we determine the matrix elements of the electron operators.

3.3 Transition matrix elements of electron operators and the transition rates

In order to determine the transition rates, first we need to calculate the transition matrix elements. Thus in the eigenbasis of the system, the transition matrix elements yield

$$\langle r|\hat{d}_{l\sigma}|s\rangle = e^{-\frac{1}{2}\sum_n |\lambda_n|^2} \prod_n F\left(\lambda_n, m_n, m'_n\right), \tag{3.14}$$

where $|r\rangle$ and $|s\rangle$ represent the eigenstates given by Eq. (3.10). The function $F(\lambda, m, m')$ determines the coupling between states with a different vibronic number of excitations with effective coupling λ and is expressed as [71, 90]

$$\begin{aligned}
F(\lambda, m, m') = &\left[\Theta(m' - m)\lambda^{m'-m} + \Theta(m - m')\left(-\lambda^*\right)^{m-m'}\right]\\
&\times \sqrt{\frac{m_{\min}!}{m_{\max}!}} \sum_{i=0}^{m_{\min}} \frac{\left(-|\lambda|^2\right)^i}{i!(i + m_{\max} - m_{\min})!} \frac{m_{\max}!}{(m_{\min} - i)!},
\end{aligned} \tag{3.15}$$

where $m_{\min/\max} = \min/\max(m, m')$. Now using the above equation, one can readily calculate the transition rates in the form

$$\Gamma^{(p)E_N E'_{N+1}}_{\alpha,k'mnk} = \sum_{l\sigma} \Gamma^{(p)}_{\alpha,l+}(\varepsilon_\alpha) \left(\hat{d}_{l\sigma}\right)^{E_N E'_{N+1}}_{k'm} \left(\hat{d}^\dagger_{l\sigma}\right)^{E'_{N+1}E_N}_{nk}, \tag{3.16}$$

with $\varepsilon_\alpha = -eV_\alpha - \left(E_N - E'_{N+1}\right)$ and V_α the electrochemical potential of lead α. Likewise

$$\Gamma^{(p)E_N E'_{N-1}}_{\alpha,k'mnk} = \sum_{l\sigma} \Gamma^{(p)}_{\alpha,l-}(\varepsilon'_\alpha) \left(\hat{d}^\dagger_{l\sigma}\right)^{E_N E'_{N-1}}_{k'm} \left(\hat{d}_{l\sigma}\right)^{E'_{N-1}E_N}_{nk}, \tag{3.17}$$

with $\varepsilon'_\alpha = -eV_\alpha - \left(E'_{N-1} - E_N\right)$. Moreover, we introduced

$$\Gamma^{(p)}_{\alpha,l\pm}(E) = \gamma_{\alpha l} f^\pm(E) + \frac{ip}{\pi}\gamma_{\alpha l} P \int d\varepsilon \frac{f^\pm(\varepsilon)}{\varepsilon - E}, \tag{3.18}$$

where $f^+(\varepsilon) = f(\varepsilon)$ is the Fermi function while $f^-(\varepsilon) = 1 - f(\varepsilon)$ and $\gamma_{\alpha l} = \frac{2\pi}{\hbar} D_\alpha |t_{\alpha l}|^2$ are the bare transfer rates with constant density of states of lead D_α. Note that the transition rates calculated above explicitly contain product of Franck-Condon factors with coupling constants depending on the mode number. Finally, knowing the stationary density matrix ρ^I_{st}, the (particle) current through lead α is determined by, cf. Eq. (2.43)

$$I_\alpha = 2\alpha \mathrm{Re} \sum_{N,E,E'} \sum_{nkj} \left(\Gamma^{(+)E_N E'_{N+1}}_{\alpha,njjk} - \Gamma^{(+)E_N E'_{N-1}}_{\alpha,njjk}\right) \rho^{I,E_N}_{kn,st}. \tag{3.19}$$

If the relation given by Eq. (3.4) holds, then spin and orbital degeneracies intrinsic in the electronic structure are supplemented by degeneracies related to the vibronic structure. Several vibronic modes with frequencies $\omega_n = n\omega$ multiples of the fundamental frequency ω give rise, in fact, naturally to several degenerate vibronic configurations. This is the situation we shall focus on in the rest of this chapter.

A degenerate spectrum is a necessary condition for the appearance of interference effects in the transport characteristics both in the linear and non linear regime [69, 70, 72, 73, 75, 76, 79, 80, 85, 90, 91] and these effects can be captured only by considering not only populations (diagonal elements) but also coherences (off-diagonal elements) of the reduced density matrix.

For the system considered in this chapter, we calculated the current both with and without coherences between degenerate states up to five vibronic modes, obtaining though only quantitative but not qualitative differences. While spin and orbital degeneracies can be a priori excluded from the transport through a single molecule with nonpolarized leads [90], the role played by the vibronic coherences requires a more careful analysis.

We have confirmed that it is not possible to construct a linear combination of degenerate states $\{|s\rangle\}$ with finite transition amplitude to a state $|r\rangle$ at one lead but decoupled from $|r\rangle$ at the other lead, where $|r\rangle$ and $|s\rangle$ represent the states given by Eq. (3.10).

This observation, complemented by the general method presented in Ref. [92], proves the absence of interference blocking states in our system. Thus, interference, even if present, does not have dramatic consequences on the transport characteristics of the system.

All the current maps presented in the next section are hence, apart from Fig. 3.7(b), calculated neglecting coherences. As shown explicitly in Fig. 3.7(b), this approximation does not affect qualitatively the results (at least in the low bias regime). Moreover, the negative differential conductance and the associated dynamical symmetry breaking that we present in the next section are not related to the interference and can thus be obtained by considering the dynamics of the populations alone.

3.4 Transport calculations

Here we present our transport characteristics of the system for two different cases. In the first case, we consider a central system symmetrically coupled to the leads as shown in Fig. 3.1. In the second case, we consider a situation where different orbital states are differently coupled to the source and drain contacts as depicted in Fig. 3.11.

3.5 Symmetric setup

In this section, we are going to show that the additional presence of spin and/or orbital degeneracies opens the possibility of getting slow channels contributing to transport. As a consequence, NDC phenomena can occur despite a *fully symmetric* quantum-dot setup. A peculiarity of the observed features is, in particular, an asymmetry with respect to the gate voltage in the stability diagrams. Here, we present our transport characteristics and focus on the $0 \leftrightarrow 1$ transitions. In the calculation, we also assume for the coupling constant of the nth mode $g_n = \sqrt{n} g_1$ (as expected for stretching modes in carbon nanotubes [93]). The system is *symmetrically* coupled to source and drain contacts ($\gamma_{sl} = \gamma_{dl}$), see Fig. 3.1, and the lowest five vibron modes are included. Results for the differential conductance for different values of the dimensionless coupling constant λ are illustrated in Fig. 3.2 and Fig. 3.8, obtained for zero and finite orbital mismatch $\varepsilon_\Delta = \varepsilon_0 \Delta$, respectively.

3.5.1 Current-voltage characteristics at low bias with zero band mismatch

When the orbital mismatch is zero, i.e., $\varepsilon_\Delta = 0$, then the two orbital energies ε_l are the same. The minimum energy to produce a charge excitation is ε_0. We take the value of this energy as $\varepsilon_0 = 1.4$ meV (comparable to the level spacing energy of a suspended single wall carbon nanotube of 1.2 μm length). Furthermore, we assume the energy of the lowest vibronic mode to be $\varepsilon_1 = 0.04$ meV. Thus the charge excitation energy is much larger than the energy of the lowest vibron mode. Indeed, all the equidistant lines running parallel to the diamond edges observed in Fig. 3.2 are due to vibron

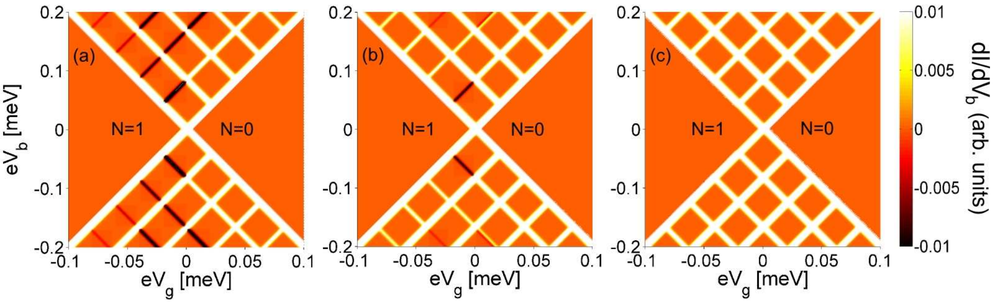

Figure 3.2: (a)-(c) Plots of the numerical differential conductance dI/dV(arbitrary units) of the system for coupling constants $\lambda = 0.68,\ 0.83$ and 1.18, respectively. The charge excitation energy is $\varepsilon_0 = 1.4$ meV and the energy of the lowest vibron mode is $\varepsilon_1 = 0.04$ meV. Additional parameters are a thermal energy of $k_{\rm B}T = 0.8$ μeV, orbital mismatch $\varepsilon_\Delta = 0$ and $\gamma_{sl} = \gamma_{dl} = 0.02$ μeV for $l = 1, 2$. The black lines running parallel to the Coulomb diamond edges correspond to negative differential conductance (NDC). Note that here and in the following figures dI/dV(arbitrary units) is normalized to the maximum of dI/dV(arbitrary units) in the considered parameter range. The gate voltage is set to zero by convention at the degeneracy point.

excited states. What striking is the occurrence of negative differential conductance (NDC) features at moderate coupling ($\lambda = 0.68$ and 0.83) which, however, disappear when the coupling is increased ($\lambda = 1.18$). Moreover, the NDC lines are only running parallel to one of the diamond edges, which indicates an asymmetry with respect to the gate voltage V_g. As we are going to explain, at low bias, these features are a consequence of Franck-Condon-assisted tunneling combined with the spin and/or orbital degeneracy in the system.

Specifically, let us focus on the low bias region, see Fig. 3.3(a), where only ground-state ↔ ground-state transitions (region A), and ground-state ↔ first excited-state transitions (regions B, C) are relevant. The 0- and 1-particle states involved are illustrated in Fig. 3.3(b), together with their degeneracy due to spin and orbital degrees of freedom, and have energies below the dashed line in Fig. 3.3(b). The states above the dashed line require an energy of at least $2\hbar\omega$ and have thus also a vibron degeneracy. In the considered energy range no degenerate vibron configurations are involved. Moreover, coherences between degenerate electronic configurations are not present such that a rate equation description only in terms of populations is appropriate. At low bias and in the stationary limit Eq. (2.35) yields the equation for the populations:

$$0 = \dot{\rho}^{E_N}_{nn} = -R^{E_N}_{nnnn}\rho^{E_N}_{nn} + \sum_{M=N\pm1}\sum_{E'}\sum_{k} R^{E_N E'_M}_{nnkk}\rho^{E'_M}_{kk}, \tag{3.20}$$

or, equivalently,

$$0 = \sum_{M=N\pm1}\sum_{E'}\sum_{k}\sum_{\alpha}\left(\Gamma^{E_N E'_M}_{\alpha,nk}\rho^{E_N}_{nn} - \Gamma^{E'_M E_N}_{\alpha,kn}\rho^{E'_M}_{kk}\right), \tag{3.21}$$

where $\Gamma^{E_N E'_M}_{\alpha,nk} \equiv 2{\rm Re}\Gamma^{(+)E_N E'_M}_{\alpha,nkkn}$ and $\Gamma^{E'_M E_N}_{\alpha,kn} \equiv 2{\rm Re}\Gamma^{(+)E'_M E_N}_{\alpha,knnk}$, see Eqs. (3.16)-(3.18). Note in particular that $\Gamma^{E_N E'_{N+1}}_{\alpha,nk} = \gamma_{\alpha l} f^+\left(E'_{N+1} - E_N - eV_\alpha\right) C_{nk}$ and $\Gamma^{E'_{N+1} E_N}_{\alpha,kn} = \gamma_{\alpha l} f^-\left(E'_{N+1} - E_N - eV_\alpha\right) C_{nk}$, i.e., they only differ in the Fermi factors. The transition

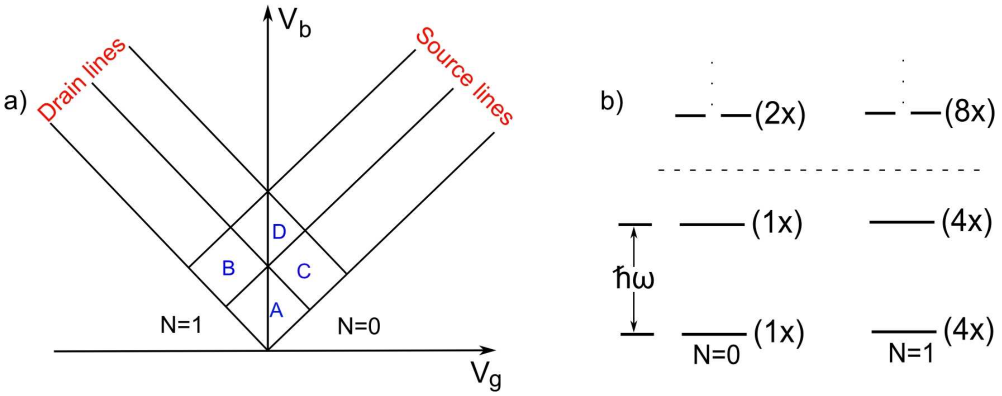

Figure 3.3: (a) The low-bias transition regions of the stability diagram are labeled as A, B, C, D. (b) Energy-level scheme for the relevant transitions in the stability diagram involving regions A-D. Above the dashed line region D is activated with two vibron modes being in the transport window. The energy of the lowest vibron mode is $\hbar\omega = 0.04$ meV. The number of degenerate states is indicated in bracket.

coefficients are the same and given by $C_{nk} = \sum_{l\sigma} \left| \left(\hat{d}_{l\sigma}\right)_{kn}^{E_N E'_{N+1}} \right|^2$. Moreover, we find for the current through lead α

$$I_\alpha = \alpha \sum_{N,E,E'} \sum_k \sum_n \left(\Gamma_{\alpha,nk}^{E_N E'_{N+1}} - \Gamma_{\alpha,kn}^{E'_{N+1} E_N} \right) \rho_{nn}^{E_N}. \tag{3.22}$$

Let us now focus on region A. In this case only the 0-particle ground state $|0,0\rangle$, see Eq. (3.11), with energy E_0^0 and the four 1-particle ground states $|1_k,0\rangle$, see Eq. (3.12), with energy E_1^0 contribute to transport. Moreover, inside region A it holds

$$\begin{aligned} &f\left(E_1^0 - E_0^0 - eV_\mathrm{s}\right) = 1, \\ &1 - f\left(E_1^0 - E_0^0 - eV_\mathrm{d}\right) = 1, \end{aligned} \tag{3.23}$$

such that, if $\gamma_{\alpha 1} = \gamma_{\alpha 2} = \gamma_\alpha$, $\gamma_\mathrm{s} = \gamma_\mathrm{d}$, it also follows ($|n\rangle = |0,0\rangle$, $|k\rangle \in \{|1_k,0\rangle\}$)

$$\sum_\alpha \Gamma_{\alpha,nk}^{E_0^0 E_1^0} = \sum_\alpha \Gamma_{\alpha,kn}^{E_1^0 E_0^0} \equiv \Gamma_{00}. \tag{3.24}$$

This situation is illustrated in the table of Fig. 3.4, where a dashed red (black) arrow indicates a transition involving the source (drain). Condition (3.24) with (3.21) then implies that

$$\rho_{nn}^{E_0^0} = \rho_{kk}^{E_1^0} \quad \forall k, \text{ and } n \tag{3.25}$$

and hence $P_0^g := \rho_{nn}^{E_0^0} = \frac{1}{5}$; $P_1^g = \sum_k \rho_{kk}^{E_1^0} = \frac{4}{5}$, yielding, with Eq. (3.22) for the current in region A, $I_A = \frac{4}{5}\Gamma_{00}$. Along similar lines we can calculate the current in regions B and C. Let us start with region B where, see table of Fig. 3.4, the gate voltage V_g is such that the 1-particle ground states $|1_k,0\rangle$ have energy E_1^0 smaller than the one, E_0^0, of the 0-particle ground state $|0,0\rangle$. Moreover, in this region also the first excited state $|1_k,1\rangle$ with energy E_1^1 enters the transport window. We also assume that the rate Γ_{11} between the states $|0,1\rangle$ and $|1_k,1\rangle$ is negligible with respect to Γ_{00} and Γ_{01}. Corrections due to a finite Γ_{11} will be discussed later. Inside region B it holds, besides Eq. (3.23), and hence Eq. (3.25), $f\left(E_1^1 - E_0^0 - eV_\mathrm{s}\right) = 1$ and $1 - f\left(E_1^1 - E_0^0 - eV_\mathrm{d}\right) = 1$. Hence, it follows that $\left(|n\rangle = |0,0\rangle,\ |k\rangle \in \left\{|1_k,1\rangle\right\}\right)$

$$\Gamma_{01} \equiv \sum_\alpha \Gamma_{\alpha,nk}^{E_0^0 E_1^1} = \sum_\alpha \Gamma_{\alpha,kn}^{E_1^1 E_0^0} \equiv \Gamma_{10}. \tag{3.26}$$

Eq. (3.21) implies thus that in region B it holds

$$\rho_{nn}^{E_0^0} = \rho_{kk}^{E_1^0} = \rho_{kk}^{E_0^1} = \frac{1}{9}, \tag{3.27}$$

and hence $P_0^g \equiv \rho_{nn}^{E_0^0} = \frac{1}{9}$, $P_1^g = \sum_k \rho_{kk}^{E_1^0} = \frac{4}{9}$, $P_1^e = \sum_k \rho_{kk}^{E_1^1} = \frac{4}{9}$. The total current in region B follows from Eq. (3.22) and reads $I_B = \frac{4}{9}\left(\Gamma_{00} + \Gamma_{01}\right)$. The condition to observe NDC is that $I_B < I_A$, which implies

$$\Gamma_{01} < \frac{4}{5}\Gamma_{00}. \tag{3.28}$$

Along similar lines, see table in Fig. 3.4, one finds for the transition from region A to C that $I_C < I_A$ if

$$\Gamma_{01} < \frac{1}{5}\Gamma_{00}. \tag{3.29}$$

Let us look in more detail at Eqs. (3.28) and (3.29). The rates Γ_{00} and Γ_{01} describe transitions between states which only differ in their vibronic part. From Eqs. (3.24), (3.26) and (3.14) it follows that

$$\frac{\Gamma_{01}}{\Gamma_{00}} = F^2\left(\lambda, 0, 1\right) = \lambda^2. \tag{3.30}$$

Hence, to observe NDC for the transition from region A to B one needs that $\lambda^2 < \frac{4}{5}$. On the other hand, for NDC in the transition from A to C we must require $\lambda^2 < \frac{1}{5}$. Indeed, as shown in Fig. 3.2, NDC for the transition A $\leftrightarrow$ B is observed for $\lambda = 0.68$ and 0.83, but it vanishes for $\lambda = 1.18$. On the other hand, NDC is never observed for the transition region A $\leftrightarrow$ C. Let us now turn to region B and to a finite $\Gamma_{11} \equiv \sum_\alpha \Gamma_{\alpha,nk}^{E_0^1 E_1^1} = \sum_\alpha \Gamma_{\alpha,kn}^{E_1^1 E_0^1}$ with $|n\rangle = |0,1\rangle$, $k \in \{|1_k,1\rangle\}$. Because now $|0,1\rangle$ can get populated, also transitions from $|0,1\rangle$ to $|1_k,0\rangle$ are activated, see Fig. 3.5.
Because of $E_0^1 - E_1^0 > eV_\mathrm{s}, eV_\mathrm{d}$ it holds

$$\tilde{\Gamma}_{10} \equiv \sum_\alpha \Gamma_{\alpha,nk}^{E_0^1 E_1^0} \neq \tilde{\Gamma}_{01} \equiv \sum_\alpha \Gamma_{\alpha,kn}^{E_1^0 E_0^1} = 0.$$

Hence, the stationary solution with equal probabilities is spoiled, at finite Γ_{11}, due to the inequality of $\tilde{\Gamma}_{01}$ and $\tilde{\Gamma}_{10}$. In fact, in the case $\Gamma_{11} = 0$, the same inequality only

Regions	Relevant transitions	P_0^g	P_0^e	P_1^g	P_1^e	I
A	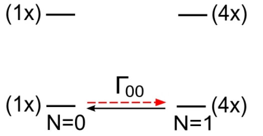	1/5	0	4/5	0	$4/5\Gamma_{00}$
B	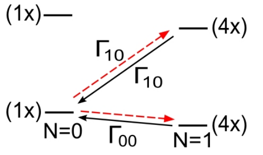	1/9	0	4/9	4/9	$4/9(\Gamma_{00}+\Gamma_{01})$
C	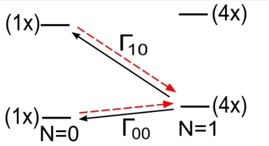	1/6	1/6	4/6	0	$4/6(\Gamma_{00}+\Gamma_{01})$

Figure 3.4: In the table for each of the different regions A, B, C in the stability diagram, relevant transitions, population of states, and current are given. P_0^g, P_0^e represent the population of the 0-particle ground and first excited states, respectively, and P_1^g, P_1^e the population of the 1-particle ground and first excited states. I is the corresponding current in each region. In the transition scheme, the black arrows represent the drain and the dashed red arrows the source transitions. Γ_{00} denotes the transition rate from 0-particle ground state to the 1-particle ground state, while Γ_{01} the transition rate from the 0-particle ground state to a 1-particle first excited state.

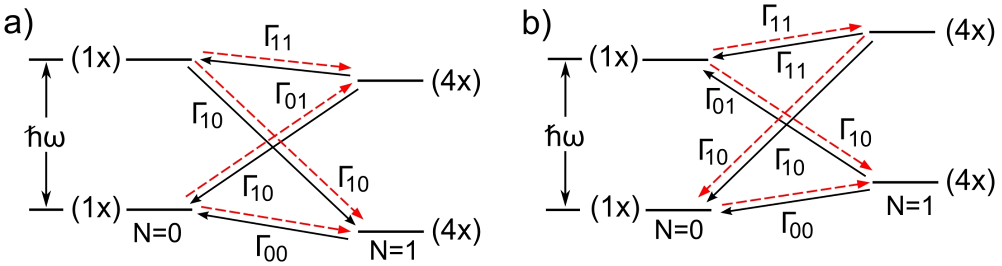

Figure 3.5: (a) Energy-level scheme for transitions in region B and (b) in region C. Importantly, because the bias voltage is too low, the transition $|1_k, 0\rangle \to |0, 1\rangle$ in region B and the transition $|0, 0\rangle \to |1_k, 1\rangle$ in region C are not allowed.

implies that $\rho^{E_0^1} = 0$. We also note that $\tilde{\Gamma}_{10} = \Gamma_{10}$. Moreover, the rates Γ_{11} and Γ_{00} only differ in their vibronic configuration: it holds, cf. Eq. (3.15)

$$\frac{\Gamma_{11}}{\Gamma_{00}} = \left[\sum_{i=0}^{1} \left(-\lambda^2\right)^i\right]^2 = \left(1 - \lambda^2\right)^2 .$$

Likewise

$$\frac{\Gamma_{11}}{\Gamma_{01}} = \frac{\left(1 - \lambda^2\right)^2}{\lambda^2} .$$

Hence, if $|\lambda| \approx 1$ it is indeed $\Gamma_{11} \ll \Gamma_{00}, \Gamma_{01}$ and an expansion to lowest order in the ratios $\frac{\Gamma_{11}}{\Gamma_{00}}, \frac{\Gamma_{11}}{\Gamma_{01}}$ can be performed. In this case the conditions for NDC acquire a more complicated form. The condition to get NDC in the source threshold lines, from A to

B in Fig. 3.3(a), is

$$\Gamma_{01} < \frac{4}{5}\Gamma_{00} - \frac{23}{40}\Gamma_{11}, \tag{3.31}$$

while the condition for NDC in the drain threshold lines, from A to C in Fig. 3.3(a), is

$$\Gamma_{01} < \frac{1}{5}\Gamma_{00} - \frac{7}{10}\Gamma_{11}. \tag{3.32}$$

It means that the presence of chain transition processes redistributes the population among the many-body states in a way that privileges the low energy states, see Fig. 3.6; this in turn weakens NDC since it privileges the conducting channels that carry more current. Eventually, let us consider explicitly the effects of the higher harmonics and of the coherences between states with different vibronic configuration on the transport characteristics of the system. In Fig. 3.7(a) we present the stability diagram for a coupling constant $\lambda = 0.68$ in which we artificially neglect the higher harmonics. By a direct comparison with Fig. 3.2(a), it is clear that this approximation only marginally affects the NDC and positive differential conductance (PDC) pattern, thus confirming the dominant role played by the spin and pseudospin (orbital) degeneracies in the gate asymmetry. The effect of the coherences, shown in Fig.3.7(b), is more complex. Nothing changes for the lowest transition lines where no degeneracy is involved. For higher biases, though, some source transition lines change their character from PDC to NDC. Thus, the gate asymmetry introduced by the spin and orbital degeneracy and the corresponding NDC (PDC) character of the source (drain) transition lines is exact in the low-bias limit but should be taken only as a trend when several excited vibronic states participate in the transport.

3.5.2 Current-voltage characteristics at low bias with finite band mismatch

In this section, we discuss our results on vibration-assisted transport with the same parameters as in Sec. 3.5.1 but with a finite orbital mismatch, i.e, $\varepsilon_\Delta \neq 0$. In this case the orbital degeneracy is broken. The corresponding stability diagrams are shown in Fig. 3.8. The analysis for the NDC conditions at low bias remains almost the same as before. Slight differences occur because in this case the orbital degeneracy is lost and the populations are redistributed over the many-body states in a different way. In Fig. 3.9(a), the different transition regions of the stability diagram have been labeled while the energy-level scheme has been shown in Fig. 3.9(b), where the degeneracy of each state is given in brackets. We again truncate the process at the dashed line to analyze the lowest-energy excitations. As before $l = 1$ and $l = 2$ are the orbital degrees of freedom. The transition scheme for regions D and F is shown explicitly in Fig. 3.10. The current-voltage characteristics Figs. 3.8(a)-(c) and 3.8(d)-3.8(f) are qualitatively the same as far as the mismatch is in the moderate regime $k_\mathrm{B}T \ll \varepsilon_\Delta < \hbar\omega$, the only difference being the position of the resonance lines, which depends on the specific position of the energy levels. In other terms, despite the size and the position of the regions of the stability diagram, see Fig. 3.8, depend on the mismatch ε_Δ, the value

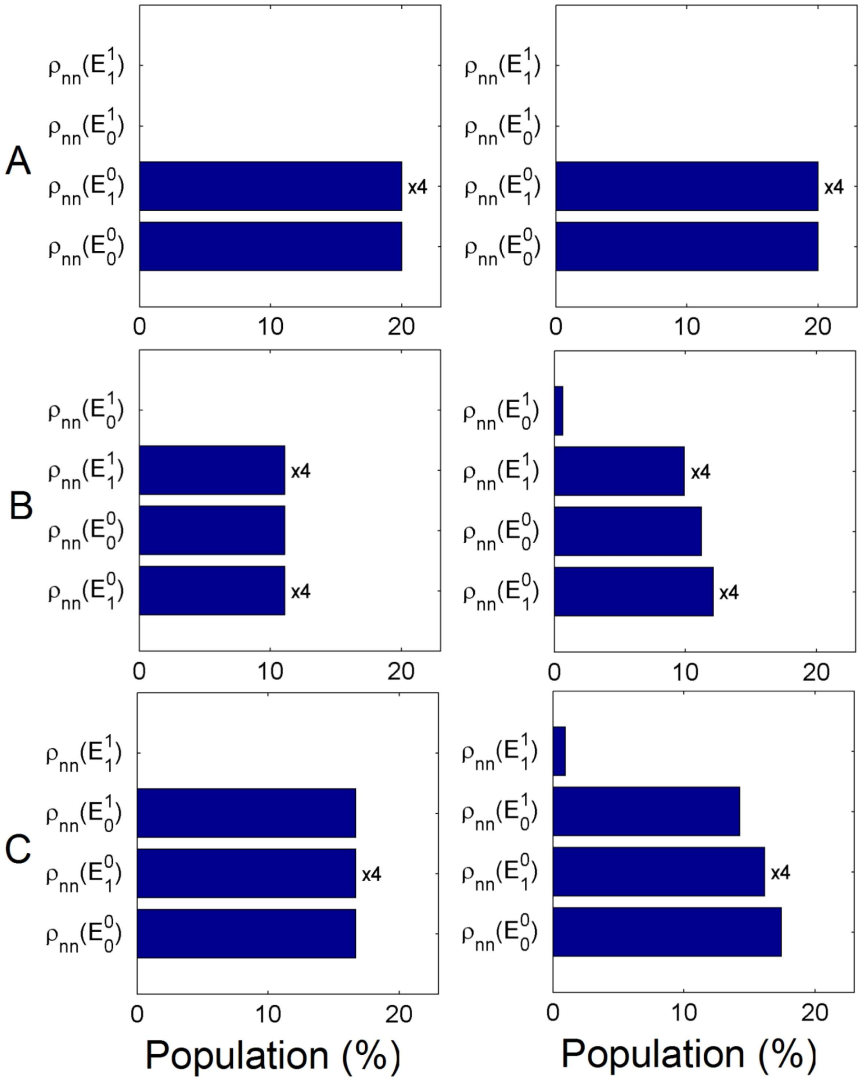

Figure 3.6: Populations of the low-energy states corresponding to the stationary density matrix calculated for different electron-vibron coupling λ and different gate-bias ranges. The first column corresponds to the case $\lambda = 1$, thus $\Gamma_{11} = 0$, while in the second column $\lambda = 0.83$. The letters A, B, C labeling the rows refer to the stability diagram regions defined in Fig. 3.3. The states are ordered in energy. The rest of the parameters are the same as used for Fig. 3.2.

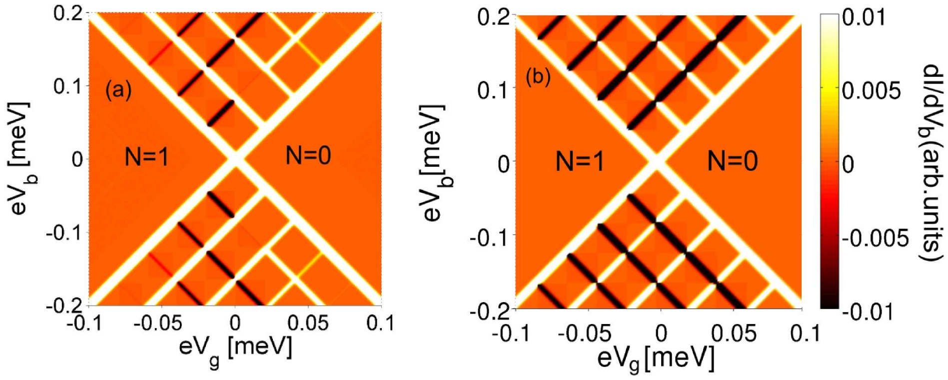

Figure 3.7: Plots of the differential conductance for a coupling constant $\lambda = 0.68$ with two different approximations: (a) neglecting the higher harmonics of the system vibrations, (b) keeping coherences between the degenerate states with different vibronic configurations. The rest of the parameters are the same as used for Fig. 3.2(a).

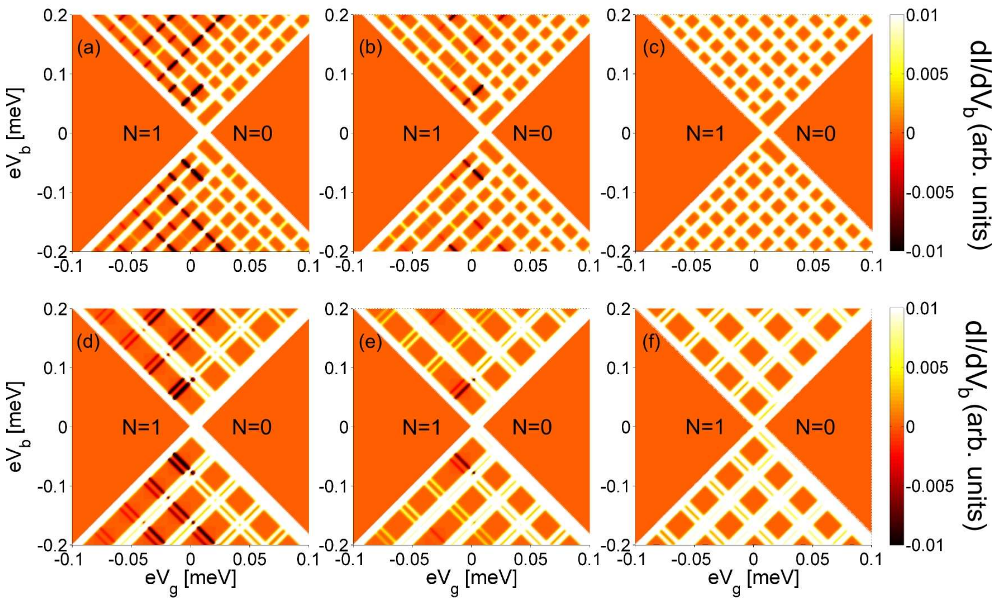

Figure 3.8: (a)-(c) Stability diagrams for coupling constants $\lambda = 0.68,\ 0.83$ and 1.18, respectively. Additional parameters are a thermal energy of $k_\mathrm{B}T = 0.8\ \mu$eV, orbital mismatch $\varepsilon_\Delta = 0.016\varepsilon_0 = 0.56\varepsilon_1$ and $\gamma_\mathrm{s} = \gamma_\mathrm{d} = 0.02\ \mu$eV while for (d)-(f) $\varepsilon_\Delta = 0.006\varepsilon_0$. The rest of the parameters are the same as used for Fig. 3.2.

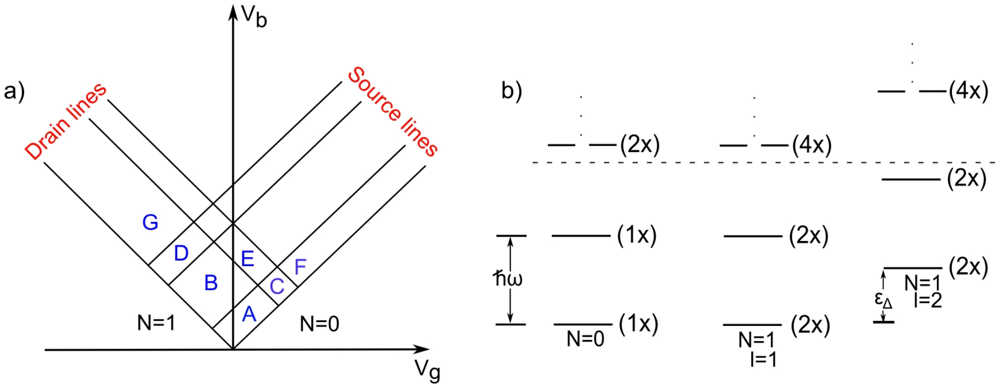

Figure 3.9: (a) The low-bias transition regions are labeled as A, B, C, D, E, F, G. (b) Energy-level scheme for the transitions relevant in the low-bias regions of the stability diagram. As in Fig. 3.3, $\hbar\omega = 0.04$ meV. The degeneracy of each state has been shown in brackets.

of the current in each region is independent of it. Thus a unified treatment of the two cases presented in Fig. 3.8 is allowed, despite their apparent qualitative differences. In particular, we can observe that the current in region B is larger than the current in region A since a new transport channel is opening with the same geometrical coupling (Γ_{00}) when passing from A to B. This implies that the first source threshold transition line is always a positive differential conductance (PDC) line. The current in C is equal to the one in A since, due to energy conservation, no new transport channel is opening when passing from A to C. The corresponding resonance line is thus invisible in the stability diagram, see Fig. 3.8. The transition that defines the threshold line separating A from C ($|1_{ke}, 0\rangle \leftrightarrow |0, 1\rangle$ at the drain) involves, in fact, states which are not populated in that bias and gate voltage range. Finally, the comparison between currents in the adjacent B and D regions and between the currents in the C and F regions results in conditions for the appearance of NDC lines which are very similar to the one in absence of mismatch. In particular, the condition for NDC at the transition between regions B and D is identical to the one for the transition between regions A and the B corresponding to zero mismatch given in Eq. (3.31). The NDC condition for the transition between region C and F reads instead

$$\Gamma_{01} < \frac{\sqrt{57}-1}{28}\Gamma_{00} + \frac{1}{4}\left(1 - \frac{3}{\sqrt{57}}\right)\Gamma_{11}, \tag{3.33}$$

to be compared with the one for the transition between the regions A and C and zero mismatch given in Eq. (3.32). A similar analysis can be repeated for higher-energy transitions which participate in the transport for higher biases. It is already clear though from the low-energy transitions that a moderate breaking of the orbital degeneracy introduced by the finite mismatch ε_Δ does not change qualitatively the transport characteristics of the system. In particular, it preserves the presence or absence of asymmetric NDC lines as a function of the electron vibron coupling λ, compare Figs. 3.2 and 3.8.

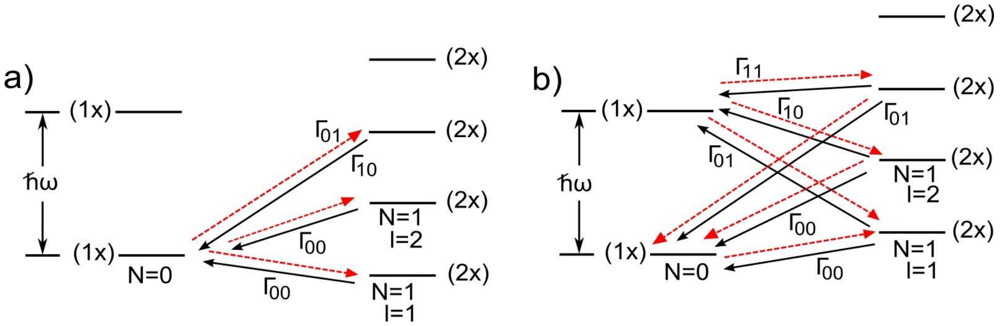

Figure 3.10: (a) Transition scheme for region D at $\varepsilon_\Delta = 0.016\varepsilon_0$. (b) Transition scheme for region F at $\varepsilon_\Delta = 0.016\varepsilon_0$.

3.6 Asymmetric setup

In some of the experiments [43, 89], the slope of the NDC lines is the same for both positive and negative biases. This characteristic has been associated with the left and right asymmetry in the coupling to the leads [89]. We confirm that including the higher harmonics does not change the effect and give an analytical interpretation of the numerical results for low biases. Hence, we retain source-drain symmetry but allow for an asymmetry in the coupling to the two orbitally degenerate states. We show that this asymmetry is sufficient to explain the experimental observations. In asymmetric setup, we consider the following two different cases:

3.6.1 Effect of an asymmetric coupling of the different orbital states to the leads

In this case, we focus on a situation in which one orbital is weakly coupled to the source and drain leads compared to the other as shown Fig. 3.11(a). The Franck Condon factors are still assumed to be the same for the source and drain tunneling and no overall asymmetry is introduced in the tunnel coupling of the molecule dot to the source and drain ($\gamma_{\mathrm{s},1/2} = \gamma_{\mathrm{d},1/2}$). The theory can produce, though, alternating PDC and NDC traces as discussed in Ref. [89] if we assume that coupling of the $l = 1$ and $l = 2$ orbitals to be different. In Fig. 3.12 we have plotted the differential conductance (dI/dV) for an asymmetry parameter $a = \frac{\gamma_{\alpha,1}}{\gamma_{\alpha,2}} = 1/45$ where "1" , "2" represent the orbital degrees of freedom, respectively and α means source or drain. For convenience, in the numerical calculations, we use parameters as in Figs. 3.2 and 3.8. As seen by comparing Fig. 3.8 with Fig. 3.12, at $\lambda = 1.18$ NDC can now occur. Moreover, an alternation of PDC with NDC lines, as seen in the experiments [43, 45, 89] occurs. Repeating the same analysis as in Sec. 3.5.2, we indeed find that: (i) the transition from region A to B gives a NDC line for $a > 3/2$ independent of the value of λ. (ii) the condition governing the transition from region B to D is now modified to be (at $\Gamma_{11} = 0$)

$$\frac{\Gamma_{01}^{(2)}}{\Gamma_{00}^{(2)}} = \lambda^2 < \frac{2+2a}{5a}, \tag{3.34}$$

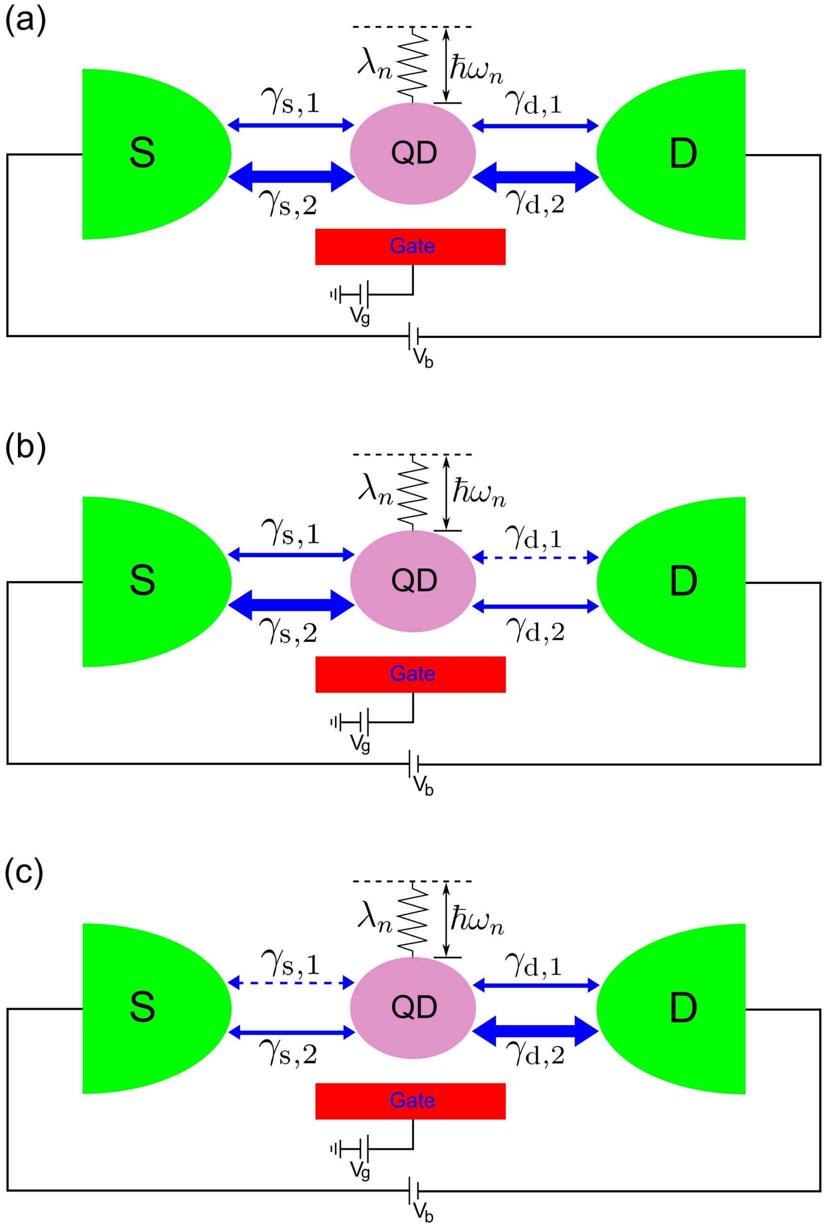

Figure 3.11: Schematic diagrams of a generic multilevel quantum dot (QD) asymmetrically coupled to the leads and capacitively coupled to a gate electrode. The dot is in turn coupled to the nth vibrational mode with energy $\hbar\omega_n$ via a dimensionless coupling constant λ_n. $\gamma_{\mathrm{s/d},1}$ and $\gamma_{\mathrm{s/d},2}$ denote coupling constants of the orbital states 1 and 2 to the source (S) and drain (D) contacts, respectively. (a) Orbitals 1 and 2 are symmetrically coupled to the source and drain leads such that orbital 1 is weaker coupled compared to orbital 2. (b) Orbitals 1 and 2 are symmetrically coupled to the source and drain, respectively, whereas orbital 2 is strongly coupled to the source and orbital 1 is weakly coupled to the drain such that both the conditions $a = \frac{\gamma_{\alpha,1}}{\gamma_{\alpha,2}} = 1/45$ and $b = \frac{\gamma_{\mathrm{s},l}}{\gamma_{\mathrm{d},l}} = 45$ are satisfied. (c) Orbitals 2 and 1 are symmetrically coupled to the source and drain, respectively, whereas orbital 2 is strongly coupled to the drain and orbital 1 is weakly coupled to the source such that both the conditions $a = \frac{\gamma_{\alpha,1}}{\gamma_{\alpha,2}} = 1/45$ and $b = \frac{\gamma_{\mathrm{s},l}}{\gamma_{\mathrm{d},l}} = 1/45$ are fulfilled.

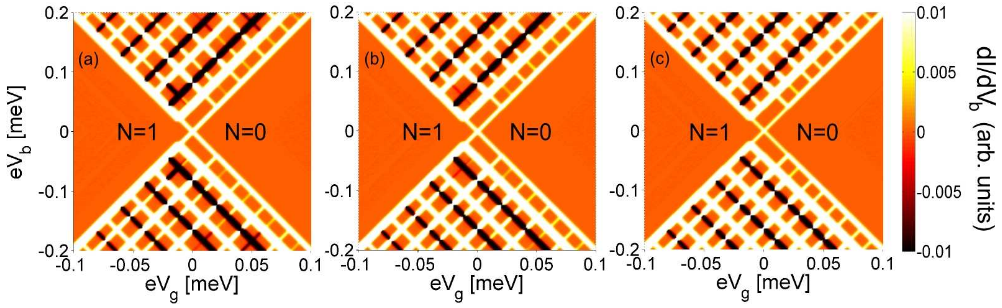

Figure 3.12: (a)-(c) Stability diagrams for a molecule for the case of a coupling to the leads which depends on the orbital degree of freedom. All the parameters are the same as used in Figs. 3.2 and 3.8. The asymmetry is $a = 1/45$ with orbital mismatch $\varepsilon_\Delta = 0.016\varepsilon_0$.

which, for $a < 1$, increases the range of λ giving NDC also for $\lambda = 1.18$, see Fig. 3.12(c). $\Gamma_{00}^{(l)}$ and $\Gamma_{01}^{(l)}$ are defined analogously Γ_{00} and Γ_{01} by considering the l dependence of the bare tunneling rates γ_l. (iii) the transition from region D to G is governed by the condition:

$$\frac{\Gamma_{01}^{(2)}}{\Gamma_{00}^{(2)}} = \lambda^2 < \frac{2(a+1)}{7-2a}, \tag{3.35}$$

which explains the persistence of a PDC line also for smaller values λ, compare again Fig. 3.8 with Fig. 3.12. The corrections introduced by a finite Γ_{11} rate do not change qualitatively the analysis and can be calculated for completeness as follows:

Here we give the conditions which determine the sign of the current change in the transition from region B to D and D to G with finite mismatch ε_Δ, see Fig. 3.9. We take only the first order contribution in the ratios Γ_{11}/Γ_{00} and Γ_{11}/Γ_{01}. The validity of these formulas is thus restricted to $\lambda \approx 1$. The condition for the transition B to D reads

$$\Gamma_{01}^{(2)} < \frac{2+2a}{5a}\Gamma_{00}^{(2)} - \frac{14+9a}{20(1+a)}\Gamma_{11}^{(2)}, \tag{3.36}$$

while for the transition D to G one obtains

$$\Gamma_{01}^{(2)} < \frac{2(a+1)}{7-2a}\Gamma_{00}^{(2)} - \frac{4a^2-16a-11}{4(a+1)(2a-7)}\Gamma_{11}^{(2)}, \tag{3.37}$$

where $a = \gamma_{\alpha 1}/\gamma_{\alpha 2}$ measures in both cases the asymmetry between the coupling to the different orbitals.

3.6.2 Effect of the asymmetric coupling to the left and right lead

In this section, we consider another asymmetric setup in which the effect of an asymmetry in the coupling to the left and right lead in combination to the orbital asymmetry discussed in the previous section is taken into account. We introduce the asymmetry via the parameter $b = \gamma_{L,l}/\gamma_{R,l}$ where $l = 1, 2$ represents the orbital degree of freedom and by convention $\gamma_{s,l} \equiv \gamma_{L,l}$ for positive bias voltages. In Fig. 3.13 we present the stability diagrams for a molecule coupled to vibrons with an orbital asymmetry $a = 1/45$

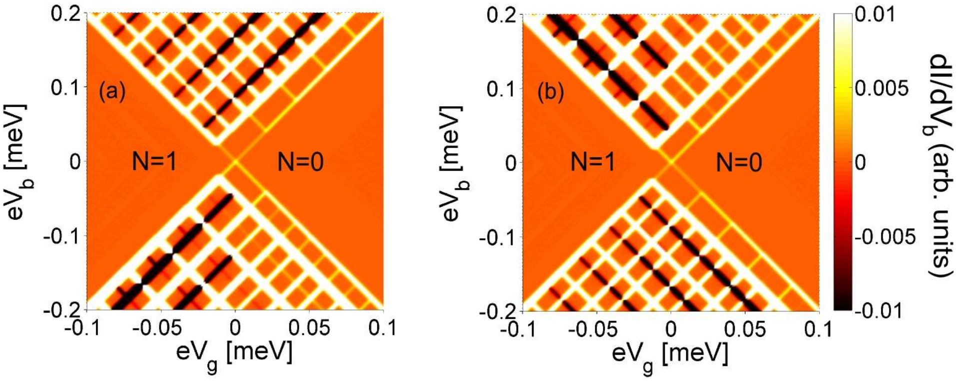

Figure 3.13: (a),(b) Stability diagrams for both an orbital and left and right asymmetry. All the parameters are the same as used in Fig. 3.12(c). The asymmetry with respect to the left and right lead is $b = 45$ in panel (a), while it is $b = 1/45$ in panel (b).

and two different left and right asymmetries. In Fig. 3.13(a) the asymmetry parameter $b = 45$, see Fig. 3.11(b), while $b = 1/45$, see Fig. 3.11(c), in Fig. 3.13(b). Since b is the only parameter of the system that breaks the left and right symmetry, the differential conductances in Fig. 3.13 can be obtained one from the other by a reflection of the bias. The most striking effect of the left and right asymmetry is, though, to produce the NDC lines always in the same direction, compare Figs. 3.12(c) and 3.13(a), both for positive and negative biases. As in the previous sections, we studied analytically the transitions lines separating the A, B, D and G low-bias regions of the stability diagram, see Fig. 3.9. We could thus obtain the NDC conditions for arbitrary values of the asymmetry parameters a and b. The transition line between region A and B is a NDC line for every electron-vibron coupling λ under the condition

$$a > \frac{2b+1}{2b}. \tag{3.38}$$

The NDC condition for the transition between the B and D region reads instead

$$\lambda^2 < \frac{2(a+1)}{a}\frac{b}{1+4b}, \tag{3.39}$$

while the transition between the regions D and G is governed by the relation

$$\lambda^2 < \frac{2(a+1)b}{1+2(3-a)b}. \tag{3.40}$$

Eqs. (3.38)-(3.40) allow a partial interpretation of the numerical results presented in Fig. 3.13. It is in fact easy to demonstrate that, if $b > 1$, for sufficiently small values of a ($a \lesssim 1/b$) the alternating NDC and PDC pattern at positive biases is not modified by the left and right asymmetry parameter b. With the help of the same set of equations and the symmetry property mentioned above we can also analyze the negative bias transitions. The sequence of transitions between regions A, B, D, and G in Fig. 3.13(b) reveals in fact a very different pattern of strong PDC transitions alternated by very weak NDC lines. This sequence can be obtained by the conditions expressed in Eqs. (3.38)-(3.40) by substituting b with $1/b$ in the limit $b \gg 1$. Unfortunately, due to the peculiar structure of the harmonic spectrum, the number of states involved in the regions E and F of the stability diagram grows rapidly and the analytical analysis of the transition, even if possible, becomes very cumbersome. Our numerical findings are nevertheless consistent with the ones reported by other groups [89], where the left and right asymmetry has been given as a necessary condition for achieving NDC with the same slope at both positive and negative biases.

The results presented in this chapter were worked out in collaboration with Andrea Donarini, Sonja Koller and Milena Grifoni. They were published in
[83] Abdullah Yar, Andrea Donarini, Sonja Koller and Milena Grifoni, Phys. Rev. B 84, 115432 (2011).

Part II

Quantum switching and memory effects in interacting quantum dots

Chapter 4

Vibration induced memory effects and switching in ac-driven molecular nanojunctions

There is a considerable excitement and interest in the area of nanoscale quantum switching. From a practical point of view, new switching paradigms are continually being explored in order to advance the current switching based memory technology. From a fundamental science point of view, the study of switching dynamics involves deep physical insight into subtle issues such as memory, bistability and hysteresis in nanoscale systems. One such experimental realization has been envisioned via molecular electronics [94–97]. Electron-vibron interaction has profound consequences on the transport characteristics of nanoelectromechanical systems [43, 44, 57, 58]. Under appropriate conditions, the system can even be driven to a bistable state where memory effects can be expected. In this respect, different theoretical approaches have been adopted to explore memory attributes in NEMS based nanojunctions [25, 98–103]. In this chapter, we investigate a vibron-mediated memory mechanism in a simple Anderson-Holstein model system. The model consists of a single level weakly coupled two metallic leads via tunnel barriers and capacitively coupled to a gate electrode that modulates its electrostatic potential. In addition, the dot is coupled to a vibrational mode as shown in Fig. 4.1.

4.1 The model

We consider a simple Anderson-Holstein model which appropriately describes transport through vibrating quantum dots with a discrete spectrum. The Hamiltonian of the central system is described as

$$\hat{H}_{\mathrm{sys}} = \hat{H}_{\mathrm{mol}} + \hat{H}_{\mathrm{v}} + \hat{H}_{\mathrm{e\text{-}v}}, \tag{4.1}$$

where $\hat{H}_{\mathrm{mol}}$ represents a spinless single molecular level modeled by the Hamiltonian

$$\hat{H}_{\mathrm{mol}} = (\varepsilon_0 + eV_{\mathrm{g}})\, \hat{d}^{\dagger}\hat{d}, \tag{4.2}$$

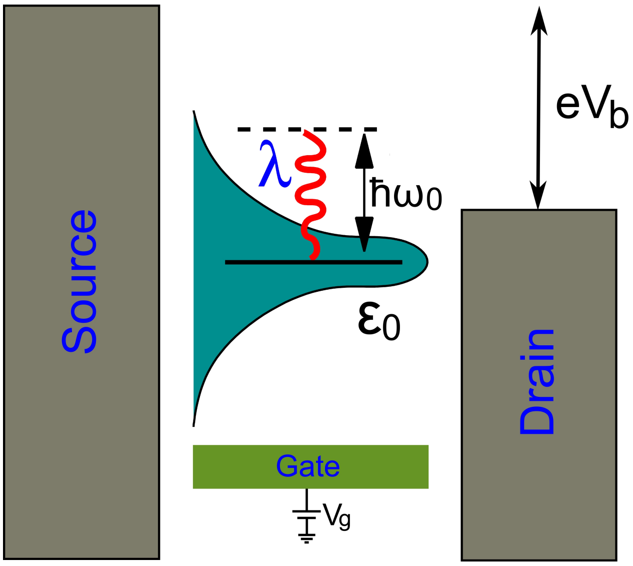

Figure 4.1: Schematic diagram of the system where a single level with energy ε_0 is coupled to a vibrational mode with energy $\hbar\omega_0$ via a dimensionless coupling constant λ. The energy level is broadened due to coupling to the leads. In turn the electrostatic potential of the dot is controlled by a gate electrode.

where $\hat{d}^\dagger(\hat{d})$ is the creation (annihilation) operator of an electron on the molecule and ε_0 is the energy of the molecular level, and V_g accounts for an externally applied gate voltage. Here we assume a strong Coulomb interaction, $U \to \infty$, i.e., we have at most one excess charge localized on the molecule. This approximation is appropriate when $eV_\mathrm{b}, k_\mathrm{B}T \ll U$, with V_b being the bias voltage drop between the leads. The vibron Hamiltonian can be written as

$$\hat{H}_\mathrm{v} = \hbar\omega_0 \left(\hat{a}^\dagger\hat{a} + \frac{1}{2}\right), \tag{4.3}$$

where $\hat{a}^\dagger(\hat{a})$ creates (annihilates) a vibron with energy $\hbar\omega_0$. Finally, the electron-vibron interaction Hamiltonian is expressed as

$$\hat{H}_\text{e-v} = g\hat{d}^\dagger\hat{d}\left(\hat{a}^\dagger + \hat{a}\right), \tag{4.4}$$

where g is a coupling constant. This model assumes that transport occurs through an electronic state coupled to a single vibrational mode.

4.1.1 Diagonalization of the system Hamiltonian

To study the transport features of the system, the spectrum of the Hamiltonian described by Eq. (4.1) is required which can be achieved by eliminating the electron-vibron interaction in the same way as explained in Chapter 3. Hence, for the decoupling of electron-vibron interaction Hamiltonian, we apply the canonical polaron unitary transformation [56]. Explicitly, we set $\tilde{\hat{H}}_\mathrm{sys} = e^{\hat{S}}\hat{H}_\mathrm{sys}e^{-\hat{S}}$, where

$$\hat{S} = \lambda\hat{d}^\dagger\hat{d}\left(\hat{a}^\dagger - \hat{a}\right), \tag{4.5}$$

with $\lambda = \frac{g}{\hbar\omega_0}$ as the dimensionless coupling constant. The transformed form of the electron operator is

$$\tilde{\hat{d}} = \hat{d}\hat{X}, \tag{4.6}$$

where $\hat{X} = \exp\left[-\lambda\left(\hat{a}^\dagger - \hat{a}\right)\right]$. In a similar way, the vibron operator is transformed as

$$\tilde{\hat{a}} = \hat{a} - \lambda\hat{d}^\dagger\hat{d}. \tag{4.7}$$

Now the transformed form of the system Hamiltonian reads

$$\tilde{\hat{H}}_{\mathrm{sys}} = \varepsilon\hat{d}^\dagger\hat{d} + \hbar\omega_0\left(\hat{a}^\dagger\hat{a} + \frac{1}{2}\right), \tag{4.8}$$

where $\varepsilon = \varepsilon_0 + eV_{\mathrm{g}} - \frac{g^2}{\hbar\omega_0}$ is the polaron energy with polaron shift $\varepsilon_{\mathrm{p}} = \frac{g^2}{\hbar\omega_0}$. The polaron eigenstates of the system are

$$|n, m\rangle_1 := e^{-\hat{S}}|n, m\rangle, \tag{4.9}$$

where n denotes the number of electrons on the molecular quantum dot, whereas the quantum number m characterizes a vibrational excitation induced by the electron transfer to or from the dot.

4.2 Sequential transport

We are interested to analyze the transport properties of the system in the limit of weak coupling to the leads. The Hamiltonian of the full system is described in the form

$$\hat{H}(t) = \hat{H}_{\mathrm{sys}} + \hat{H}_{\mathrm{T}} + \sum_{\alpha}\hat{H}_\alpha(t), \tag{4.10}$$

where $\alpha = \mathrm{s}, \mathrm{d}$ denotes the source and the drain contacts, respectively. The tunneling Hamiltonian is given by

$$\hat{H}_{\mathrm{T}} = \sum_{\alpha\kappa} t_\alpha\left(\hat{c}^\dagger_{\alpha\kappa}\hat{d} + \hat{d}^\dagger\hat{c}_{\alpha\kappa}\right), \tag{4.11}$$

where $\hat{c}^\dagger_{\alpha\kappa}(\hat{c}_{\alpha\kappa})$ creates (annihilates) an electron in lead α. The coupling between molecule and leads is parametrized by the tunneling matrix elements t_{s} and t_{d}. Here, we consider the weak coupling regime so that the energy broadening $\hbar\Gamma$ of molecular levels due to $\hat{H}_{\mathrm{T}}$ is small, i.e., $\hbar\Gamma \ll \hbar\omega_0, k_{\mathrm{B}}T$, and a perturbative treatment for $\hat{H}_{\mathrm{T}}$ in the framework of rate equations is appropriate. For simplicity, we assume that the tunneling amplitude $t_{\mathrm{s/d}}$ of lead s/d is real and independent of the momentum $\hbar\kappa$ of the lead state. In addition, we consider a symmetric device with $t_{\mathrm{s}} = t_{\mathrm{d}}$. Finally, the time dependent lead Hamiltonian is described by

$$\hat{H}_\alpha(t) = \sum_{\kappa}\left[\varepsilon_\kappa + \Delta\mu_\alpha(t)\right]\hat{c}^\dagger_{\alpha\kappa}\hat{c}_{\alpha\kappa}. \tag{4.12}$$

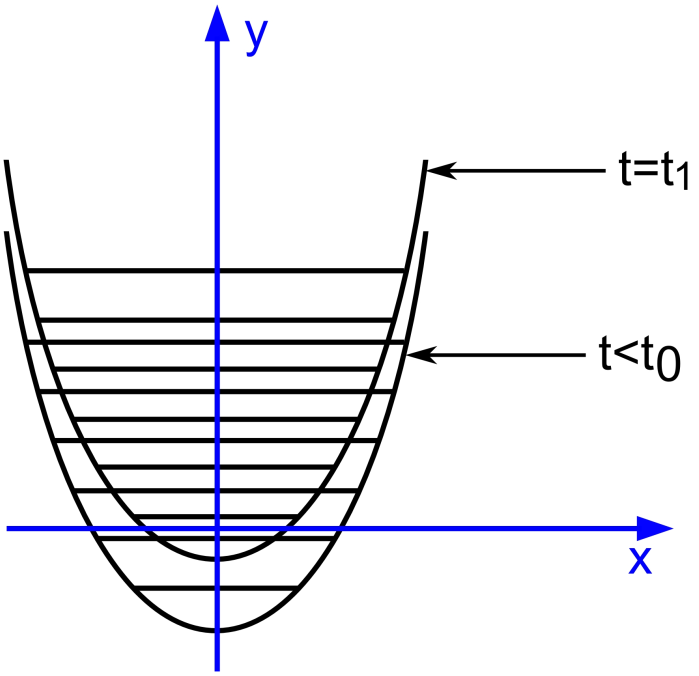

Figure 4.2: Schematic representation for the κ-independent shift of all single-particle levels of the lead in the vertical direction, i.e., along y-axis.

The above equation describes the lead Hamiltonian of non-interacting electrons with dispersion relation ε_κ. The time-varying chemical potential $\Delta\mu_\alpha(t)$ of lead α depends on the applied bias voltage, and yields κ-independent shift of all the single-particle levels as schematically shown in Fig. 4.2.

4.2.1 Time dependent master equation

In this section, we calculate the dynamics of the system in the same way as discussed in Chapter 2. However, in this chapter the equation of motion for the reduced density matrix (RDM) of the molecular junction is solved accounting for the time-dependence, Eq. (4.12), of the leads Hamiltonian $\hat{H}_\alpha(t)$. We also derive the important time scale relations which govern the switching dynamics of the system. Hence, we start with the well known Liouville equation for the time evolution of the density matrix for the full system consisting of the leads and the generic quantum dot as

$$i\hbar\frac{\partial\hat{\rho}^I_{\text{red}}(t)}{\partial t} = \text{Tr}_{\text{leads}}\left[\hat{H}^I_{\text{T}}(t), \hat{\rho}^I(t)\right], \tag{4.13}$$

for the reduced density matrix $\hat{\rho}_{\text{red}}(t) = \text{Tr}_{\text{leads}}\left\{\hat{\rho}(t)\right\}$ in interaction picture, where the trace over the leads degrees of freedom is taken. In the above equation, $\hat{H}^I_{\text{T}}(t)$ is the tunneling Hamiltonian in the interaction picture to be calculated as below:

$$\hat{H}^I_{\text{T}}(t) = \sum_{\alpha\kappa} t_\alpha\left[\hat{c}^\dagger_{\alpha\kappa}\hat{d}(t)e^{\frac{i}{\hbar}[\varepsilon_\kappa t+\zeta_\alpha(t)]} + \text{h.c.}\right], \tag{4.14}$$

where $\zeta_\alpha(t) = \int_{t_0}^{t} \Delta\mu_\alpha(t')\mathrm{d}t'$. We make the following standard approximations to solve the above equation: (i) The leads are considered as reservoirs of noninteracting electrons in adiabatic thermal equilibrium. Note that this implies that the time scale of variation of the external perturbation has to be large compared to the relaxation time scale of the reservoirs, cf. Eq. (4.19) below. We assume the coupling between system and reservoirs has been switched on at time $t = t_0$ and consider a factorized initial condition. Thus at times $t \geq t_0$ it holds $\rho^I(t) = \rho^I_{\mathrm{sys}}(t) \otimes \rho_{\mathrm{s}}\rho_{\mathrm{d}} + \theta(t - t_0)O(\hat{H}_{\mathrm{T}}) := \rho^I_{\mathrm{sys}}(t) \otimes \rho_{\mathrm{leads}} + \theta(t - t_0)O(\hat{H}_{\mathrm{T}})$. Here $\rho_{\mathrm{s/d}} = \frac{1}{Z_{\mathrm{s/d}}} e^{-\beta(\hat{H}_{\mathrm{s/d}}(t) - \mu_{\mathrm{s/d}}(t)\hat{\mathcal{N}}_{\mathrm{s/d}})}$ denotes the thermal equilibrium grandcanonical distribution of lead s/d, $Z_{\mathrm{s/d}}$ is the partition function, β the inverse of the thermal energy, $\hat{\mathcal{N}}_{\mathrm{s/d}}$ the electron number operator, and $\mu_{\mathrm{s/d}}(t) = \mu_0 + \Delta\mu_{\mathrm{s/d}}(t)$ is the time dependent chemical potential of lead s/d which depends on the applied bias voltage. Note that the levels shift is taken into account by the time-dependent perturbation $\Delta\mu_{\mathrm{s/d}}(t)$, while the change in chemical potential is taken into account accordingly via the chemical potential $\mu_{\mathrm{s/d}}(t)$ so that the net positive or negative charge accumulation in the leads is avoided. Conventionally, we take the molecular energy levels as a fixed reference and let the bias voltage drop across the source and drain contacts through the Fermi energies as [104]

$$\begin{aligned}
\mu_{\mathrm{s}}(t) &= \mu_0 + (1 - \eta)eV_{\mathrm{b}}(t), \\
\mu_{\mathrm{d}}(t) &= \mu_0 - \eta eV_{\mathrm{b}}(t),
\end{aligned} \tag{4.15}$$

where $0 \leq \eta \leq 1$ describes the symmetry of the voltage drop across the junction. Specifically, $\eta = 0$ corresponds to the most asymmetric situation, while $\eta = 1/2$ represents the symmetric case. In addition, we consider a sinusoidally-varying bias voltage, i.e., $V_{\mathrm{b}}(t) = V_0 \sin(\omega t)$, where ω is the frequency of the driving field. (ii) Since we assume weak coupling of the molecule to the leads, we treat the effects of $\hat{H}_T$ perturbatively up to second order. Accounting for the time-evolution as in Eq. (4.14) of the leads creation/annihilation operators, we find:

$$\begin{aligned}
\dot{\hat{\rho}}^I_{\mathrm{red}}(t) = -\sum_{\alpha\kappa} \frac{|t_\alpha|^2}{\hbar^2} \int_{t_0}^{t} \mathrm{d}t' \Big\{ & f_\alpha(\varepsilon_\kappa - \mu_0)\, \hat{d}(t)\hat{d}^\dagger(t')\hat{\rho}^I_{\mathrm{red}}(t') \\
& \times e^{\frac{i}{\hbar}[\varepsilon_\kappa(t-t') + \zeta_\alpha(t) - \zeta_\alpha(t')]} + [1 - f_\alpha(\varepsilon_\kappa - \mu_0)] \\
& \times \hat{d}^\dagger(t)\hat{d}(t')\hat{\rho}^I_{\mathrm{red}}(t') e^{-\frac{i}{\hbar}[\varepsilon_\kappa(t-t') + \zeta_\alpha(t) - \zeta_\alpha(t')]} \\
& - [1 - f_\alpha(\varepsilon_\kappa - \mu_0)]\, \hat{d}(t)\hat{\rho}^I_{\mathrm{red}}(t')\hat{d}^\dagger(t') \\
& \times e^{\frac{i}{\hbar}[\varepsilon_\kappa(t-t') + \zeta_\alpha(t) - \zeta_\alpha(t')]} - f_\alpha(\varepsilon_\kappa - \mu_0)\, \hat{d}^\dagger(t) \\
& \times \hat{\rho}^I_{\mathrm{red}}(t')\hat{d}(t') e^{-\frac{i}{\hbar}[\varepsilon_\kappa(t-t') + \zeta_\alpha(t) - \zeta_\alpha(t')]} + \mathrm{h.c} \Big\}.
\end{aligned} \tag{4.16}$$

In the derivation of the above equation we have used the relation: $\mathrm{Tr}_{\mathrm{leads}} \left\{ \hat{c}^\dagger_{\alpha\kappa}\hat{c}_{\alpha'\kappa'}\hat{\rho}_{\mathrm{s}}\hat{\rho}_{\mathrm{d}} \right\} = \delta_{\alpha\alpha'}\delta_{\kappa\kappa'} f(\varepsilon_\kappa - \mu_0)$, where $f(\varepsilon_\kappa - \mu_0)$ is the Fermi function, and the cyclic property of the trace. By summing over κ we obtain the generalized master equation (GME) for the reduced density matrix in the form

$$\begin{aligned}\dot{\hat{\rho}}^I_{\text{red}}(t) = -\sum_\alpha \frac{|t_\alpha|^2}{\hbar^2}\int_{t_0}^{t}\mathrm{d}t'\Big\{ & F_\alpha(t-t',\mu_0)\hat{d}(t)\hat{d}^\dagger(t')\hat{\rho}^I_{\text{red}}(t')e^{\frac{i}{\hbar}[\zeta_\alpha(t)-\zeta_\alpha(t')]}\\ & + F_\alpha(t-t',-\mu_0)\hat{d}^\dagger(t)\hat{d}(t')\hat{\rho}^I_{\text{red}}(t')e^{-\frac{i}{\hbar}[\zeta_\alpha(t)-\zeta_\alpha(t')]}\\ & - F^*_\alpha(t-t',-\mu_0)\hat{d}(t)\hat{\rho}^I_{\text{red}}(t')\hat{d}^\dagger(t')e^{\frac{i}{\hbar}[\zeta_\alpha(t)-\zeta_\alpha(t')]}\\ & - F^*_\alpha(t-t',\mu_0)\hat{d}^\dagger(t)\hat{\rho}^I_{\text{red}}(t')\hat{d}(t')e^{-\frac{i}{\hbar}[\zeta_\alpha(t)-\zeta_\alpha(t')]} + \text{h.c}\Big\},\end{aligned} \tag{4.17}$$

where the correlation function $F_\alpha(t-t',\mu_0)$ of lead α whose detailed derivation is given in Chapter 2 has, in the wide band limit, the following form:

$$F_\alpha\big(t-t',\mu_0\big) = \pi\hbar D_\alpha e^{i\frac{\mu_0}{\hbar}(t-t')}\bigg\{\delta\big(t-t'\big) - \frac{i}{\hbar\beta\sinh\big[\pi\frac{(t-t')}{\hbar\beta}\big]}\bigg\}, \tag{4.18}$$

which decays with the time difference $t-t'$ approximately as $\exp\Big[-\pi\frac{(t-t')}{\hbar\beta}\Big]$ on the time scale $\frac{\hbar\beta}{\pi}$. Here D_α is the density of states of lead α at the Fermi level. (iii) Since we are interested in the long-term dynamical behavior of the system, we set $t_0 \to -\infty$ in Eq. (4.17). Furthermore, we replace t' by $t-t''$. We then apply the Markov approximation, where the time evolution of $\hat{\rho}^I_{\text{red}}$ is taken only local in time, meaning we approximate $\hat{\rho}_{\text{red}}(t-t'') \sim \hat{\rho}_{\text{red}}(t)$ in Eq. (4.17). In general, the condition of time locality requires that [88]

$$\Gamma, \omega \ll \frac{\pi}{\hbar\beta}. \tag{4.19}$$

Here we defined from Eq. (4.17) together with Eq. (4.18), $\Gamma_\alpha = \frac{2\pi}{\hbar}|t_\alpha|^2 D_\alpha$ as the bare transfer rates and $\hbar\Gamma = \sum_\alpha \hbar\Gamma_\alpha$ as the tunneling-induced level width. Finally, the condition of adiabatic driving Eq. (4.19) allows to approximate $\zeta_\alpha(t) - \zeta_\alpha(t-t'') = \Delta\mu_\alpha(t)t''$. Taking into account these simplifications, the generalized master equation (GME) for the reduced density matrix acquires the form

$$\begin{aligned}\dot{\hat{\rho}}^I_{\text{red}}(t) = -\sum_\alpha \frac{|t_\alpha|^2}{\hbar^2}\int_0^\infty \mathrm{d}t''\Big\{ & F[t'',\mu_\alpha(t)]\hat{d}(t)\hat{d}^\dagger(t-t'')\hat{\rho}^I_{\text{red}}(t)\\ & + F[t'',-\mu_\alpha(t)]\hat{d}^\dagger(t)\hat{d}(t-t'')\hat{\rho}^I_{\text{red}}(t)\\ & - F^*[t'',-\mu_\alpha(t)]\hat{d}(t)\hat{\rho}^I_{\text{red}}(t)\hat{d}^\dagger(t-t'')\\ & - F^*[t'',\mu_\alpha(t)]\hat{d}^\dagger(t)\hat{\rho}^I_{\text{red}}(t)\hat{d}(t-t'') + \text{h.c.}\Big\},\end{aligned} \tag{4.20}$$

where $F[t'',\mu_\alpha(t)] = F_\alpha(t'',\mu_0)e^{\frac{i}{\hbar}\Delta\mu_\alpha(t)t''}$.

Since the eigenstates $|n,m\rangle_1$ of $\hat{H}_{\text{sys}}$ are known, it is convenient to calculate the time evolution of $\hat{\rho}^I_{\text{red}}$ in this basis. For a generic quantum dot system, this projection yields a set of differential equations coupling diagonal (populations) and off-diagonal (coherences) components of the RDM. For the simple Anderson-Holstein model Eq. (4.1) coherences and populations are, however, decoupled. In the sequential-tunneling regime, the master equation for the occupation probabilities $P_n^m = {}_1\langle n, m|\hat{\rho}_{\text{red}}|n, m\rangle_1$ of finding the system in one of the polaron eigenstates assumes the form

$$\dot{P}_n^m = \sum_{n',m'} \Gamma_{n'\to n}^{m'\to m}(t) P_{n'}^{m'} - \sum_{n',m'} \Gamma_{n\to n'}^{m\to m'}(t) P_n^m. \tag{4.21}$$

Here, the coefficient $\Gamma_{n'\to n}^{m'\to m}$ denotes the transition rate from $|n', m'\rangle_1$ into the many body state $|n, m\rangle_1$, while $\Gamma_{n\to n'}^{m\to m'}$ describes the transition rate out of the state $|n, m\rangle_1$ to $|n', m'\rangle_1$. Taking into account all possible single-electron-tunneling processes, we obtain the incoming and outgoing tunneling rates, in the wide band limit, as

$$\begin{aligned} \Gamma_{0\to 1}^{m\to m'}(t) &= \sum_\alpha \Gamma_\alpha F_{mm'} f^+\big[\varepsilon + \hbar\omega_0 (m' - m) - \mu_\alpha(t)\big] \\ &\equiv \sum_\alpha \Gamma_{\alpha,0\to 1}^{m\to m'}(t), \end{aligned} \tag{4.22}$$

$$\begin{aligned} \Gamma_{1\to 0}^{m'\to m}(t) &= \sum_\alpha \Gamma_\alpha F_{mm'} f^-\big[\varepsilon + \hbar\omega_0 (m' - m) - \mu_\alpha(t)\big] \\ &\equiv \sum_\alpha \Gamma_{\alpha,1\to 0}^{m'\to m}(t), \end{aligned} \tag{4.23}$$

where the terms describing sequential tunneling from and to the lead α are proportional to the Fermi functions $f^+(x - \mu_\alpha) = f(x - \mu_\alpha)$ and $f^-(x - \mu_\alpha) = 1 - f(x - \mu_\alpha)$, respectively. The factor $F_{mm'} = |\langle m|\hat{X}|m'\rangle|^2$ is the Franck-Condon matrix element which can be calculated, with $\hat{X}$ defined in Sec. 4.1.1, explicitly by determining the matrix elements

$$\langle r|\hat{d}|s\rangle = e^{-\frac{1}{2}|\lambda|^2} F(\lambda, m, m'), \tag{4.24}$$

where $|r\rangle$ and $|s\rangle$ represent the eigenstates given by Eq. (4.9). The function $F(\lambda, m, m')$ determines the coupling between states with a different vibronic number of excitations with effective coupling λ and is given by Eq. (3.15). Consequently, the FC factor $F_{mm'}$ is defined as

$$F_{mm'} = e^{-\lambda^2} F^2(\lambda, m, m'). \tag{4.25}$$

The sum rules $\sum_m F_{mm'} = \sum_{m'} F_{mm'} = 1$ are well satisfied because of the completeness of each vibrational basis set $\{|0, m\rangle\}$ and $\{|1, m'\rangle_1\}$. This factor describes the wavefunction overlap between the vibronic states participating in the particular transition. It contains essential information about the quantum mechanics of the molecule and significantly influences the transport properties of the single-molecule junction. Within the rate-equation approach, the (particle) current through lead α is determined by, cf. Eq. (2.41)

$$I_\alpha(t) = \sum_{mm'} \left(\Gamma^{m\to m'}_{\alpha,0\to 1}(t) P^m_0(t) - \Gamma^{m'\to m}_{\alpha,1\to 0}(t) P^{m'}_1(t) \right). \tag{4.26}$$

and it is in general time dependent. Moreover, differently from the stationary case, in general $I_L(t) \neq -I_R(t)$. The charge is though not accumulating on the dot since, for the average quantities

$$I_{\alpha,\mathrm{av}} = \lim_{t\to\infty} \int_t^{t+T_{\mathrm{ex}}} \mathrm{d}t' I_\alpha(t') \tag{4.27}$$

it holds $I_{L,\mathrm{av}} = -I_{R,\mathrm{av}}$, as it can be easily proved considering that the average charge on the dot oscillates with the same period T_{ex} of the driving bias. Finally, in the DC limit $\omega \to 0$ the relation $I_L(t) = -I_R(t)$ holds as the fully adiabatic driving allows to reach the quasi-stationary limit at all times.

4.3 Lifetimes and bistability of states

In this section, we show that when the bias voltage drop is asymmetric across the junction, upon sweeping the bias, one can tune the lifetime of the neutral and charged states to achieve a bistable system. The lifetime of a state is obtained by calculating the switching rate of that state. The lifetime τ_{nm} of a generic quantum state $|n,m\rangle_1$ is given by the sum of the rates of all possible processes which change this state, i.e.,

$$\tau^{-1}_{nm} = \sum_{n',m'} \Gamma^{m\to m'}_{n\to n'}. \tag{4.28}$$

Thus, at finite bias voltage, the inverse lifetime of the 0-particle mth vibronic state is given by the relation

$$\tau^{-1}_{0m} = \sum_{\alpha,m'} \Gamma_\alpha F_{mm'} f^+ \left[\varepsilon + \hbar\omega_0 \left(m' - m\right) - \mu_\alpha\right]. \tag{4.29}$$

In a similar way, the inverse lifetime of the 1-particle and mth vibronic state is expressed as

$$\tau^{-1}_{1m} = \sum_{\alpha,m'} \Gamma_\alpha F_{mm'} f^- \left[\varepsilon + \hbar\omega_0 \left(m - m'\right) - \mu_\alpha\right]. \tag{4.30}$$

A consequence of Eqs. (4.29) and (4.30) is that, due to the characteristic features of the Franck-Condon matrix elements, in the strong electron-vibron coupling regime, the tunneling with small changes in $m - m'$ is suppressed exponentially. Hence, only some selected vibronic states contribute to the tunneling process. However, tunneling also depends on the bias voltage and temperature through the Fermi function. To proceed further, let us focus first on the lifetime of the 0- and 1-particle ground states for the case of fully asymmetric coupling of the bias voltage to the leads, i.e., $\eta = 0$:

$$\begin{aligned}\tau_{00}^{-1} = &\sum_{m'} \frac{e^{-\lambda^2}\lambda^{2m'}}{m'!}\big\{\Gamma_{\mathrm{s}} f^{+}\left(\varepsilon + m'\hbar\omega_0 - \mu_0 - eV_{\mathrm{b}}\right) \\ &+ \Gamma_{\mathrm{d}} f^{+}\left(\varepsilon + m'\hbar\omega_0 - \mu_0\right)\big\},\end{aligned} \tag{4.31}$$

$$\begin{aligned}\tau_{10}^{-1} = &\sum_{m'} \frac{e^{-\lambda^2}\lambda^{2m'}}{m'!}\big\{\Gamma_{\mathrm{s}} f^{-}\left(\varepsilon - m'\hbar\omega_0 - \mu_0 - eV_{\mathrm{b}}\right) \\ &+ \Gamma_{\mathrm{d}} f^{-}\left(\varepsilon - m'\hbar\omega_0 - \mu_0\right)\big\}.\end{aligned} \tag{4.32}$$

One can see from Eq. (4.31) that if in the considered parameters range is $\varepsilon + m'\hbar\omega_0 \gg \mu_0$, i.e., $f\left(\varepsilon + m'\hbar\omega_0 - \mu_0\right) \to 0$, then the second term in the bracket is negligible. The first term is nonzero at large positive bias, while at large negative bias it remains negligible. In a similar way one can analyze the behavior of τ_{10}^{-1} in which the first term on the r.h.s. of Eq. (4.32) will be dominating at large negative bias. In order to understand the mechanism of this process the energy-level scheme for the relevant transitions in a coordinate system given by the particle number N and the grand-canonical energy $E - \mu_0 N$ shown in Fig. 4.3. We choose $V_{\mathrm{g}} = 0$ and $\mu_0 = 0$. Moreover, the polaron energy levels are at resonance with the 0-particle states for our chosen set of parameters: we set $\varepsilon_{\mathrm{p}} = \varepsilon_0$ and hence $\varepsilon = 0$. Then the only transitions allowed at zero bias are ground state ↔ ground state transitions. At finite bias also transitions involving excited vibronic states become allowed. In particular, at $V_{\mathrm{b}} = 0$ it follows from Eqs. (4.31), and (4.32) that

$$\tau_{00}^{-1}(V_{\mathrm{b}} = 0) = \tau_{10}^{-1}(V_{\mathrm{b}} = 0) = e^{-\lambda^2}(\Gamma_{\mathrm{s}} + \Gamma_{\mathrm{d}})/2, \tag{4.33}$$

while at $|V_{\mathrm{b}}| \to \infty$ it holds

$$\begin{aligned}\tau_{00}^{-1}(V_{\mathrm{b}} \to \infty) &= \tau_{10}^{-1}(V_{\mathrm{b}} \to -\infty) \\ &= \Gamma_{\mathrm{s}} + \frac{\Gamma_{\mathrm{d}}}{2} e^{-\lambda^2} \sim \Gamma_{\mathrm{s}} \equiv \tau_{\min}^{-1},\end{aligned} \tag{4.34}$$

whereas

$$\tau_{00}^{-1}(V_{\mathrm{b}} \to -\infty) = \tau_{10}^{-1}(V_{\mathrm{b}} \to \infty) = \frac{\Gamma_{\mathrm{d}}}{2} e^{-\lambda^2} \equiv \tau_{\max}^{-1}. \tag{4.35}$$

In practice the asymptotic behaviors are already reached at $e|V_{\mathrm{b}}|/\hbar\omega_0 \sim 2\lambda^2$ as observed in Fig. 4.3(b). Note that $\tau_{\max}$ and $\tau_{\min}$ set the maximum and minimum achievable lifetimes which, due to $\tau_{\max}/\tau_{\min} \sim e^{\lambda^2}$, can differ by several orders of magnitude for $\lambda > 1$. Note also that near zero bias the lifetimes are so long that the system never likes to charge or discharge and a bistable situation is reached. A selective switching, however, can occur upon sweeping the bias voltage. Hence, $\tau_{\min}$ also sets the time scale for switching: $\tau_{\min} \sim \tau_{\mathrm{switch}}$.

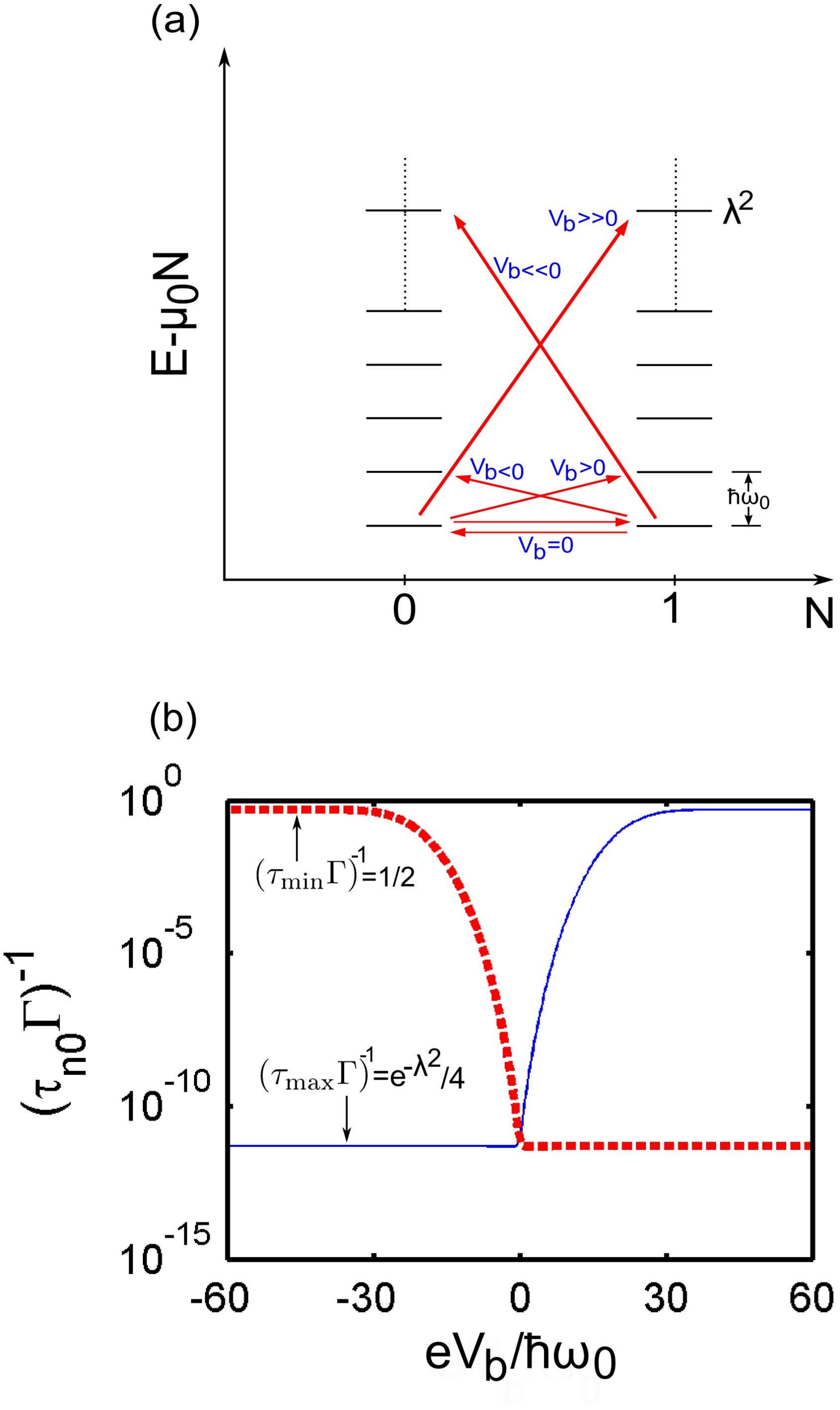

Figure 4.3: (a) Energy-level scheme for the relevant transitions in a coordinate system given by the particle number N and grandcanonical energy $E - \mu_0 N$ at $V_\mathrm{b} = 0$. The red lines represent the transitions threshold, where the thickness of each transition line gives the strength of the transition. The polaron energy levels are aligned with the 0-particle states for our chosen set of parameters ($\mu_0 = 0$, $V_\mathrm{g} = 0$, $\varepsilon_0 = 25\hbar\omega_0$, $\lambda = 5$) yielding the polaron shift $\varepsilon_\mathrm{p} = \varepsilon_0$. (b) Inverse lifetimes $(\tau_{n0}\Gamma)^{-1}$ on logarithmic scale as a function of normalized bias voltage $eV_\mathrm{b}/\hbar\omega_0$. The red thick line represents the inverse lifetime of the 1-particle ground state, while the thin blue line refers to the 0-particle ground state.

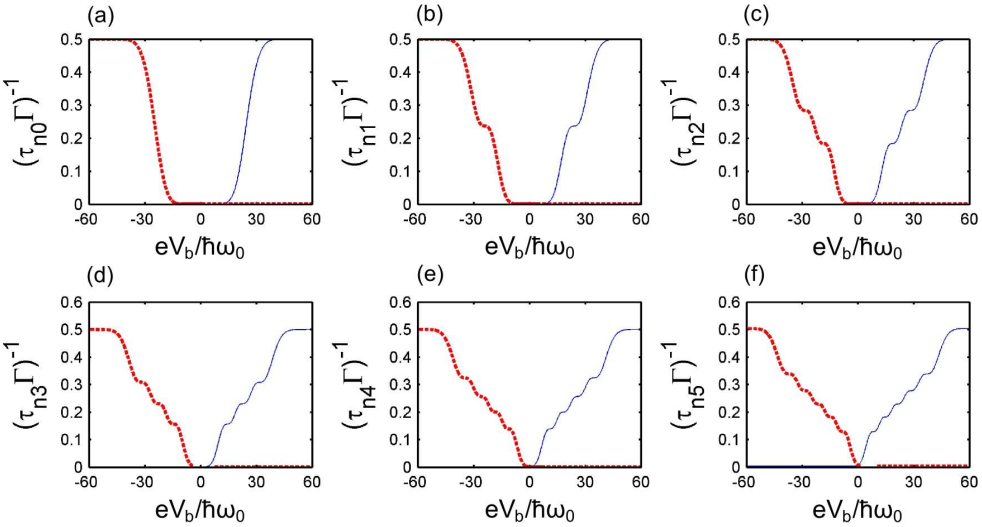

Figure 4.4: Inverse lifetime $(\tau_{nm}\Gamma)^{-1}$ as a function of normalized bias voltage $eV_\mathrm{b}/\hbar\omega_0$ for (a) vibronic ground states, (b) first excited states, (c) second excited states, (d) third excited states, (e) fourth excited states, (f) fifth excited states when $V_\mathrm{g} = 0$. The blue thin line represents the inverse lifetime of the 0-particle state ($n = 0$), while the thick dashed red line refers to the 1-particle state ($n = 1$). The asymmetry parameter is $\eta = 0$ and we fix the zero of the energy at the leads chemical potential at zero bias: $\mu_0 = 0$. The energy of the molecular level is $\varepsilon_0 = 25\hbar\omega_0$. The electron-vibron coupling constant is $\lambda = 5$ yielding a polaron shift $\varepsilon_\mathrm{p} = \varepsilon_0$. Finally, the thermal energy is $k_\mathrm{B}T = 0.2\hbar\omega_0$, the frequency of the driving field is $\omega = 0.002\omega_0$, and $\Gamma_\mathrm{s} = \Gamma_\mathrm{d} = 0.006\omega_0$.

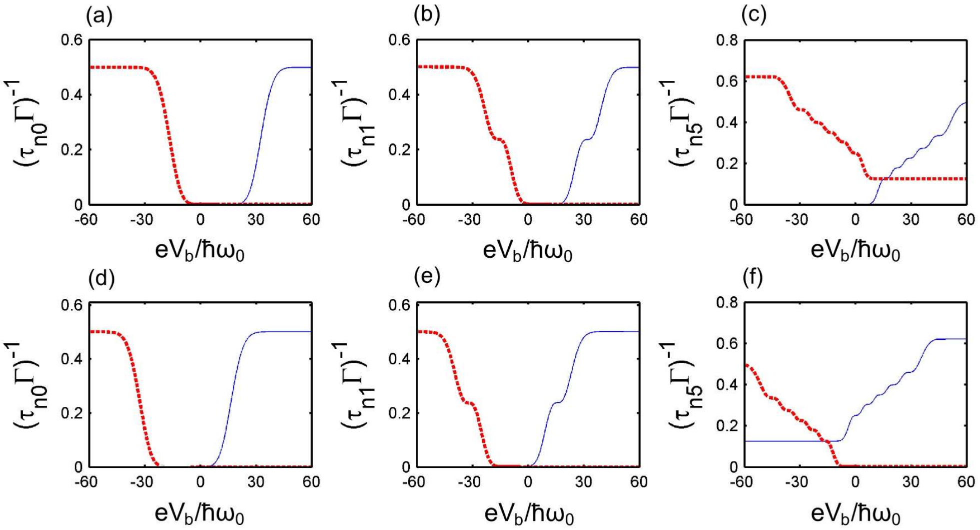

Figure 4.5: Inverse lifetime $(\tau_{nm}\Gamma)^{-1}$ as a function of normalized bias voltage $eV_\mathrm{b}/\hbar\omega_0$ for (a) vibronic ground states, (b) first excited states, (c) fifth excited states when $eV_\mathrm{g}/\hbar\omega_0 = 8$, while (d) shows vibronic ground states, (e) first excited states, and (f) fifth excited states, when $eV_\mathrm{g}/\hbar\omega_0 = -8$. The remaining parameters are the same as used in Fig. 4.4.

Analogously, we can explain the behavior of the lifetimes of the excited states, see Fig. 4.4. It follows that in the considered parameters range, in general, the 0-particle vibronic states are stable at large enough negative bias voltage, while the 1-particle vibronic states are stable at large positive bias. There is, however, an interval of bias voltage, the so-called bistable region, where both states $|1,m'\rangle_1$ and $|0,m\rangle_1$ are stable for not too large m and m', as shown in Fig. 4.4. Moreover, m steps are observed in the inverse lifetimes τ_{nm}^{-1}, see Figs. 4.4(b-f), because for certain values of the coupling constant λ some of the FC factors $F_{mm'}$ vanish or are exponentially small such that the additional channels opened upon increasing the bias voltage do not have pronounced contribution. For instance, the FC factor for the first excited vibronic state can be described as

$$F_{1m'} = e^{-\lambda^2}\frac{\lambda^{2(m'-1)}}{m'!}(m'-\lambda^2)^2, \tag{4.36}$$

which vanishes for $m' = \lambda^2$. That is why a plateau around $eV_\mathrm{b}/\hbar\omega_0 = 25$ in Fig. 4.4(b) is observed for our chosen parameters. Analogously, for the second excited vibronic state, one has the expression for $F_{2m'}$ in the form

$$F_{2m'} = e^{-\lambda^2}\left\{\frac{1}{2}\lambda^6 - \frac{3}{2}\lambda^4 + 2\lambda^2 + \frac{\lambda^{2(m'-2)}}{2!m'!}\left[m'^2 - m'(1+2\lambda^2)+\lambda^4\right]^2\right\}, \tag{4.37}$$

which has two minima at

$$m_1 = \frac{1+2\lambda^2+\sqrt{1+4\lambda^2}}{2},\ m_2 = \frac{1+2\lambda^2-\sqrt{1+4\lambda^2}}{2}. \tag{4.38}$$

Hence, two plateau can be observed, see Fig. 4.4(c), around $eV_\mathrm{b}/\hbar\omega_0 = 20$ and $eV_\mathrm{b}/\hbar\omega_0 = 31$. Similar arguments can be extended to explain the steps in the inverse lifetimes of higher excited states. This also implies that the bias window for bistability shrinks for excited states and even disappears for large enough m. It follows that the major contribution in bistability is coming from low excited vibronic states. Note that the bistability of the many body states is crucial for the hysteresis and hence memory effects which is discussed in the next section. Finally, a closer inspection of Fig. 4.4 reveals that the minimum of the inverse lifetime increases with the vibronic quantum number m. This effect can be understood easily by analyzing the minimum of the inverse lifetime for each particle state. For example the minimum of the inverse lifetime for the 0-particle vibronic ground state is, cf Eq. (4.35), whereas for the 0-particle vibonic first excited state is

$$\tau_{01}^{-1}(V_\mathrm{b}\to-\infty) = \frac{\Gamma_\mathrm{d}}{2}(1+\lambda^4)e^{-\lambda^2}. \tag{4.39}$$

From Eqs. (4.35) and (4.39), one can conclude that $\tau_{00}^{-1}(V_\mathrm{b}\to-\infty) < \tau_{01}^{-1}(V_\mathrm{b}\to-\infty)$. A similar explanation can be extended to the higher excited states. For gate voltages such that $eV_\mathrm{g} > 0$, the 1-particle vibronic excited states are becoming unstable faster than the 0-particle states, see Fig. 4.5(a)-(c), while for large negative gate ($eV_\mathrm{g} < 0$),

the 0-particle states are getting unstable fast, see Fig. 4.5(d)-(f). In order to explain this effect, we analyze the shift of the inverse lifetime of the 0-particle vibronic first excited state, τ_{01}^{-1}, as follows:
The maximum of the inverse lifetime for $V_\mathrm{g} \neq 0$ is

$$\tau_{01}^{-1}(V_\mathrm{b} \to \infty) = \Gamma_\mathrm{s} + \Gamma_\mathrm{d} \sum_m F_{1m} f(eV_\mathrm{g} + \hbar\omega_0(m-1)), \tag{4.40}$$

whereas the minimum is given by

$$\tau_{01}^{-1}(V_\mathrm{b} \to -\infty) = \Gamma_\mathrm{d} \sum_m F_{1m} f(eV_\mathrm{g} + \hbar\omega_0(m-1)). \tag{4.41}$$

Eqs. (4.40) and (4.41) imply that both minimum and maximum of τ_{01}^{-1} shift by an equal amount and the condition of the bistability region can be tuned by setting V_g.

4.4 Quantum switching and hysteresis

Neutral and charged (polaron) states correspond to different potential energy surfaces and transitions between low-lying vibronic states are strongly suppressed in the presence of strong electron-vibron interaction. This leads to the bistability of the system. Upon applying an external voltage, one can change the state of this bistable system obtaining under specific conditions hysteretic charge-voltage and current-voltage curves. Here it is crucial to point out that only if the time scale of variation of the external perturbation is shorter than the maximum lifetime but longer than the minimum lifetime of the system hysteresis can be observed, i.e., $\tau_\mathrm{min} \sim \tau_\mathrm{switch} < T_\mathrm{ex} < \tau_\mathrm{max}$. Due to $\tau_\mathrm{max} > T_\mathrm{ex}$, the system stays in the stable state during the sweeping until the sign of the perturbation changes, the former stable state becomes unstable and, due to $T_\mathrm{ex} < \tau_\mathrm{min}$, a switching to the new stable state can occur. In this section we now consider the situation when $\omega \sim \Gamma$, i.e., $T_\mathrm{ex} \sim \tau_\mathrm{switch}$ while in Sec. 4.5 the regime $\omega \ll \Gamma$, i.e., $T_\mathrm{ex} \gg \tau_\mathrm{switch}$ is addressed. In Figs. 4.6 and 4.7 we present the populations of the electronic states, $P_n = \sum_m P_n^m$, as well as of the vibronic states, $P^m = \sum_n P_n^m$, respectively. Specifically, in Fig. 4.6(a)-(b), we have plotted the populations of the 0- and 1-particle electronic states as a function of normalized bias voltage, where hysteresis loops can be seen. In Fig. 4.6(c), instead, we have shown the population of the 0-particle electronic state as a function of time. The latter can be used to determine the time τ_switch of switching between the neutral and charged states. In a similar way, the sweeping time T_ex of the bias voltage can be calculated using Fig. 4.6(d). By comparison of these two time scales, it is apparent that the switching time is of the same order as the sweeping time and much shorter than the lifetime in the bistable region, see Fig. 4.3. The relation $\tau_\mathrm{switch} \approx T_\mathrm{ex}$ also explains why the switching between the neutral and charged state is on average never complete (P_0 oscillates between 0.2 and 0.8). In Fig. 4.7, the populations of the vibronic states as a function of the normalized bias voltage are shown, while in Fig. 4.8 the populations of the different vibronic states resolved for different charges have been plotted. Clearly not only the vibronic ground

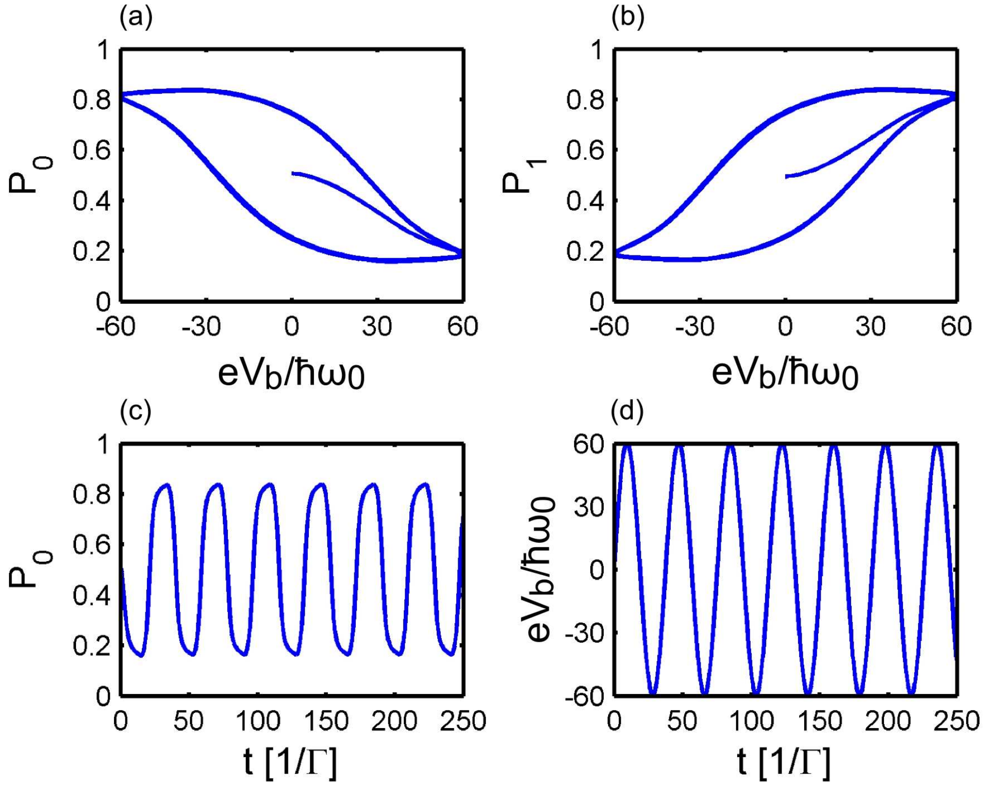

Figure 4.6: (a)-(b) Occupation probabilities P_0 and P_1 of the 0- and 1-particle electronic states as a function of normalized time dependent bias voltage $eV_\mathrm{b}/\hbar\omega_0$, (c) population of the 0-particle configuration as a function of time; (d) normalized bias voltage as a function of time. The parameters are the same as used in Fig. 4.4.

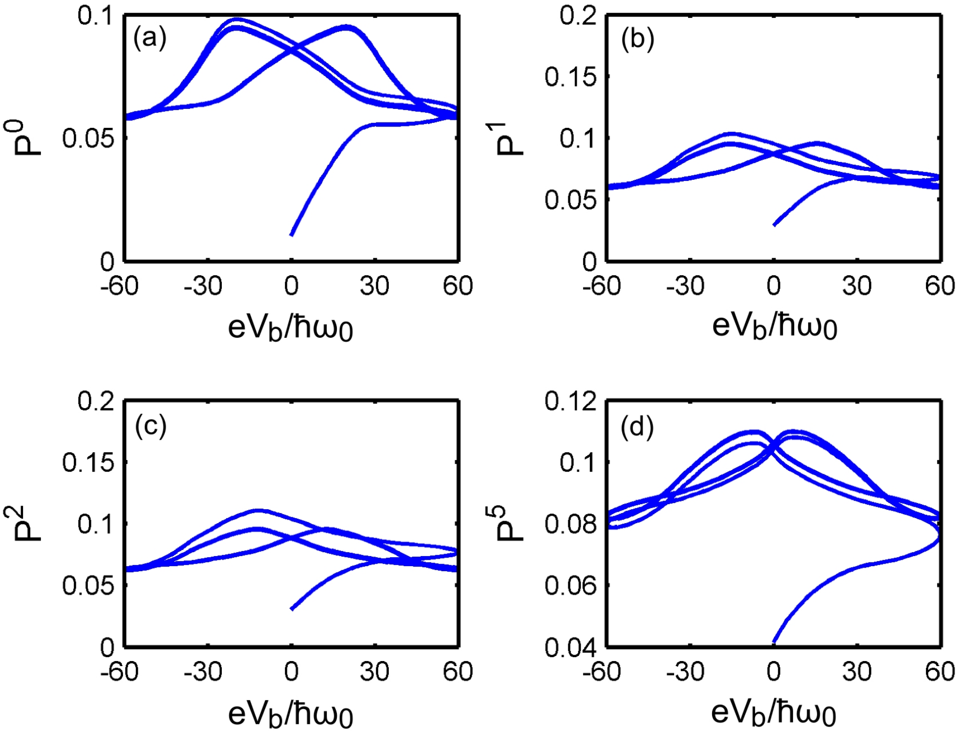

Figure 4.7: Populations P^m of the vibronic states as a function of normalized time dependent bias voltage $eV_\mathrm{b}/\hbar\omega_0$ for (a) ground state, (b) first excited state, (c) second excited state, and (d) fifth excited state. The parameters are the same as used in Fig. 4.4.

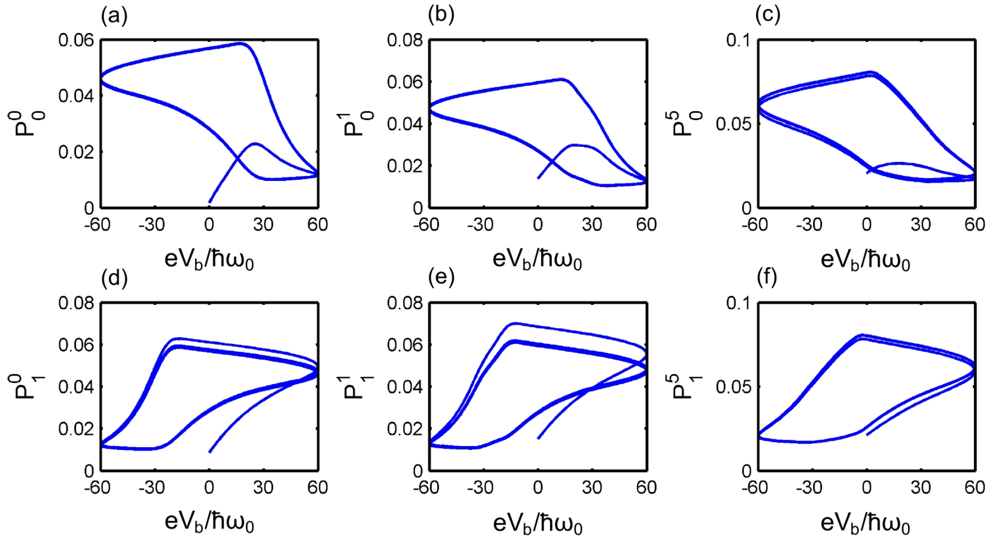

Figure 4.8: Plots of the population P_n^m as a function of normalized time dependent voltage $eV_\mathrm{b}/\hbar\omega_0$ for the 0-particle vibronic (a) ground state, (b) first excited state, (c) fifth excited state, and for the 1-particle vibronic (d) ground state, (e) first excited state, (f) fifth excited state. The parameters are the same as used in Fig. 4.4.

states (which were considered in Ref. [102]) show hysteretic behavior but the vibronic excited states also exhibit these interesting features. Furthermore, inspection of these figures reveals that even after relaxation on the stable limit cycle, the vibronic excited states are highly populated in the non-stationary case in contrast to the stationary case $\omega \to 0$, see e.g., Figs. 4.17 and 4.19, where the population of the excited states is strongly suppressed. Hence it is natural to take into account the vibronic excited states in the dynamics of the system.

4.4.1 Memory effects in the current-voltage characteristics

The hysteretic behavior of the bistable system is also reflected in the current as a function of normalized bias, see Fig. 4.9, where a hysteresis loop (single loop) is observed in the current calculated both at the left and the right lead. Interestingly, the left and the right currents differ by more than a sign, in contrast to the stationary case. This behavior is understandable again in terms of relaxation time scales. In fact, for voltages $|V_b|$ outside the bistable region the system relaxes to the stationary regime on a time scale τ_switch. Though, since the driving time T_ex has the same order of magnitude, the stationary regime cannot be reached. Yet, no net charge accumulation occurs since $I_{L,\mathrm{av}} = -I_{R,\mathrm{av}}$. In Fig. 4.10, we plot the left time dependent current as a function of the normalized bias for different values of the electron-vibron coupling constant. An inspection of this figure reveals that the width of the hysteresis loop decreases and shifts from zero bias upon decreasing the coupling constant λ. This feature can be understood by observing that for $\lambda \neq 5$ the polaron shift ε_p does not longer compensate the energy of the molecular level ε_0, and hence the polaron energy $\varepsilon \neq 0$. In other words, the system is no longer behaving symmetrically upon exchange of the sign of

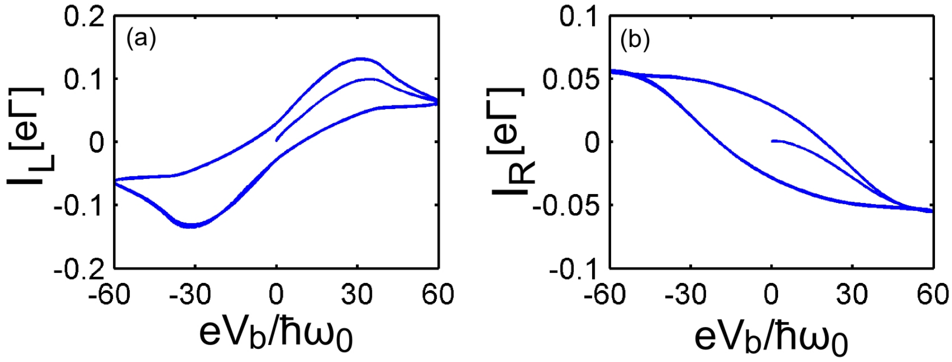

Figure 4.9: Time dependent current as a function of normalized voltage for (a) left lead, (b) right lead. The parameters are the same as used in Fig. 4.4.

the bias voltage. If we consider e.g. the case $\lambda = 1$ is, for $V_\mathrm{g} = \mu_0 = 0$, $\varepsilon/\hbar\omega_0 = 24$. In turn this implies that $\tau_{00}^{-1}(V_\mathrm{b} = 0) \sim 0$ and $\tau_{10}^{-1}(V_\mathrm{b} = 0) \sim \Gamma_\mathrm{s} + \Gamma_\mathrm{d}$, i.e., the region around zero bias is no longer bistable as for the case $\lambda = 5$. Hence the dot is preferably empty at zero bias. Switching however can be reached upon increasing V_b in the region around $eV_\mathrm{b} \sim \varepsilon$. Overall however the bistability region has shrunk. Similar considerations apply to the other considered values of λ.

4.4.2 Role of vibron energy in memory attributes

In this section, we illustrate the role played by the vibronic energy in the hysteretic behavior of the system. The vibron energy of the whole system can be expressed as

$$E_\mathrm{v} = \mathrm{Tr}_\mathrm{sys}\left\{\hat{\rho}_\mathrm{red}\hbar\omega_0\left(\hat{a}^\dagger\hat{a} + \frac{1}{2}\right)\right\}, \tag{4.42}$$

where the trace is taken over the system degrees of freedom. The normalized vibronic energy as a function of normalized bias voltage is depicted in Fig. 4.11(a), where hysteretic loops are also observed. The value of the vibronic energy, together with the observation that the probability distribution is relatively flat over the excitations, see Fig. 4.8, ensures that, depending on the bias, between 10 and 20 vibronic excited states are considerably populated. Further insight in the dynamics of the system is obtained by considering the correlation between the vibronic energy and the charge occupation. The vibron energy associated with the 0-particle state is determined by the relation

$$E_{\mathrm{v},0} = \mathrm{Tr}_\mathrm{sys}\left\{\hat{\rho}_0\hbar\omega_0\left(\hat{a}^\dagger\hat{a} + \frac{1}{2}\right)\right\}, \tag{4.43}$$

with $\hat{\rho}_0 = \hat{\rho}_\mathrm{red}|0,m\rangle_{11}\langle 0,m|$. In Fig. 4.11(b), the normalized vibronic energy as a function of normalized bias voltage for the 0-particle configuration has been plotted. The hysteresis loop resembles that of Fig. 4.6(a) implying a direct correlation between the vibronic energy and the population of the neutral state i.e., the more the neutral state is occupied the higher is the associated vibronic energy. Qualitatively the result

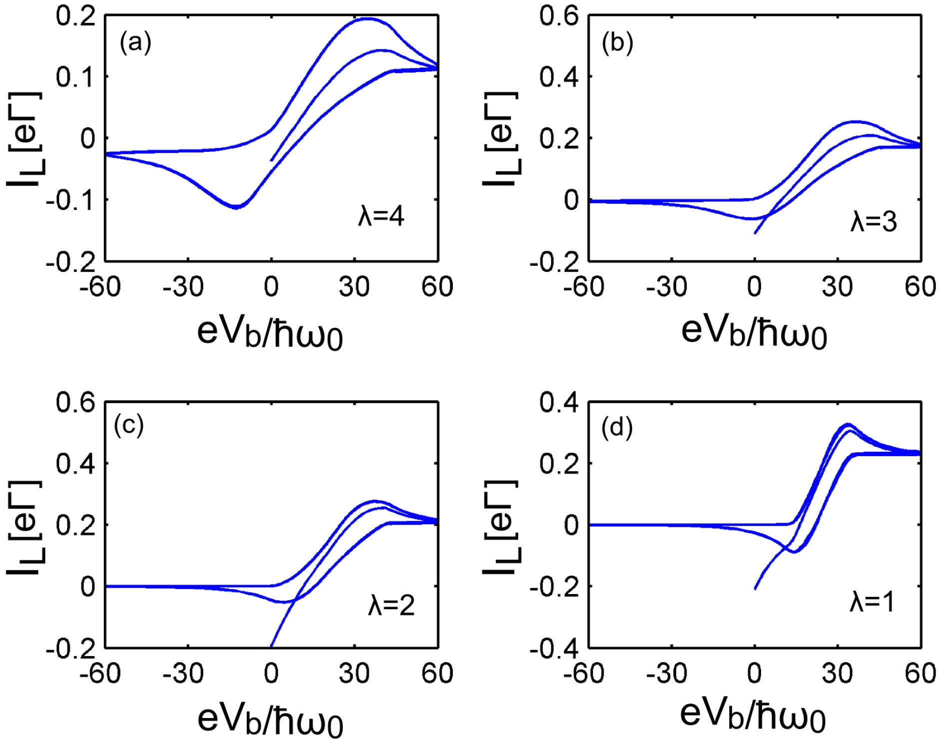

Figure 4.10: Time dependent current for left lead as a function of the normalized voltage for coupling constants (a) $\lambda = 4$, (b) $\lambda = 3$, (c) $\lambda = 2$, and (d) $\lambda = 1$. The remaining parameters are the same as used in Fig. 4.4.

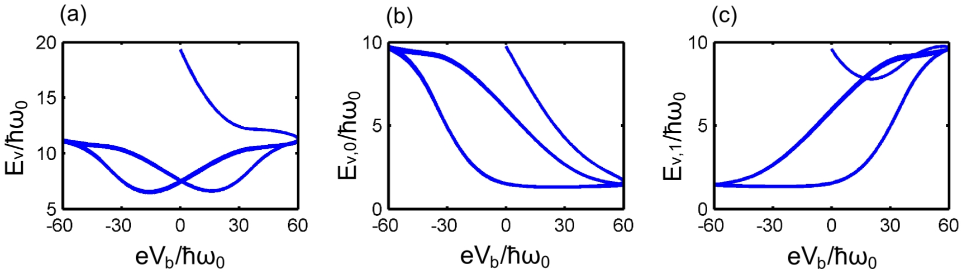

Figure 4.11: (a) Total vibron energy as a function of the time dependent bias voltage. (b) Vibron energy for the 0-particle, and (c) for the 1-particle configuration only. Parameters are the same as used in Fig. 4.4.

can be explained as follows: transitions from the charged to the neutral states are predominantly involving low energy charged states and highly excited neutral states. Due to energy conservation and asymmetric bias drop these transitions are confined to the large negative biases where the highly excited neutral states show also a long life time. This situation remains roughly unchanged during the up sweep of the bias until the symmetric condition is obtained at high positive bias and the charged excited states are maximally populated. Finally, the bistability around zero bias explains the hysteresis. The analytical expression for the vibronic energy of the 1-particle state is given by

$$E_{\mathrm{v},1} = \mathrm{Tr}_{\mathrm{sys}} \left\{ \hat{\rho}_1 \hbar\omega_0 \left(\hat{a}^\dagger \hat{a} + \frac{1}{2} \right) \right\}, \tag{4.44}$$

with $\hat{\rho}_1 = \hat{\rho}_{\mathrm{red}} |1, m\rangle_{11} \langle 1, m|$. The normalized average vibron energy as a function of normalized bias voltage for the 1-particle configuration is sketched in Fig. 4.11(c), where we can observe a hysteresis loop resembling that of Fig. 4.6(b). In conclusion, the vibron energies also show hysteretic behavior, in analogy to the population-voltage and current-voltage curves, in the non-stationary limit.

4.5 Testing lower driving frequencies

When lowering the driving frequency ω ($\omega \ll \Gamma$) of the external perturbation, we choose $\omega = 2 \times 10^{-6}\omega_0$, our model displays features similar to those presented in Ref. [102]. In more detail, we show the population of the electronic states as a function of normalized bias and time in Fig. 4.12(a)-(b), Fig. 4.12(c), respectively, whereas in Fig. 4.12(d) the normalized bias as a function of time is shown. In this case the population-voltage curve is slightly different from Fig. 4.6 because the transition between 0 and 1 occurs more abruptly as a function of V_b and it is complete. Indeed, for the parameter chosen in Fig. 4.12 is $\varepsilon = 0$ and $\tau_{\mathrm{max}}^{-1} \sim \omega_{\mathrm{min}} \ll \omega \ll \Gamma \sim \tau_{\mathrm{switch}}^{-1}$. In other words the frequency is small compared to the charge/discharge rate. The system thus follows adiabatically the changes of the bias voltage and only switches at those values of the bias where $\tau_{n0} \sim \tau_{\mathrm{switch}}$. The time-dependent left current as a function of normalized bias is shown in Fig. 4.13(a) giving two loops, one for positive bias sweeping

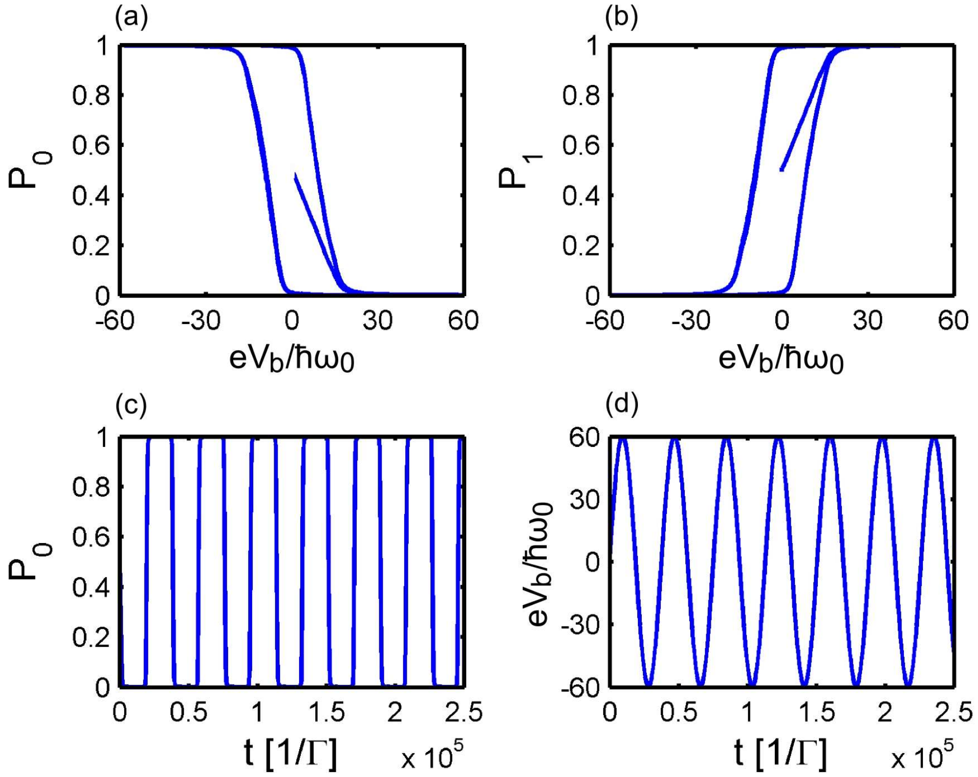

Figure 4.12: (a)-(b) Population of the 0- and 1-particle electronic states as a function of the bias voltage, (c) population of the 0-particle electronic state as a function of time, and (d) normalized bias voltage as a function of time. The frequency of the driving field is $\omega = 2 \times 10^{-6}\omega_0$. The other parameters are the same as used in Fig. 4.4.

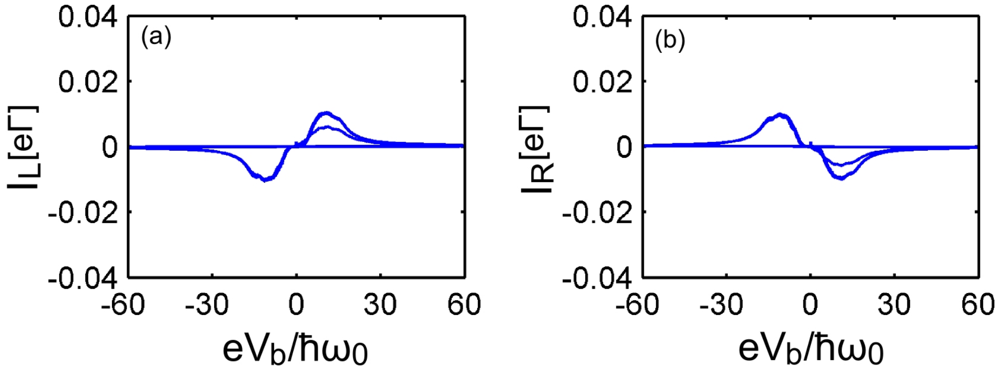

Figure 4.13: Plot of the time dependent current as a function of normalized voltage for (a) left lead, (b) right lead. The value of gate voltage is $V_\mathrm{g} = 0$ and the frequency of the driving field is $\omega = 2 \times 10^{-6}\omega_0$. The other parameters are the same as used in Fig. 4.4.

and the other for negative sweeping. The right current is shown in Fig. 4.13(b). Due to the extremely low frequency the currents substantially fulfill the quasi-stationary relation $I_L(t) = -I_R(t)$ associated to a fully adiabatic regime. In Fig. 4.14, we present the populations of the vibronic states and hysteretic loops are visible. Vibronic states with quantum numbers up to λ all display nonvanishing populations, much less than in the case $T_\mathrm{ex} \approx \tau_\mathrm{switch}$.

4.6 The DC-case ($\omega \to 0$)

In this section, we consider the limit ($\omega \to 0$) of DC-bias as a special case of the master equation presented in the previous section and compare the results. Even if the system still exhibits the bistable properties discussed in Sec. 4.3 (they are in fact not related to the sweeping time of the bias) the hysteretic behavior cannot be observed anymore. In Fig. 4.15, we present the population of the electronic states for gate voltage $V_\mathrm{g} = 0$. At large negative bias the system is empty, while at large positive bias it is charged. The system makes transitions from the 0- to 1-particle state near zero bias. Analogously, in Fig. 4.16, the population of electronic states as a function of normalized bias is depicted for gate voltage $eV_\mathrm{g}/\hbar\omega_0 = 8$. Due to a finite ε, the transition $0 \to 1$ occurs at positive bias voltages. Moreover, the populations of the vibronic states are sketched in Fig. 4.17 for gate voltage $V_\mathrm{g} = 0$, which clearly shows that, for the considered parameters, only the vibronic ground state and first excited state are populated, whereas the populations of higher excited states are very small. This is in contrast to the non-stationary case where the excited states are highly populated, see Fig. 4.7. In a similar way, the populations of the vibronic states for gate voltage $eV_\mathrm{g}/\hbar\omega_0 = 8$ are presented in figure 4.18 where higher excited states also get populated. Finally, in Figs. 4.19 and 4.20 we show the populations of the 0- and 1-particle vibronic states for gate voltages $V_\mathrm{g} = 0$ and $eV_\mathrm{g}/\hbar\omega_0 = 8$, respectively, which basically provide the same information as mentioned before.

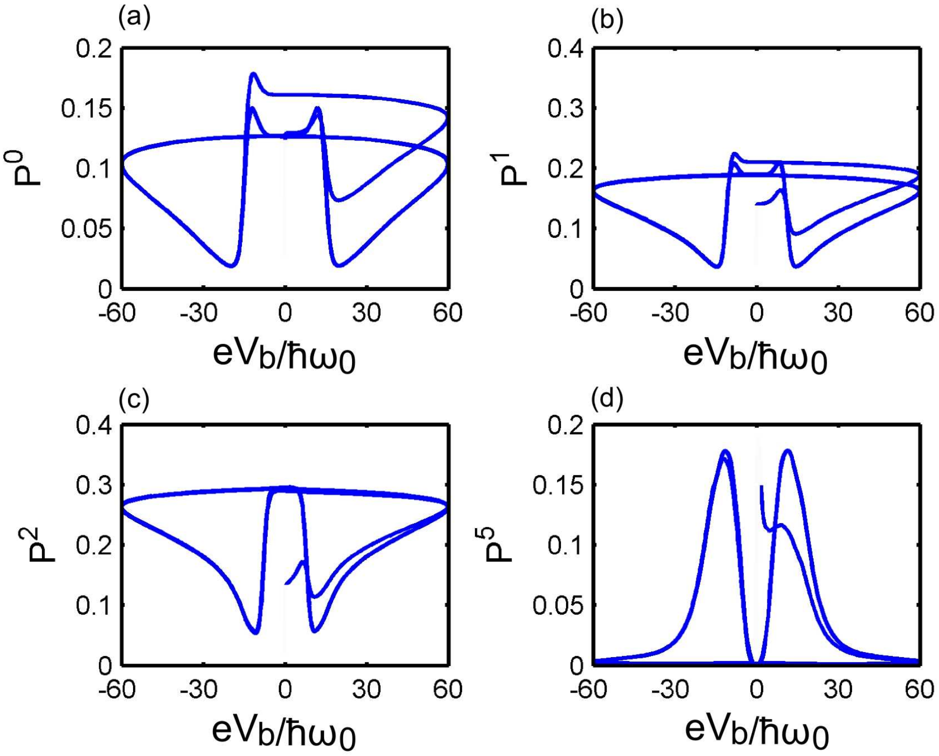

Figure 4.14: Plots of populations of vibronic (a) ground state, (b) first excited state, (c) second excited state, and (d) fifth excited state. The frequency of the driving field is $\omega = 2 \times 10^{-6}\omega_0$. The other parameters are the same as used in Fig. 4.4.

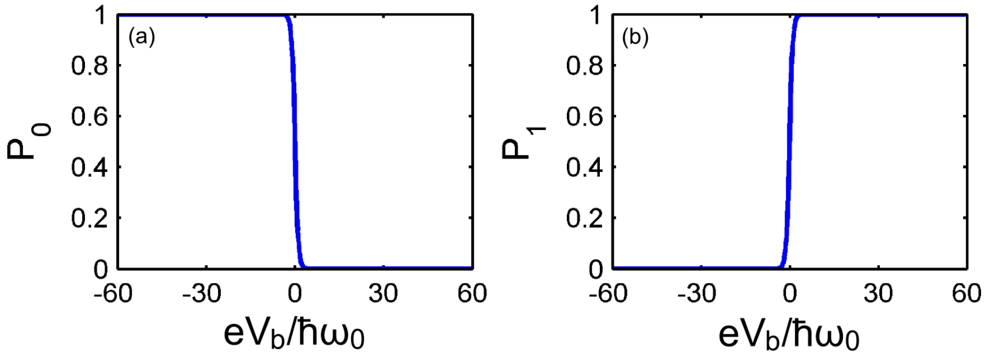

Figure 4.15: Population of (a) the 0-particle electronic state, (b) the 1-particle electronic state. The value of gate voltage is $V_\mathrm{g} = 0$, and the frequency of the driving field is $\omega \ll 1/\tau_\mathrm{max}$. The other parameters are the same as used in Fig. 4.4.

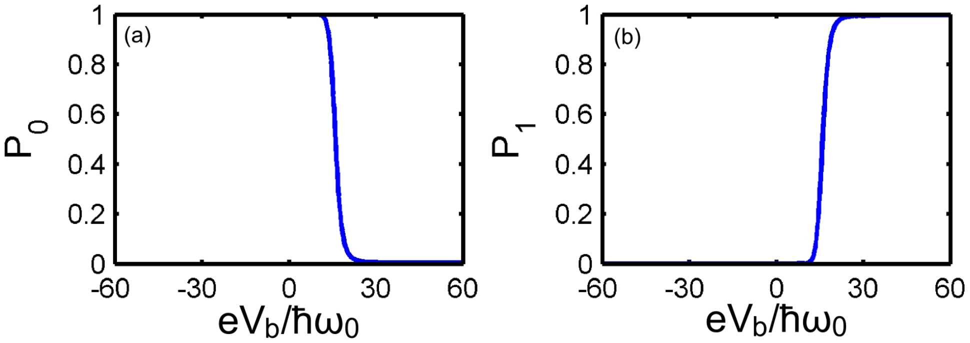

Figure 4.16: (a) Population of the 0-particle electronic state, (b) population of the 1-particle electronic state. The value of the gate voltage is $eV_\mathrm{g}/\hbar\omega_0 = 8$, and the frequency of the driving field is $\omega \ll 1/\tau_\mathrm{max}$. The other parameters are the same as used in Fig. 4.4.

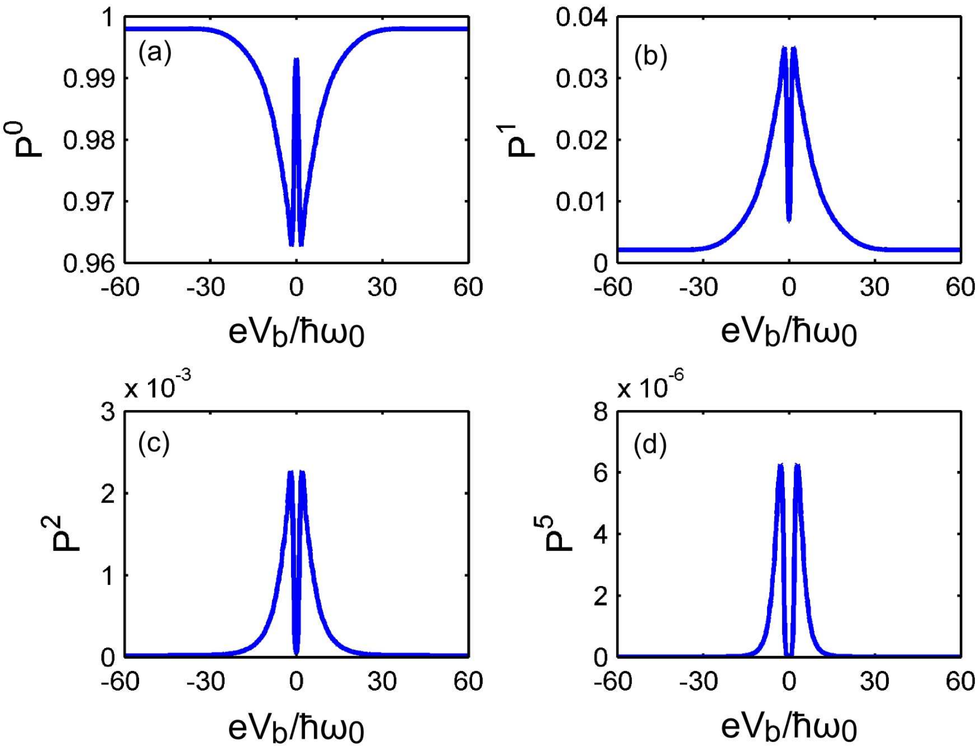

Figure 4.17: Populations as a function of normalized bias voltage for (a) vibronic ground state, (b) first excited state, (c) second excited state, and (d) fifth excited state. The frequency of the driving field is $\omega \ll 1/\tau_\mathrm{max}$. The other parameters are the same as used in Fig. 4.4.

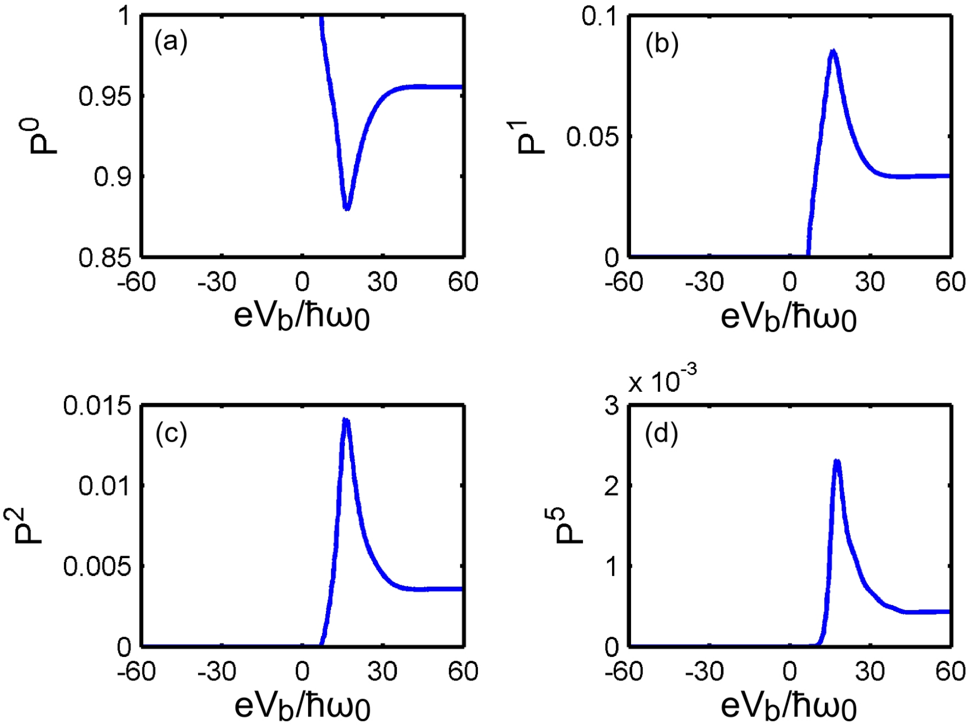

Figure 4.18: Population as a function of normalized bias voltage for (a) vibronic ground state, (b) first excited state, (c) second excited state, and (d) fifth excited state. The value of the gate voltage is $eV_g/\hbar\omega_0 = 8$, and the frequency of the driving field is $\omega \ll 1/\tau_{\max}$. The other parameters are the same as used in Fig. 4.4.

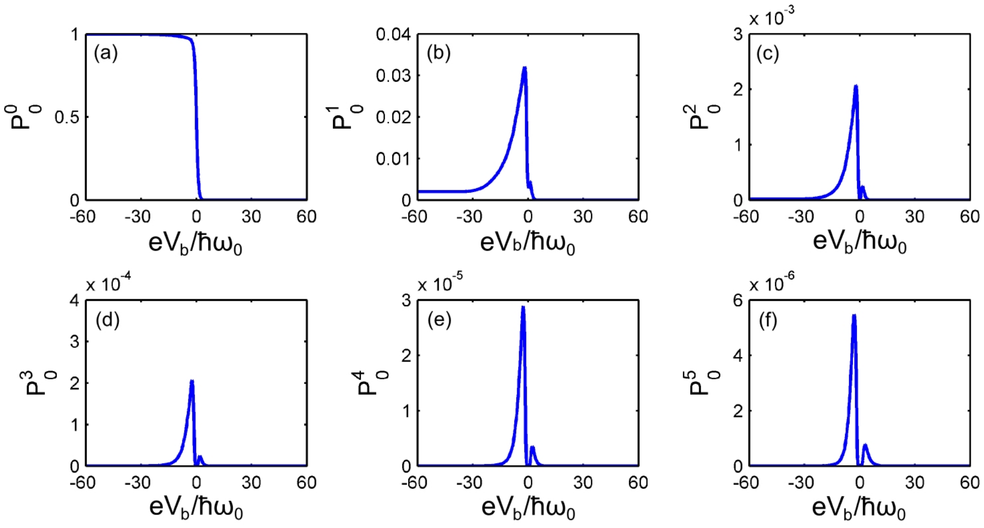

Figure 4.19: Populations P_0^m as a function of normalized bias voltage for the 0-particle (a) vibronic ground state, (b) first excited state, (c) second excited state, (d) third excited state, (e) fourth excited state, (f) fifth excited state, (g) sixth excited state, (h) seventh excited state, and (i) eighth excited state. The frequency of the driving field is $\omega \ll 1/\tau_{\max}$. The other parameters are the same as used in Fig. 4.4.

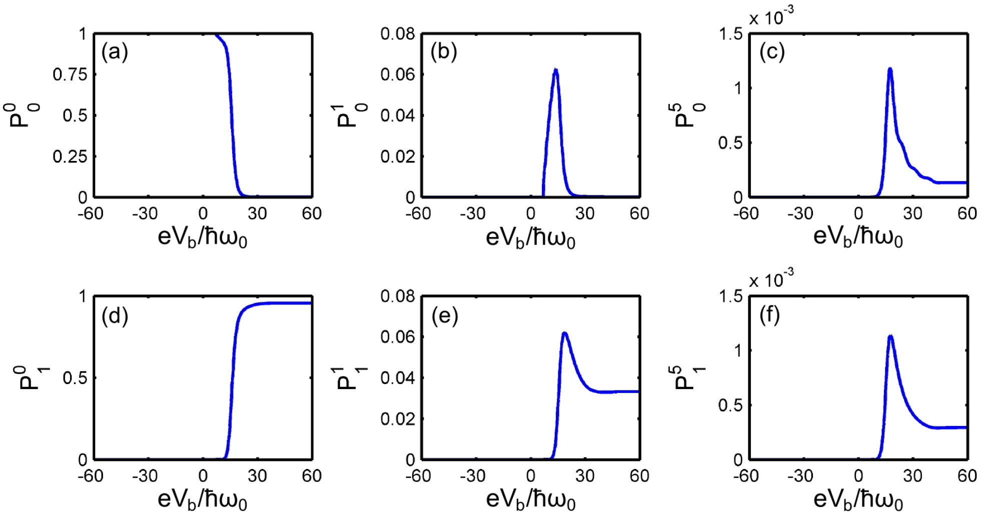

Figure 4.20: Population as a function of normalized bias voltage for the 0-particle (a) vibronic ground state, (b) first excited state, (c) fifth excited state and (d) 1-particle ground state, (e) first excited state, (f) fifth excited state. The value of the gate voltage is $eV_\mathrm{g}/\hbar\omega_0 = 8$, and the frequency of the driving field is $\omega \ll 1/\tau_\mathrm{max}$. The other parameters are the same as used in Fig. 4.4.

4.6.1 Current-voltage characteristics for the DC-case

In the DC-case the analytical expression for the current remains the same as given by Eq. (4.26) taking into account a time independent bias. Let us first discuss the situation when the 0- and 1-particle states are in resonance, $\varepsilon = \varepsilon_0 - \varepsilon_\mathrm{p} = 0$ and $V_\mathrm{g} = 0$. In this particular case, an interesting behavior of the I-V characteristics with two opposite current peaks around zero bias can be observed, see Fig. 4.21. In order to understand the mechanism of this process, we consider the source current which can be expressed in the form

$$I_\mathrm{s} = \Gamma_\mathrm{s} \sum_{mm'} F_{mm'} \big\{ f^+ \big[\varepsilon + \hbar\omega_0 (m' - m) - eV_b\big] P_0^m \\ - f^- \big[\varepsilon + \hbar\omega_0 (m' - m) - eV_b\big] P_1^{m'} \big\}. \tag{4.45}$$

At $V_b = 0$ only ground to ground state transitions are open and $P_0^0 = P_1^0 = \frac{1}{2}$. Hence in this region the current is zero. At large positive bias, i.e., $V_b \to \infty$, the current is zero because the system is in a 1-particle stable state and no new transition channel is available. For finite bias, the behavior of the Franck-Condon factor $F_{mm'}$ is of importance. In particular, it suffices to investigate the classically allowed transitions as determined by the Franck-Condon parabola [17,61]. The minimum of the parabola is for $m = m' \sim \left(\frac{\lambda}{2}\right)^2$, i.e., $m, m' < \left(\frac{\lambda}{2}\right)^2$ transitions are exponentially suppressed. Moreover, $F_{mm'}$ attains the maximal values for $F_{mm'} = F_{m0}$ or $F_{mm'} = F_{0m'}$ and m or m' of the order of λ^2. Hence Fig. 4.19 describes a threshold effect. The populations P_1^m of the 1-particle states are mirror symmetric with respect to the bias inversion (not shown). Analogously, we can analyze in the same way as above the current peak in Fig. 4.22 which occurs at $eV_\mathrm{b} \sim \varepsilon$ for gate voltage $eV_\mathrm{g}/\hbar\omega_0 = 8$.

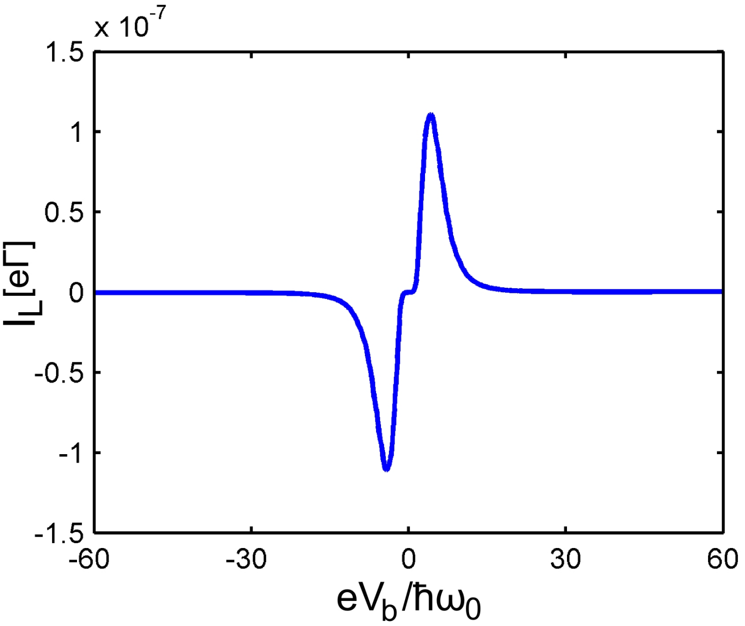

Figure 4.21: Current as a function of normalized bias. The frequency of the driving field is $\omega \ll 1/\tau_{\text{max}}$. The other parameters are the same as used in Fig. 4.4.

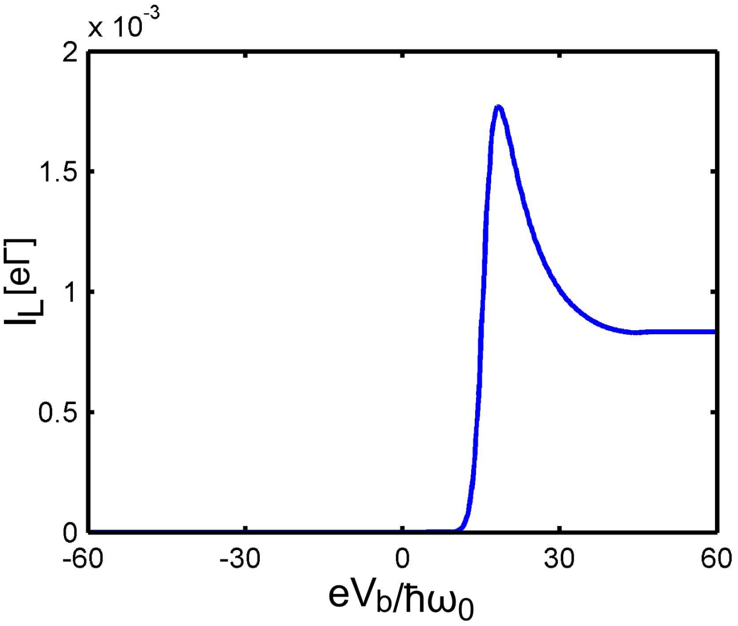

Figure 4.22: Current as a function of normalized bias. The value of gate voltage is, $eV_{\text{g}}/\hbar\omega_0 = 8$. The other parameters are the same as used in Fig. 4.4.

The results presented in this chapter were worked out in collaboration with Andrea Donarini, and Milena Grifoni. They have been submitted to the European Physical Journal B.
[105] Andrea Donarini, Abdullah Yar, and Milena Grifoni, aXiv:cond-mat/1205.4927v1 (2012).

Part III

Vibrational modes, spectrum, and Franck-Condon factors of suspended SWCNTs

Chapter 5

Electronic band structure of SWCNTs

Carbon nanotubes are an interesting realization of one-dimensional (1D) electronic system due to their remarkable electrical and mechanical properties inherited from the unusual band structure of a graphene sheet [106]. A short time after their discovery by Iijima [107], carbon nanotubes became an attractive research field with promising perspectives for applications and fundamental science. Suspended single-wall carbon nanotubes (SWCNTs) provide ideal building blocks for NEMS (main focus of this thesis), due to a low mass, easy scalablility through their length, and a large Young's modulus of rigidity, typically 1.25 TPa, which is almost an order of magnitude higher than that of silicon [106]. In this chapter, the physics of noninteracting electrons in single-wall carbon nanotubes (SWCNTs) is shortly reviewed in order to get the basic knowledge of these systems. The results and main concepts will be used in the next chapter where we will take into account the electron-electron and electron-vibron interactions. In order to understand the electronic properties of SWCNTs, it is more convenient to study first the band structure of graphene. The band structure of SWCNTs can be readily obtained from that of a graphene sheet by rolling it using a zone folding technique. It turns out that different types of SWCNTs, e.g., metallic or semiconductor, can be obtained depending on their diameters and helical configuration.

5.1 Electronic band structure of graphene

Graphene is made out of carbon which belongs to the fourth group of periodic table of elements having four valence electrons in the outermost shell that are responsible for the chemical bonding. The electronic structure of an isolated carbon atom is $1s^2 2s^2 2p^2$. In carbon based materials, new orbitals are constructed by a linear combination of different atomic orbital wave functions in order to minimize the bonding energy. The inner two $1s$ electrons remain chemically inert. However, the $2s$ and $2p$ electrons can hybridize leading to the formation of different structures. One possible configuration is the sp^3 hybridization building four similar orbitals, which naturally tend to establish a tetrahedral bonding structure that accommodates all the valence electrons. The example is a well known solid form of carbon, diamond, which is a good insulator with band gap ∼5 eV because all the four electrons participate in the chemical bonding and no free charge carriers are left for conduction. Another possible structure is sp^2 hybridization which leads to the formation of three sp^2-orbitals, leaving one p-orbital unaffected. In this situation, all the three sp^2-orbitals are arranged in a plane at 120^o angles, and the lattice thus formed is the hexagonal lattice. In this case, the hybridization of the $2s$-orbital with the $2p_x$- and $2p_y$-orbitals results in the formation of strong σ-bonds in the lattice plane, whereas the electrons in the remaining $2p_z$-orbitals, oriented perpendicular to the xy-plane with rotational symmetry around the z-axis, form π-bands which essentially determine the electronic properties of graphene at low energies. The structure of the π-band is such that the valence (π-bonding) and conduction (π^*-antibonding) bands touch each other at the corner points of the first Brillouin zone, also known as Dirac points, see Fig. 5.2. Since there is only one p_z-electron per carbon atom, in isolated graphene the valence band is completely filled, whereas the conduction band is empty. That is why graphene is known as a semimetal or zero-gap semiconductor with a vanishing gap. In the vicinity of the Dirac points, the band structure shows a linear dispersion behavior, see the zoomed in region in Fig. 5.2, reminiscent of the one of massless relativistic particles. In this thesis, we focus on the region of linear dispersion which extends far above room temperature (beyond 1 meV). Using a nearest neighbor tight binding calculation technique, one can describe the p_z-electrons in terms of Dirac equation which provides all the required information on the π-band in the vicinity of the Dirac points [108, 109]. It is important to point out that there are two inequivalent sublattices A and B in the graphene sheet, see Fig. 5.1, with the neighborhoods of the corresponding atoms being mirror images of one another. It means that the Bravais lattice of graphene is not the hexagonal lattice itself but it is a triangular lattice with two atoms per unit cell so that we can characterize two different sublattices A and B in the structure. In order to determine the band structure of graphene, it is convenient to choose a Bravais lattice with primitive lattice vectors $\vec{a}_1$ and $\vec{a}_2$, see Fig. 5.1, given by

$$\vec{a}_1 = \frac{\sqrt{3}a_0}{2}\left(1, \sqrt{3}\right), \quad \vec{a}_2 = \frac{\sqrt{3}a_0}{2}\left(-1, \sqrt{3}\right), \tag{5.1}$$

where a_0 denotes the nearest-neighbor C-C bond length. Its value for graphene is 0.142 nm. The two carbon atoms in the unit cell are shifted with respect to the real lattice nodes by

$$\vec{\tau}_+ = \frac{\sqrt{3}a_0}{2}\left(1, \frac{1}{\sqrt{3}}\right), \ \vec{\tau}_- = \frac{\sqrt{3}a_0}{2}\left(1, -\frac{1}{\sqrt{3}}\right). \tag{5.2}$$

The reciprocal lattice vectors $\vec{b}_1$ and $\vec{b}_2$ defined by the condition $\vec{a}_i \cdot \vec{b}_j = 2\pi\delta_{ij}$ are given by

$$\vec{b}_1 = \frac{2\pi}{3a_0}\left(\sqrt{3}, 1\right), \ \vec{b}_2 = \frac{2\pi}{3a_0}\left(-\sqrt{3}, 1\right). \tag{5.3}$$

The first Brillouin zone of the reciprocal lattice is the region bounded by the planes bisecting the vectors to the nearest reciprocal lattice points. In graphene the first

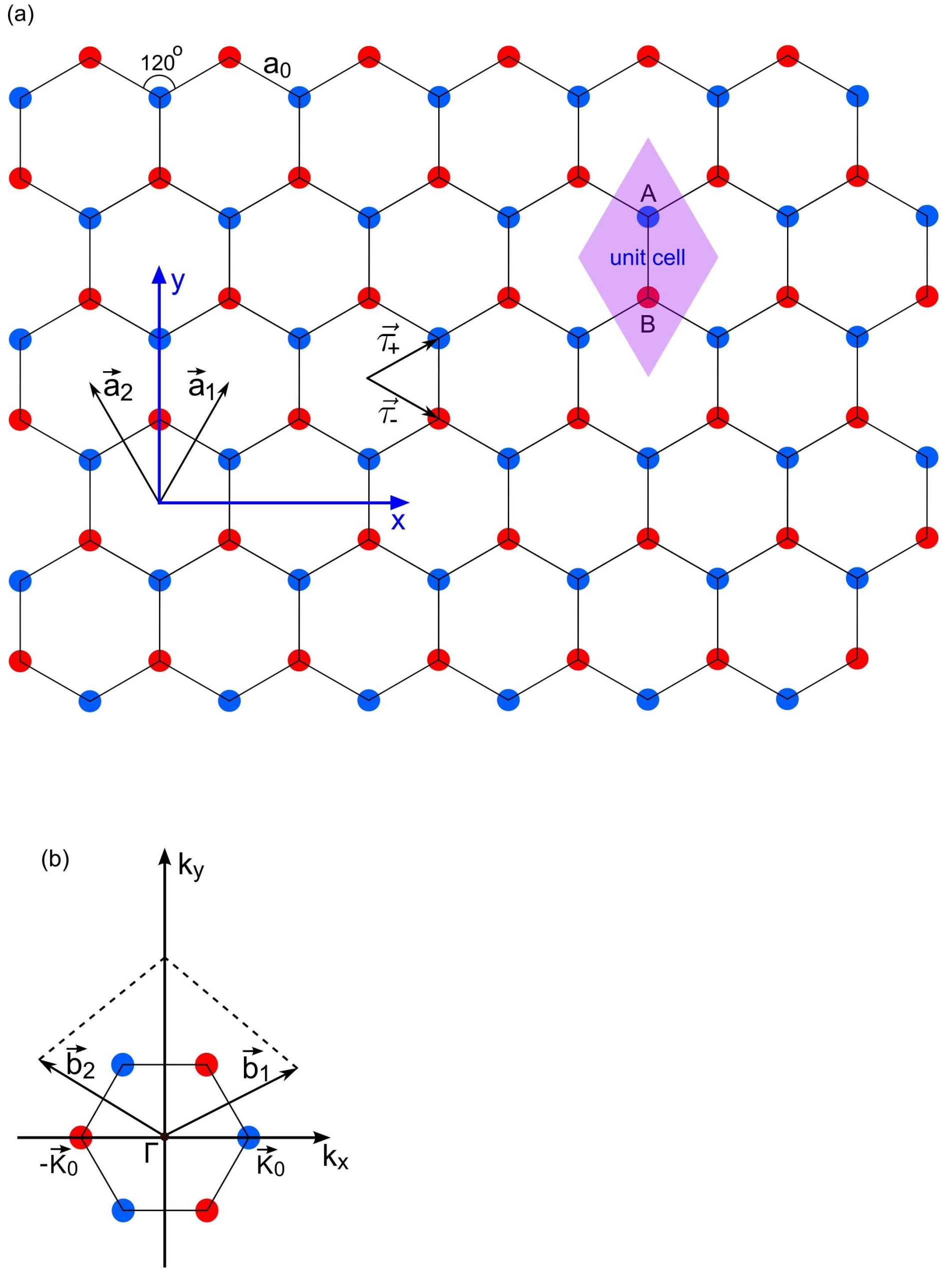

Figure 5.1: (a) Schematic representation of the honeycomb lattice structure of 2D graphene consisting of two interpenetrating triangular lattices. Two primitive lattice vectors are denoted by $\vec{a}_1$ and $\vec{a}_2$. A rhombic unit cell in real space containing two carbon atoms labeled as A and B is shown. The two carbon atoms in the unit cell are specified by $\vec{\tau}_p,\ p = \pm$. The coordinate system in the position space is defined by the xy-axes as shown. (b) The first hexagonal Brillouin zone of the 2D graphene with the coordinate system in momentum space. The Dirac cones are located at the Fermi points. The reciprocal lattice vectors denoted by $\vec{b}_1$ and $\vec{b}_2$ are given.

Brillouin zone (FBZ) is a hexagon resembling the original hexagons of the honeycomb lattice, but rotated by $\pi/2$ as depicted in Fig. 5.1(b). In addition, the six points at the corners of the FBZ are reduced to two groups, each containing three points equivalent under the lattice symmetry operations. We need therefore to consider only the two inequivalent corners, labeled as $\vec{K}_0$ and $-\vec{K}_0$ which are not connected by a reciprocal lattice vector, as shown in Fig. 5.2. These two points at the corners of the graphene Brillouin zone (BZ) play important role in the physics of graphene. They are named Dirac points because at these points the electrons behave as Dirac fermions. The position of the Dirac points in momentum space is

$$\vec{K}_0 = \frac{4\pi}{3\sqrt{3}a_0}\,(1,0)\,, \quad -\vec{K}_0 = \frac{4\pi}{3\sqrt{3}a_0}\,(-1,0)\,. \tag{5.4}$$

In order to derive the electronic band structure of graphene, we assume an infinitely extended sheet of graphene and neglect the finite size effects which allows us to impose periodic boundary conditions (PBC) for the graphene honeycomb lattice L_G. Employing Bloch's theorem, we can solve the single particle Schrödinger equation for the wave functions $\varphi_{\alpha\vec{k}}(\vec{r})$ describing p_z-electrons in the graphene lattice with a crystal momentum $\vec{k}$ and band index $\alpha = \pm$ which characterizes the Bloch waves associated with the two atoms per unit cell. To describe the p_z-electrons, we solve the single particle Schrödinger equation [87, 106]

$$\hat{H}_G(\vec{r})|\varphi_{\alpha\vec{k}}\rangle = \varepsilon_{\alpha\vec{k}}|\varphi_{\alpha\vec{k}}\rangle, \tag{5.5}$$

where $\varphi_{\alpha\vec{k}}$ is the wave function of a p_z-electron which can be expressed as a linear combination of single p_z-electron wave functions $\chi(\vec{r})$ associated with sublattice p at lattice site $\vec{R} + \vec{\tau}_p$ as

$$\varphi_{\alpha\vec{k}}(\vec{r}) = \sum_{\vec{R}\in L_G}\sum_{p=\pm} f_{p\alpha\vec{k}}\, e^{i\vec{k}\cdot\vec{R}}\chi(\vec{r} - \vec{R} - \vec{\tau}_p), \tag{5.6}$$

where $\alpha = \pm$ denotes the conduction and valence bands, respectively. The Hamiltonian $\hat{H}_G(\vec{r})$ can be expressed in real space as

$$\hat{H}_G(\vec{r}) = -\frac{\hbar^2\vec{\nabla}^2}{2m} + \sum_{\vec{R}\in L_G}\sum_{p} v_c(\vec{r} - \vec{R} - \vec{\tau}_p), \tag{5.7}$$

where $v_c(\vec{r} - \vec{R} - \vec{\tau}_p)$ describes the interaction of the p_z electron with the ionized carbon atom at position $\vec{R} + \vec{\tau}_p$. The detailed solution and analysis can be found in Refs. [87, 110, 111]. Here we present a short review only. The solution of Eq. (5.5) yields the energy bands of graphene lattice in the form

$$\varepsilon_\pm(\vec{k}) = \pm\gamma_0\sqrt{1 + 4\cos\left(\frac{\sqrt{3}a_0k_x}{2}\right)\cos\left(\frac{3a_0k_y}{2}\right) + 4\cos^2\left(\frac{\sqrt{3}a_0k_x}{2}\right)}, \tag{5.8}$$

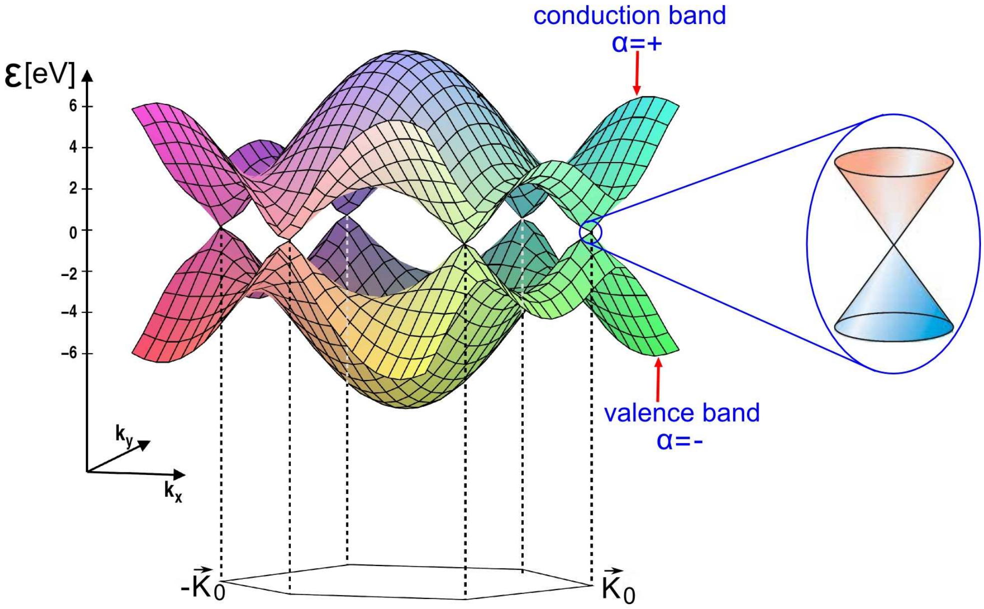

Figure 5.2: (a) Schematic diagram for the band structure of graphene where the two bands (characterized by $\alpha = \pm$) touch at six Fermi points. The two inequivalent Fermi points are represented by $\vec{K}_0$ and $-\vec{K}_0$. On the right: zoom in of the energy bands close to one of the Dirac points is shown. Parts of this figure have been reproduced from [112].

where γ_0 is the transfer integral between nearest-neighbor carbon atoms. In Fig. 5.2, we have shown the full band structure of graphene and a zoom in of the band structure close to one of the Dirac points (at the $\vec{K}_0$ or $-\vec{K}_0$ point in the BZ) with linear dispersion, where the low energy theory is relevant. In the above equation, the plus sign denotes the upper (π^*) and the minus sign the lower (π) band. It is clear from Eq. (5.8) that the spectrum is symmetric around zero energy meaning that electron-hole symmetry is retained. It is also obvious that $\varepsilon_\pm(\vec{K}_0) = \varepsilon_\pm(-\vec{K}_0) = 0$. The expansion of the above energy bands close to the $\vec{K}_0$ and $-\vec{K}_0$ Fermi points reads

$$\varepsilon_\pm(\vec{k} + \vec{K}_0) = \varepsilon_\pm(\vec{k} - \vec{K}_0) = \pm\gamma\sqrt{k_x^2 + k_y^2}, \tag{5.9}$$

with

$$\gamma = \frac{\sqrt{3}a_0\gamma_0}{2}, \tag{5.10}$$

for $|\vec{k}|a_0 \ll 1$ and $\gamma = \hbar v_F$ with v_F is the Fermi velocity. In neutral graphene, the chemical potential crosses exactly the Dirac point. This linear dispersion in the vicinity of the Fermi points $\vec{K}_0$ and $-\vec{K}_0$ plays crucial role in various electronic and transport properties of 2D graphene and carbon nanotubes. This particular dispersion, that is only valid at low energies, mimics the physics of quantum electrodynamics (QED) for massless fermions except for the fact that in graphene the Dirac fermions move with Fermi velocity v_F, which is 300 times smaller than the speed of light c [108, 109]. Thus graphene exhibits many unusual properties like that of QED at much smaller speed than light. Hence, one of the most interesting feature of the graphene structure is the fact that its low-energy excitations are similar to the ones of massless, chiral, Dirac fermions [108,109]. It is also important to mention that the Dirac excitations near the Fermi point $\vec{K}_0$ cannot be described as the antiparticles of those near the Fermi point $-\vec{K}_0$. However, the two possible combinations of the excitations near one Dirac point on the sublattices A and B, with energies $\pm\hbar v_F|\vec{\kappa}|$ respectively, are the antiparticles of one another.

5.2 From graphene to carbon nanotube

A single-wall carbon nanotube is a graphene sheet wrapped into a cylindrical geometry so that the resulting structure acquires an axial symmetry. Generally, the arrangement of atoms in the nanotube exhibits a spiral structure which is characterized by the so-called chiral vector. This feature plays an important role in determining the electronic properties. Carbon nanotubes can mainly be classified into achiral and chiral types on the basis of symmetry. An achiral carbon nanotube is the one with a spiral symmetry such that its mirror image reflects the original one. It turns out that in achiral nanotubes, one side of the hexagons is parallel or perpendicular to the cylindrical axis. This type of nanotubes is further classified into armchair and zigzag where the nomenclature is associated with the cross-section of the tube as displayed in Fig. 5.3. A chiral carbon nanotube is the one without the mirror symmetry. In order to proceed and understand the different types of carbon nanotubes in a better way, we define the chiral vector, which later on becomes the circumference of the tube. In terms of the graphene lattice basis vectors in real space, the chiral vector can be written as [106]

$$\vec{C}_{n,m} = n\vec{a}_1 + m\vec{a}_2, \ n, m \in \mathbb{Z}^+. \tag{5.11}$$

Hence, armchair nanotubes are characterized by the chiral vectors $\vec{C}_{n,n}$, whereas the chiral vectors $\vec{C}_{n,0}$ describe the zigzag tubes, while $\vec{C}_{n,m}$ with $m \neq 0, n$ represent the chiral tubes, see Fig. 5.3. Thus folding of graphene sheet results in a tube with axis perpendicular to the chiral vector $\vec{C}_{n,m}$. Due to the hexagonal symmetry of the graphene honeycomb lattice, the set of chiral vectors $\{\vec{C}_{n,m}\}$ with $0 \leq |m| \leq n$ can describe all possible helical arrangements of SWCNTs. In real space, the unit cell of the carbon nanotube is characterized by a rectangular structure constructed by the chiral vector $\vec{C}_{n,m}$ and translational vector $\vec{T}$. The latter represents the unit vector of carbon nanotube which is directed along the tube axis and is given by [106]

$$\vec{T} = t_1\vec{a}_1 + t_2\vec{a}_2. \tag{5.12}$$

Since the translational vector is perpendicular to the chiral vector, therefore, the integers t_1 and t_2 can be determined using the condition $\vec{C}_{n,m} \cdot \vec{T} = 0$ which yields

$$t_1 = \pm\frac{2m+n}{\gcd(2n+m, n+2m)}, \ t_2 = \mp\frac{2n+m}{\gcd(2n+m, n+2m)}. \tag{5.13}$$

In the above equation, the division by the greatest common divisor shows that the translational vector $\vec{T}$ represents an axial vector with minimum length. We can also

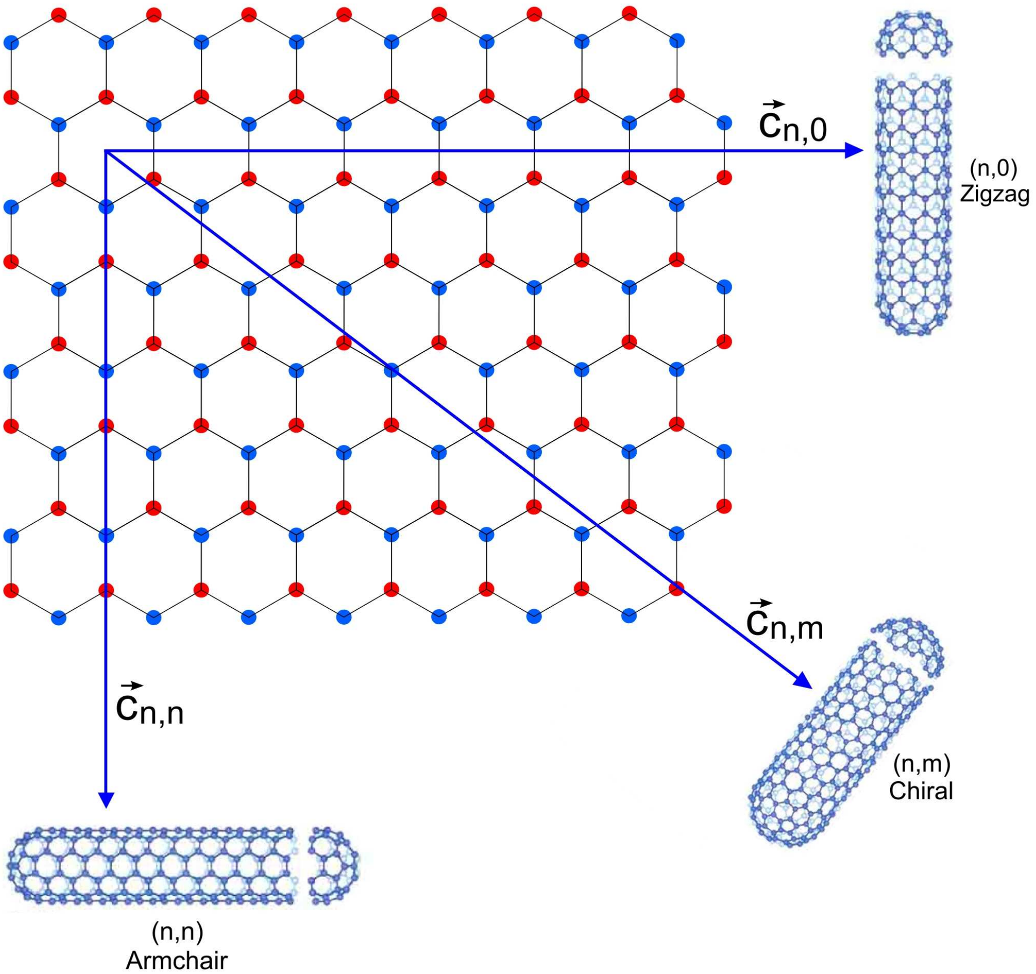

Figure 5.3: Different geometries of SWCNTs originate from different chiral vectors.

find the tube diameter d as follows

$$d = \frac{|\vec{C}_{n,m}|}{\pi} = \frac{a_0}{\pi}\sqrt{3(n^2+m^2+nm)}. \tag{5.14}$$

5.3 Low energy theory of armchair metallic SWCNTs

In a graphene sheet, the conduction and valence bands touch at the Fermi points $\vec{K}_0$ and $-\vec{K}_0$. First-principle calculations show that electronic properties can be altered for tubes with an extremely small diameter because of a hybridization of π states with σ bands which lie well below the Fermi level in 2D graphite [113]. However, for SWCNT with a large diameter, the effects arising from finite curvature of the graphene sheet can safely be ignored and therefore electronic states in the vicinity of the Fermi level are determined by the states near the $\vec{K}_0$ and $-\vec{K}_0$ points. In this section, a theoretical description of SWCNTs appropriate in the linear dispersion regime above half-filling is presented. The detail can be found in Ref. [87]. In order to derive the low energy many body Hamiltonian of armchair tubes, we start with the graphene Bloch waves associated with carbon honeycomb lattice described by Eq. (5.6), and using the zone folding we obtain the proper SWCNT wave functions for periodic boundary conditions (PBCs) along the tube axis. However, for a finite size system, it is more convenient to use open boundary conditions (OBCs) rather than PBCs to obtain standing waves instead of traveling waves description for electrons.

5.3.1 Armchair metallic SWCNTs at low energies

In armchair SWCNTs at low energies and under periodic boundary conditions only the gapless energy subbands with linear dispersion touching at the Fermi points $F = \pm K_0\hat{e}_x$, where $\hat{e}_x$ is directed along the tube axis, are relevant [114, 115]. In order to derive a wave function for the description of electrons in the SWCNT quantum dot, we consider an armchair tube of finite length L_d. According to the coordinate system introduced in Fig. 5.1, the axial direction is along $x-$axis. At the two ends of the tube, $x = 0$ and $x = L_\mathrm{d}$, open boundary conditions are appropriate such that the wave function must vanish at the tube end points. The boundary conditions can be satisfied only if the wave functions belonging to the two inequivalent Fermi points $\vec{K}_0$ and $-\vec{K}_0$, Eq. (5.6), of the first Brillouin zone of graphene are mixed. The appropriate linear combination of the Bloch waves is [87, 116]

$$\varphi_{r\kappa}(\vec{r}) = \frac{1}{\sqrt{2}}\sum_F \mathrm{sgn}(F)e^{i\mathrm{sgn}(F)\kappa x}\sum_p f_{pr}\varphi_{pF}(\vec{r}), \tag{5.15}$$

where the prefactors f_{pr} are

$$f_{pr} := \frac{1}{\sqrt{2}}\begin{cases} 1, & \text{for} \quad p = +, \\ -\mathrm{sgn}(r), & \text{for} \quad p = -. \end{cases} \tag{5.16}$$

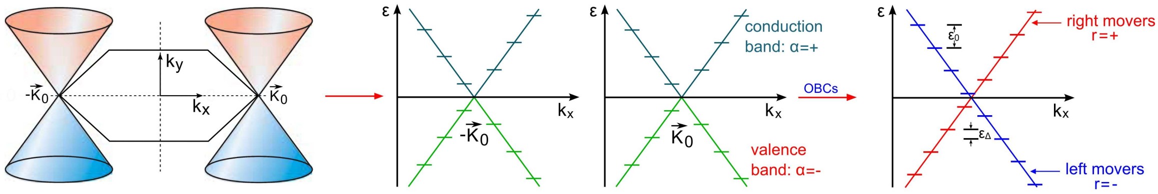

Figure 5.4: Schematic representation of the open boundary conditions (OBCs) which map the low energy dispersion in the vicinity of the two Fermi-points onto two linear branches, $r = \pm$, with slopes $\pm\hbar v_F$. The factors ε_0 and ε_Δ denote the level spacing and the orbital mismatch energy, respectively.

The function $\varphi_{pF}(\vec{r})$ describes fast oscillating Bloch waves on the graphene sublattice $p = \pm$ at the Fermi point $F = \pm K_0\hat{e}_x$ which is given by

$$\varphi_{pF}(\vec{r}) = \frac{1}{\sqrt{N_L}} \sum_{\vec{R}\in L_G} e^{iFR_x}\chi(\vec{r} - \vec{R} - \vec{\tau}_p), \tag{5.17}$$

where N_L specifies the total number of sites in the carbon nanotube Bravais lattice. The allowed values for the quasi-momentum are given by

$$\kappa = \frac{\pi}{L_\mathrm{d}}(n_\kappa + \Delta),\ n_\kappa \in \mathbb{Z},\ |\Delta| \le 1/2, \tag{5.18}$$

where L_d is the length of the tube and Δ accounts for a small offset that may be necessary if K_0 is not an integer multiple of π/L_d. The linear dispersion relation is shown in Fig. 5.4, where the two linear branches $r = \pm$ correspond to right and left moving waves with slopes $\pm\hbar v_F$, where v_F is the Fermi velocity.

The 3D field operator for an electron with spin σ at position $\vec{r}$ inside the SWCNT can be described as

$$\hat{\Psi}_\sigma(\vec{r}) = \sum_{r\kappa} \varphi_{r\kappa}(\vec{r})\hat{c}_{r\sigma\kappa}, \tag{5.19}$$

where $\hat{c}_{r\sigma\kappa}$ annihilates an electron in the nanotube with momentum κ and spin σ in branch r. Equivalently, one can express the above relation as

$$\hat{\Psi}_\sigma(\vec{r}) = \sqrt{L_d} \sum_{rFp} \mathrm{sgn}(F) f_{pr} \varphi_{pF}(\vec{r})\hat{\psi}_{rF\sigma}(x), \tag{5.20}$$

where a slowly varying 1D electron operator is defined as

$$\hat{\psi}_{rF\sigma}(x) = \frac{1}{\sqrt{2L_\mathrm{d}}} \sum_{\kappa} e^{i\mathrm{sgn}(F)\kappa x}\hat{c}_{r\sigma\kappa}. \tag{5.21}$$

5.3.2 Hamiltonian of metallic armchair SWCNTs

At low energies, the Hamiltonian describing p_z electrons in metallic armchair SWCNTs can be readily determined from the dispersion relation of the standing waves $\varphi_{r\kappa}(\vec{r})$ shown in Fig. 5.4. Hence, taking into account the spin and pseudo spin degrees of freedom, the Hamiltonian of the noninteracting electrons can be described as [87, 116]

$$\hat{H}_0 = \hbar v_F \sum_{r\sigma\kappa} r\kappa \hat{c}^\dagger_{r\sigma\kappa}\hat{c}_{r\sigma\kappa}, \tag{5.22}$$

where $\hat{c}_{r\sigma\kappa}$ is the fermionic operator which annihilates an electron in the state $|\varphi_{r\kappa}\rangle|\sigma\rangle$. Note that the summation over κ corresponds to the states in the vicinity of the Fermi points. Using the quantized form of κ from Eq. (5.18), the above Hamiltonian acquires the form

$$\hat{H}_0 = \varepsilon_0 \sum_{r\sigma} r \sum_{n_\kappa} n_\kappa \hat{c}^\dagger_{r\sigma\kappa}\hat{c}_{r\sigma\kappa} + \varepsilon_\Delta \sum_{r\sigma} r\hat{\mathcal{N}}_{r\sigma}, \tag{5.23}$$

where $\varepsilon_0 = \hbar v_F \pi / L_{\mathrm{d}}$ is the level spacing of the noninteracting SWCNTs, whereas $\varepsilon_\Delta = \varepsilon_0 \Delta$ accounts for the possible band mismatch between the left $(r = -)$ and right $(r = +)$ moving states. $\hat{\mathcal{N}}_{r\sigma}$ is the number operator that counts the total number of electrons in branch r with spin σ. Note that the four different electron species can be specified by: $r\sigma = +\uparrow, +\downarrow, -\uparrow, -\downarrow$.

5.4 Vibrational modes in SWCNTs

As we pointed out in Chapter 2, quantum dots are very sensitive to the influence of vibrational modes in nanoscale systems. In many experiments on suspended graphene [117] and carbon nanotubes [118–124], electromechanical oscillations have been observed. On the other hand, well-pronounced vibrational signatures in electronic transport have been studied in several other experiments on suspended SWCNT quantum dots [43–45]. The results of these experiments imply that the transport properties of carbon nanotubes are strongly affected by vibrations. Indeed, several vibrational modes can occur in suspended SWCNTs. However, only radial breathing modes [125] and longitudinal stretching modes [43–45, 126] have been observed in transport experiments. To explain the vibrational effects in SWCNTs, many theoretical approaches [43, 93, 127] considered the electron-vibron coupling as a mechanical deformation of the nanotube produced by the electrostatic interaction between the charge on the tube and some external potential source, e.g., nearby gate electrode or disorder. However, the electron-vibron coupling achieved in these approaches is not large enough to explain the experimental results. In another approach, the low-energy vibrational excitations of the nanotube are described in terms of low-energy acoustic modes [128–133]. These modes are coupled to the electronic degrees of freedom via a deformation potential (associated with local variations in area) combined with bond length modifications. However, the latter coupling mechanism has a coupling constant an order of magnitude smaller than the one associated with the deformation potential [130]. Taking into account the symmetry arguments, one can find which modes couple strongly to the electronic degrees of freedom. Here we highlight a few vibrational modes associated with suspended SWCNTs that can significantly influence the transport properties of these systems.

5.4.1 Longitudinal stretching mode

Longitudinal stretching mode (LSM) involves a deformation potential (local area variations) together with bond length modifications which can lead to a strong electron-vibron coupling. The coupling constant associated with LSM is very sensitive to the rel-

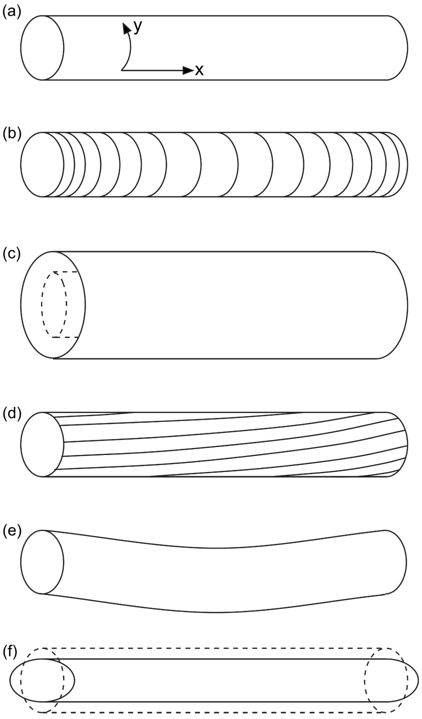

Figure 5.5: Acoustic vibron modes in SWCNT. (a) Unperturbed carbon nanotube with coordinate system such that x-axis points in the axial direction of the tube and y-axis in the circumferential direction. (b) Longitudinal stretching mode. (c) Radial breathing mode. (d) Twist mode. (e) Bending mode with gapless dispersion, and (f) bending mode with finite gap dispersion. This figure is taken from [128].

ative size and relative position of the quantum dot and its associated vibron. Schematically, LSM is shown in Fig. 5.5(b). The energies of different vibrational modes and electronic excitations as a function of the tube length have been shown in Fig. 5.6, where it is clear that the energy of the longitudinal stretching mode is next in magnitude to the electronic excitation energy and also depends on the length of the tube. Thus in doubly clamped SWCNTs, stretching modes can be retained in transport calculations, in agreement with experimental conclusions [43].

5.4.2 Radial breathing mode

Similar to longitudinal stretching modes, radial breathing modes also involve local area variations and thus couple strongly via the deformation potential to the electronic degrees of freedom. The dispersion relation of the breathing mode is well described in terms of a finite frequency ω_{B} in the long wavelength limit. Using the parameters of bulk graphites, the vibronic excitation energy $\hbar\omega_{\mathrm{B}}$ for (10,10) armchair SWCNT has value of $\hbar\omega_{\mathrm{B}} \simeq 2 \times 10^{-2}$ eV [128, 130], which is larger than that of the low-energy electrons in the vicinity of Fermi energy. Such a mode is schematically depicted in Fig. 5.5(c). Fig. 5.6 reveals that the energy of the breathing mode is higher than the electronic excitation energy and does not depend on the length of the tube. Hence, breathing modes lie too high in energy to be excited in low-bias transport experi-

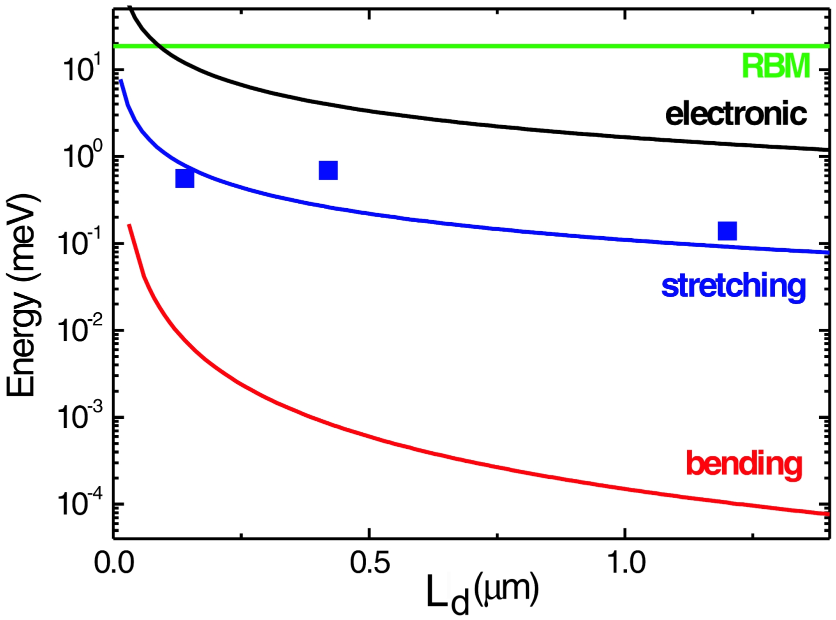

Figure 5.6: Log scale plot of energy scales for different vibrational modes and electronic excitations for a (10,10) nanotube. The red curve denotes the excitations of bending modes, blue refers to the stretching mode, black to the electronic excitation and green to the excitations associated with radial breathing modes. Note that breathing mode does not depend on the length of the tube. This figure is taken from [43].

ments. It implies that radial breathing modes can be neglected in low bias transport calculations since they cannot get populated in this energy limit.

5.4.3 Twist mode

Twist modes are associated with pure shear, see Fig. 5.5(d), and thus couple to electronic degrees of freedom only via a bond length modification [128, 130]. The linear dispersion of the twist modes produces a coupling constant that depends only on the circumference of the nanotube. Hence, these modes are weakly coupled to electrons and cannot cause well pronounced vibrational signatures to be observed in transport experiments. It means that they do not play a significant role and can be neglected.

5.4.4 Bending mode

Bending mode, though coupling via the dominant deformation potential, does not play a significant role [128, 130]. In fact, these modes couple only quadratically to the electronic degrees of freedom and cannot produce a significant electron-vibron coupling. Hence, bending modes also cannot generate well pronounced Franck-Condon blockade nor vibrational sidebands at large bias in transport measurements on suspended SWCNT. As an example, bending modes are sketched in Fig. 5.5(e-f) in the form of two different configurations. Fig. 5.6 shows that the energy of the bending mode is very small compared to the other modes and strongly depends on the length of the tube.

Hence, these modes can also be excluded in the transport calculations of suspended SWCNTs.

It turns out that longitudinal stretching modes and radial breathing modes are the natural candidates that couple strongly to electronic degrees of freedom, in agreement with experimental conclusions [43–45, 125, 126]. However, in the next chapter we take into account only longitudinal stretching modes since the focus will be on the low energy theory of suspended armchair metallic SWCNTs.

Chapter 6

Spectrum and Franck-Condon factors of interacting suspended SWCNTs

The spectrum and Franck-Condon factors of suspended single wall carbon nanotubes strongly depend on the geometric configuration of the junction in the presence of several vibronic modes. The relative size and relative position of the SWCNT quantum dot and the associated vibrons significantly influence the electromechanical properties of the system as already pointed out in many theoretical works [89, 128]. In this chapter, we extend their ideas and identify a parameters space where the dependence of the spectrum and the Franck-Condon couplings on the geometry of the system is addressed, see Fig. 6.1. We calculate the spectrum and the tunneling amplitudes over the entire parameters space varying the relative length and relative position of the vibron with respect to the quantum dot including the effect of higher vibronic modes. The treatment of a wide parameters space is relevant since it allows for a unified picture of different results presented in the literature [89, 93]. In this approach, we can identify a region in the parameters space where strong FC couplings are expected to be achieved.

6.1 Suspended SWCNTs at low-energy

The low energy spectrum of finite-size, interacting metallic armchair single-wall carbon nanotubes (SWCNTs) has been discussed in [134] within a mean-field approach and in [71, 116] within a bosonization framework going beyond the mean-field results. Bosonization is also the natural approach to include the effects of the coupling to the longitudinal stretching modes [89, 93]. Here, following [71, 89, 93], we derive and discuss the spectrum and many body states of suspended metallic SWCNTs. Particular emphasis will be given to the dependence of the electron-vibron coupling on the geometrical configuration of the system. An analytical expression for the electron-vibron coupling constants in terms of the relevant geometrical parameters is derived and plays a crucial role in the analysis of the spectrum and the matrix elements conducted in

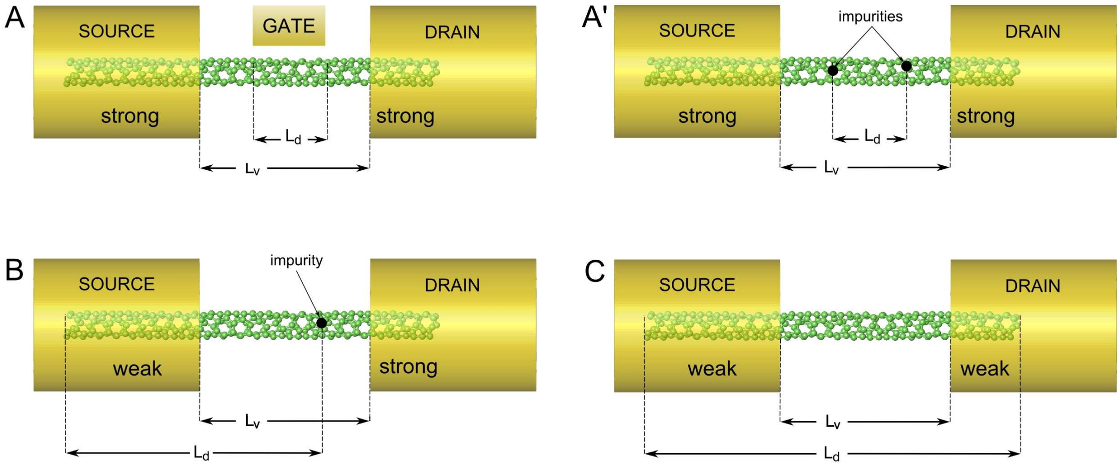

Figure 6.1: Different realizations of a nanojunction with a suspended SWCNT. The lengths L_d of the quantum dot and L_v of the vibrons are also indicated together with their position. The length and position of the vibrons is assumed to coincide with the suspended part of the tube. The length and position of the dot depend instead on many factors like for example the weak or strong hybridization of the SWCNT and the metallic leads and the presence of impurities or of side gates. The labeling of the different configurations is given according to the general one used in Fig. 6.2.

the following sections. We thus consider a Hamiltonian of the form

$$\hat{H}_\mathrm{sys} = \hat{H}_0 + \hat{V}_\mathrm{ee} + \hat{H}_\mathrm{v} + \hat{H}_\text{e-v}, \tag{6.1}$$

where $\hat{H}_0$ is the noninteracting Hamiltonian of a finite-size, metallic SWCNT described explicitly by Eq. (5.23), $\hat{V}_\mathrm{ee}$ characterizes the electron-electron interaction, $\hat{H}_\mathrm{v}$ is associated with the longitudinal stretching modes, whereas $\hat{H}_\text{e-v}$ describes the electron-vibron coupling.

6.1.1 Coulomb interaction in SWCNTs

In this section, the electron-electron interaction in metallic armchair SWCNTs is discussed. We briefly analyze the consequences of the Coulomb interaction inducing different types of scattering processes. The Coulomb interaction between electron-electron assumes the standard form in second quantization as

$$\hat{V}_\mathrm{ee} = \frac{1}{2}\sum_{\sigma,\sigma'}\int \mathrm{d}\vec{r} \int \mathrm{d}\vec{r}\,'\hat{\Psi}^\dagger_\sigma(\vec{r})\hat{\Psi}^\dagger_{\sigma'}(\vec{r}\,')U(\vec{r}-\vec{r}\,')\hat{\Psi}_{\sigma'}(\vec{r}\,')\hat{\Psi}_\sigma(\vec{r}), \tag{6.2}$$

where $U(\vec{r}-\vec{r}\,')$ is the screened Coulomb potential which takes into account the localized character of the p_z orbitals. For the actual calculations we model it by the so-called Ohno potential [116]

$$U(\vec{r}-\vec{r}\,') = U_0\left[1+\left(\frac{U_0\epsilon|\vec{r}-\vec{r}\,'|}{\alpha}\right)^2\right]^{-1/2}, \tag{6.3}$$

where a reasonable choice of the onsite energy is $U_0 = 15\,\mathrm{eV}$ [116], the dielectric constant is $\epsilon \approx 1.4 - 2.4$ and $\alpha = 14.397\,\mathrm{eV\AA}$.

The Coulomb interaction causes Umklapp, backward and forward scattering processes among the electrons. Away from half filling it is reasonable to neglect Umklapp scattering. We also disregard backscattering processes, which is a valid approximation for nanotubes with not too small radii [116]. The forward scattering processes can be fully included within a Tomonaga-Luttinger (TL) model for SWCNTs [93,114], yielding the TL Hamiltonian

$$\hat{H}_0 + \hat{V}_{\mathrm{ee}} \approx \hat{H}_{\mathrm{TL}} = \hat{H}_{\mathrm{N}} + \sum_j \hat{H}_j, \tag{6.4}$$

where $\hat{H}_{\mathrm{N}}$ describes the fermionic configuration of the nanotube and $\hat{H}_j$ represents the bosonic excitations with the index $j = c+, s+, c-, s-$ labeling the four excitation sectors for total charge, total spin, and relative (with respect to the two electronic subbands) charge and relative spin, respectively. The fermionic component of Eq. (6.4) can be casted into the form

$$\hat{H}_{\mathrm{N}} = \frac{\varepsilon_0}{4} \sum_j \frac{\hat{N}_j^2}{2} + \varepsilon_\Delta \hat{N}_{c-} + E_{\mathrm{c}} \frac{\hat{N}_{c+}^2}{2}, \tag{6.5}$$

where the particle number operators for the different charge and spin sectors are defined by $\hat{N}_{c+} = \sum_{r\sigma} \hat{N}_{r\sigma}$, $\hat{N}_{c-} = \sum_{r\sigma} \mathrm{sgn}(r)\hat{N}_{r\sigma}$, $\hat{N}_{s+} = \sum_{r\sigma} \mathrm{sgn}(\sigma)\hat{N}_{r\sigma}$ and $\hat{N}_{s-} = \sum_{r\sigma} \mathrm{sgn}(r\sigma)\hat{N}_{r\sigma}$, and the operator $\hat{N}_{r\sigma}$ counts the particles with spin σ and pseudospin r. The electron-electron interaction is parametrized, in the fermionic part of the Hamiltonian, by E_{c}, *i.e.* the charging energy of the SWCNT quantum dot. Finally, $\hat{H}_j$ describes the bosonic excitation of the sector j. In the long wavelength limit, it reads

$$\hat{H}_j = \frac{\varepsilon_0}{g_j} \sum_{n \geq 1} n\, \hat{b}_{j,n}^\dagger \hat{b}_{j,n}, \tag{6.6}$$

where the sum runs over the mode number n. Due to the Coulomb interaction the factor $g_j < 1$ for the sector $c+$, whereas $g_j = 1$ for the other cases. For unscreened interaction $g_{c+} \approx 0.2$ [114, 116].

6.1.2 Vibron Hamiltonian

The low-energy vibrational excitations of the nanotube can be described in terms of low-energy acoustic modes and only longitudinal stretching modes can be retained as we explained in Chapter 5. The stretching mode Hamiltonian is expressed in a continuum model as [93]

$$\hat{H}_{\mathrm{v}} = \frac{1}{2} \int_{x_{\mathrm{v}} - \frac{L_{\mathrm{v}}}{2}}^{x_{\mathrm{v}} + \frac{L_{\mathrm{v}}}{2}} \mathrm{d}x \left[\frac{1}{\zeta} \hat{P}^2(x) + \zeta v_{\mathrm{st}}^2 \left(\partial_x \hat{u}(x)\right)^2 \right], \tag{6.7}$$

where $\zeta = 2\pi R M$, with R being the tube radius, M the carbon mass per unit area and v_{st} is the velocity of the longitudinal stretching mode. Moreover, x_{v} and L_{v} are

the position of the centre and the length of the vibron, respectively. Typical SWCNT parameters are: $v_{\mathrm{st}} = 2.4 \times 10^4$ m/s, $M = 3.80 \times 10^{-7}$ kg/m^2.
Note that the positions and the lengths of the dot and of the vibron do not necessarily coincide. The length of the vibron (L_{v}) is readily estimated as the distance between the electrodes that clamp the nanotube and it is defined as the length of the free-standing portion of the tube. Instead, the relation between the size L_{d} of the quantum dot and the geometrical properties of the junction is much more complex. The best way of estimating L_{d} is to extract it from transport measurements, which give the mean-level spacing and the charging energy of the system. The position of the centre of the dot x_{d} can be taken as a free parameter.
In Fig. 6.1, we sketch four possible physical realizations of different configurations. In panels A and A′ the dot lies inside the vibrating part of the tube. The confinement is obtained by a side gate (A) or by impurities located on the tube (A′), whereas the rest of the tube is electrically absorbed into the leads due to the strong tube-lead hybridization (extended lead configuration). In panel C, the dot coincides with the entire tube length due to the weak hybridization between the SWCNT and the metallic leads and fully contains the vibrating fraction of the tube. Finally, a somehow mixed scenario is illustrated in panel B. The displacement and momentum field operators read [135]

$$\begin{aligned}\hat{u}(x) &= \sqrt{\frac{\hbar}{\zeta v_{\mathrm{st}} L_{\mathrm{v}}}} \sum_{m\geq 1} \sin\left[k_m\left(x - x_{\mathrm{v}} + \frac{L_{\mathrm{v}}}{2}\right)\right] \frac{1}{\sqrt{k_m}} \left(\hat{a}_m^\dagger + \hat{a}_m\right), \\ \hat{P}(x) &= \mathrm{i}\sqrt{\frac{\hbar\zeta v_{\mathrm{st}}}{L_{\mathrm{v}}}} \sum_{m\geq 1} \sin\left[k_m\left(x - x_{\mathrm{v}} + \frac{L_{\mathrm{v}}}{2}\right)\right] \sqrt{k_m} \left(\hat{a}_m^\dagger - \hat{a}_m\right),\end{aligned} \tag{6.8}$$

with $k_m = m\pi/L_{\mathrm{v}}$ the wave number. Here $\hat{a}_m(\hat{a}_m^\dagger)$ are the annihilation (creation) operators associated with the mth vibron mode obeying the commutation relation $[\hat{a}_m, \hat{a}_{m'}^\dagger] = \delta_{m,m'}$. Using the above field operators, we obtain

$$\hat{H}_{\mathrm{v}} = \sum_{m\geq 1} E_m \left(\hat{a}_m^\dagger \hat{a}_m + \frac{1}{2}\right), \tag{6.9}$$

with $E_m = m\hbar v_{\mathrm{st}}\pi/L_{\mathrm{v}} \equiv m\hbar\omega$.

6.1.3 Electron-vibron interaction Hamiltonian

So far in most cases of the transport calculations, Anderson-Holstein (AH) model has been considered in which the vibrational degree of freedom couples only to the total charge of the quantum dot. This model generates position-independent Franck-Condon (FC) factors [57,58,136–138] which have profound consequences on the transport properties of nanojunctions. However, in suspended SWCNTs vibrons couple both to the total charge of the dot and to the spatial fluctuations of the electron density [89,128]. In this case, the size and location of the dot and of the vibron do not coincide in general and position-dependent FC factors can be produced which strongly affect the transport properties of the system. Hence, the electron-vibron are microscopically coupled via the Hamiltonian

$$\hat{H}_{\text{e-v}} = \int \mathrm{d}\vec{r}\hat{\rho}(\vec{r})\hat{V}(\vec{r}), \tag{6.10}$$

where $\hat{\rho}(\vec{r}) = \sum_\sigma \hat{\Psi}^\dagger_\sigma(\vec{r})\hat{\Psi}_\sigma(\vec{r})$ is the electron-density and $\hat{V}(\vec{r}) = g\partial_x\hat{u}(x)$ is the deformation potential for the stretching vibron mode. The coupling constant g is estimated to be $g \approx 20-30$ eV [130]. Substituting the values of the corresponding quantities and integrating over the radial and azimuthal coordinates, the above equation acquires the form

$$\hat{H}_{\text{e-v}} = g\sum_{m\geq 1}\left(\frac{\hbar k_m}{\zeta v_{\text{st}} L_{\text{v}}}\right)^{1/2}\left(\hat{a}^\dagger_m + \hat{a}_m\right)\int_{\text{d}\cap\text{v}} \mathrm{d}x\hat{\rho}_{\text{1D}}(x)\cos\left[k_m\left(x - x_{\text{v}} + \frac{L_{\text{v}}}{2}\right)\right], \tag{6.11}$$

where the integral is calculated over the overlap of the dot and vibron region and the effective one-dimensional (1D) density operator $\hat{\rho}_{\text{1D}}(x)$ reads, in its bosonized form [71],

$$\hat{\rho}_{\text{1D}}(x) = \frac{\hat{N}_{c+}}{L_{\text{d}}} + \frac{2}{\sqrt{\pi\hbar}}\partial_x\hat{\phi}_{c+}(x). \tag{6.12}$$

Note that the bosonic field $\hat{\phi}_{c+}(x)$ can be expressed in terms of the bosonic creation and annihilation operators $\hat{b}^\dagger_{c+,n}$ and $\hat{b}_{c+,n}$ as

$$\hat{\phi}_{c+}(x) = \sqrt{\frac{\hbar g_{c+}}{L_{\text{d}}}}\sum_{n\geq 1}\sin\left[k_n\left(x - x_{\text{d}} + \frac{L_{\text{d}}}{2}\right)\right]\frac{1}{\sqrt{k_n}}(\hat{b}^\dagger_{c+,n} + \hat{b}_{c+,n}), \tag{6.13}$$

where $k_n = n\pi/L_{\text{d}}$ and we have imposed open boundary conditions $\hat{\rho}(x_{\text{d}} - L_{\text{d}}/2) = \hat{\rho}(x_{\text{d}} + L_{\text{d}}/2) = 0$. It is useful, for the diagonalization procedure presented in the next subsection, to introduce the dimensionless position and momentum operators for the nth plasmon mode $\{\hat{X}_n, \hat{P}_n\}$ and the ones of the mth vibronic mode $\{\hat{x}_m, \hat{p}_m\}$

$$\begin{aligned}\hat{X}_n &= \frac{\hat{b}_{c+,n} + \hat{b}^\dagger_{c+,n}}{\sqrt{2}}, & \hat{x}_m &= \frac{\hat{a}_m + \hat{a}^\dagger_m}{\sqrt{2}},\\ \hat{P}_n &= \frac{\hat{b}_{c+,n} - \hat{b}^\dagger_{c+,n}}{\mathrm{i}\sqrt{2}}, & \hat{p}_m &= \frac{\hat{a}_m - \hat{a}^\dagger_m}{\mathrm{i}\sqrt{2}},\end{aligned} \tag{6.14}$$

which satisfy the canonical commutation relations $[\hat{X}_n, \hat{P}_{n'}] = \mathrm{i}\delta_{nn'}$ and $[\hat{x}_m, \hat{p}_{m'}] = \mathrm{i}\delta_{mm'}$. In terms of these operators the electron-vibron Hamiltonian can be written as

$$\begin{aligned}\hat{H}_{\text{e-v}} = I\sqrt{g_{c+}}&\sum_{n,m\geq 1}\sqrt{nm}K_{nm}(\lambda,\delta)2\hat{X}_n\hat{x}_m\\ + I&\sum_{m\geq 1}\sqrt{m}L_m(\lambda,\delta)\sqrt{2}\hat{N}_{c+}\hat{x}_m\end{aligned} \tag{6.15}$$

where

$$I = g\sqrt{\frac{\hbar\pi}{\zeta v_{\mathrm{st}} L_{\mathrm{d}}^2}} \tag{6.16}$$

is the fundamental coupling constant; it acquires the value $I = 88$ μeV for a $(10, 10)$ SWCNT with $L_{\mathrm{d}} = 1$ μm and assuming $g = 30$ eV.
The *geometric* part of the electron-vibron coupling is given by the dimensionless matrix

$$\begin{aligned} K_{nm}(\lambda, \delta) =& \frac{1}{\lambda}\int_{x_{\mathrm{min}}}^{x_{\mathrm{max}}} \mathrm{d}x \left\{ \cos\left[\pi x\left(n + \frac{m}{\lambda}\right) - \frac{m\pi}{\lambda}\left(\delta + \frac{1-\lambda}{2}\right)\right]\right. \\ &\left. + \cos\left[\pi x\left(n - \frac{m}{\lambda}\right) + \frac{m\pi}{\lambda}\left(\delta + \frac{1-\lambda}{2}\right)\right]\right\} \end{aligned} \tag{6.17}$$

for the plasmon-vibron component and by the vector

$$L_m(\lambda, \delta) = \frac{1}{\lambda}\int_{x_{\mathrm{min}}}^{x_{\mathrm{max}}} \mathrm{d}x \cos\left[\frac{m\pi}{\lambda}\left(x - \delta - \frac{1-\lambda}{2}\right)\right] \tag{6.18}$$

for the charge-vibron component. The integration limits

$$\begin{aligned} x_{\mathrm{min}} &= \max[0, \delta + (1-\lambda)/2], \\ x_{\mathrm{max}} &= \min[1, \delta + (1+\lambda)/2] \end{aligned} \tag{6.19}$$

ensure that the integral extends only on the overlap regions of the dot and vibron. As one appreciates from Eqs. (6.15)-(6.18), for a fixed L_{d} the electron-vibron Hamiltonian is completely determined by the relative position of the centres of the dot and the vibron $\delta = (x_{\mathrm{v}} - x_{\mathrm{d}})/L_{\mathrm{d}}$, and the ratio between the length of the vibron and of the dot $\lambda = L_{\mathrm{v}}/L_{\mathrm{d}}$.
Importantly, $\hat{H}_{\text{e-v}}$ reveals that the electron-vibron interaction only involves the position operator $\hat{x}_m$ of the m-vibron mode, the position operator $\hat{X}_n$ of the nth charged plasmon mode and the total electron number $\hat{N}_{c+}$. Moreover, the important energy scales involved in the electron-vibron dynamics are the lowest vibron energy $\hbar\omega$, the lowest charged plasmon energy ε_0/g_{c+} and the fundamental coupling constant I: their values are 0.050 meV, 8.293 meV and 0.088 meV, respectively, for a (10,10) SWCNT with $L_{\mathrm{d}} = L_{\mathrm{v}} = 1$ μm and the other parameters as the ones given in Fig. 6.4. Excluding the extreme short vibron regime $\lambda \leq 1/100$ and the strong screening, we can conclude that $\hbar\omega, I \ll \varepsilon_0/g_{c+}$, thus implying a clear separation of the vibron and plasmon energy scales. Albeit these two degrees of freedom are consequently characterized, for an isolated system, by an essentially independent dynamics, the tunneling event can be substantially influenced by the mechanical motion of the nanotube under certain geometrical conditions as will be discussed later.

6.2 Coupling mechanisms in suspended SWCNTs

In the above section, we analyzed that in suspended SWCNTs, the coupling mechanism is not so simple as predicted by AH model and the effects of density fluctuations can

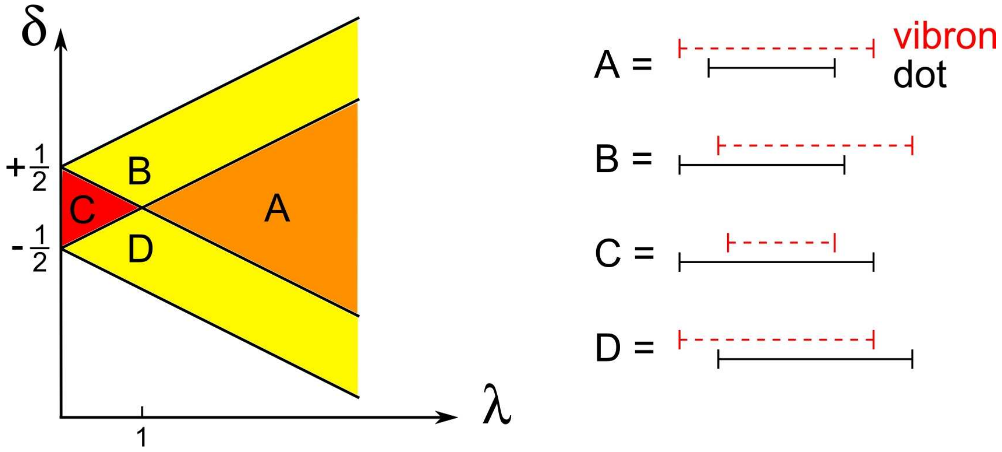

Figure 6.2: Parameters space of the geometrical configurations of the electromechanical nanojunction. The relevant dimensionless parameters are the length ratio $\lambda = L_\mathrm{v}/L_\mathrm{d}$ and the relative position of the centres $\delta = (x_\mathrm{v} - x_\mathrm{d})/L_\mathrm{d}$. Four qualitatively different regions are identified in the parameters space and schematically shown on the right.

play a crucial role. Hence, in the following sections, we analyze the two coupling mechanisms, plasmon-vibron and charge-vibron couplings, in suspended SWCNTs in some detail. The energy spectrum and the Franck-Condon couplings strongly depend on the geometry of the junction via the coupling constants K_{nm} and L_m. The detailed analysis of these coupling constants is thus the natural starting point to understand the presence of geometrical-dependent trends and selection rules in the tunneling processes of a suspended SWCNT. The geometrical parameters space $\{\lambda, \delta\}$ is divided into four regions by the different conditions imposed by the integration limits x_min and x_max explicitly given in Eq. (6.19). In Fig. 6.2, we define these regions and give a schematic representation of the corresponding geometrical configuration.

6.2.1 Plasmon-vibron couplings

The first line of the electron-vibron Hamiltonian Eq. (6.15) describes the plasmon-vibron interaction. The plasmon-vibron couplings are parameterized by the dimensionless matrix K_{nm}. The function K_{nm} has the following explicit form in the four regions:

$$
\begin{aligned}
K_{nm}^{(A)}(\lambda,\delta) &= -\frac{2m}{\pi(\lambda^2 n^2 - m^2)}\left[(-1)^n \sin\left(m\pi\frac{1-2\delta+\lambda}{2\lambda}\right) + \sin\left(m\pi\frac{1+2\delta-\lambda}{2\lambda}\right)\right],\\
K_{nm}^{(B)}(\lambda,\delta) &= -\frac{2}{\pi(\lambda^2 n^2 - m^2)}\left[(-1)^n m \sin\left(m\pi\frac{1-2\delta+\lambda}{2\lambda}\right) + \lambda n \sin\left(\lambda n\pi\frac{1+2\delta-\lambda}{2\lambda}\right)\right],\\
K_{nm}^{(C)}(\lambda,\delta) &= \frac{2\lambda n}{\pi(\lambda^2 n^2 - m^2)}\left[(-1)^m \sin\left(\lambda n\pi\frac{\lambda+2\delta+1}{2\lambda}\right) + \sin\left(\lambda n\pi\frac{\lambda-2\delta-1}{2\lambda}\right)\right],\\
K_{nm}^{(D)}(\lambda,\delta) &= \frac{2}{\pi(\lambda^2 n^2 - m^2)}\left[(-1)^m \lambda n \sin\left(\lambda n\pi\frac{\lambda+2\delta+1}{2\lambda}\right) + m \sin\left(m\pi\frac{\lambda-2\delta-1}{2\lambda}\right)\right].
\end{aligned}
\tag{6.20}
$$

Some symmetry relations for the function K_{nm} can be readily obtained from Eq. (6.20):

$$\begin{aligned} K_{nm}(\lambda,\delta) &= 1/\lambda\, K_{mn}(1/\lambda,-\delta/\lambda),\\ K_{nm}(\lambda,\delta) &= (-1)^{n+m}K_{nm}(\lambda,-\delta). \end{aligned} \tag{6.21}$$

The first equation in Eq. (6.21) quantifies the connection between the behaviour of $K_{nm}(\lambda,\delta)$ at small and large values of λ: the roles of the vibron and of the plasmon are simply exchanged in the plasmon-vibron Hamiltonian if we invert the ratio of their lengths. The second equation in Eq. (6.21) states instead that if we invert the relative position of the vibron and the dot, the plasmon-vibron Hamiltonian acquires at most a minus sign, depending on the parity of the vibronic and plasmonic modes. The case considered in [93] corresponds to the point $\lambda = 1$, $\delta = 0$ of the parameters space where the following limit holds:

$$\lim_{\lambda\to 1} K_{nm}(\lambda,0) = \delta_{nm}, \tag{6.22}$$

and each vibronic mode is only coupled to the plasmonic mode of the same order $n = m$. In *all* other regions of the parameters space, the coupling is not diagonal and the dynamics of each vibronic mode is influenced by all plasmonic modes and vice versa, making the system quite intricate. Nevertheless, from a detailed analysis of the K function, one can estimate which modes are more relevant in the low-energy limit. The function K has an upper bound $K < 2$, as can be easily proven from its definition Eq. (6.17) by considering that the distance between the integration limits is at maximum λ. Thus, K_{nm} does not diverge for $\lambda \to m/n$ as one could expect from a first sight. Instead, its maximum can be estimated by calculating the limit $\lambda \to m/n$. One obtains

$$\lim_{\lambda\to\frac{m}{n}} K_{mn}(\lambda,\delta) = \begin{cases} \frac{n}{m}\cos\left[\frac{\pi}{2}(n-m+2n\delta)\right], & \text{for} \quad n<m,\\ \cos\left[\frac{\pi}{2}(n-m+2n\delta)\right], & \text{for} \quad n>m, \end{cases} \tag{6.23}$$

where the first and the second case are calculated in regions A and C, respectively, see Fig. 6.2. The absolute value $|K_{nm}|$ of the coupling exhibits $|m-n|+1$ local maxima as a function of the relative displacement δ, separated by nodes in which the mth vibronic mode is decoupled from the nth plasmonic one. Note that in the limit $\lambda \to m/n$, the wavelength of the mth vibronic mode coincides with that of the nth plasmonic one, thus giving a physical interpretation to the resonance. One concludes that each geometrical configuration optimizes the coupling between specific plasmonic and vibronic modes. Moreover, the coupling between low vibronic modes and higher plasmonic ones is reached for short vibrons and is more efficient than the coupling of a low plasmonic mode with higher vibronic ones obtained, instead, for large vibrons. Another interesting regime can be reached in the small vibron region when the centre of the vibron lies in the vicinity of the border of the dot. Let us consider for this reason the function K_{nm} in the region B and with $\lambda \ll m/n$. The following relation holds:

$$K_{nm}\left(\lambda,\frac{1}{2}+\alpha\lambda\right) = \frac{2}{\pi m}(-1)^n \sin\left[m\pi\left(\frac{1}{2}-\alpha\right)\right], \tag{6.24}$$

where $|\alpha| < 1/2$. The absolute value $|K_{nm}|$ of the coupling exhibits m local maxima as a function of α in the region B which are independent of the plasmonic mode

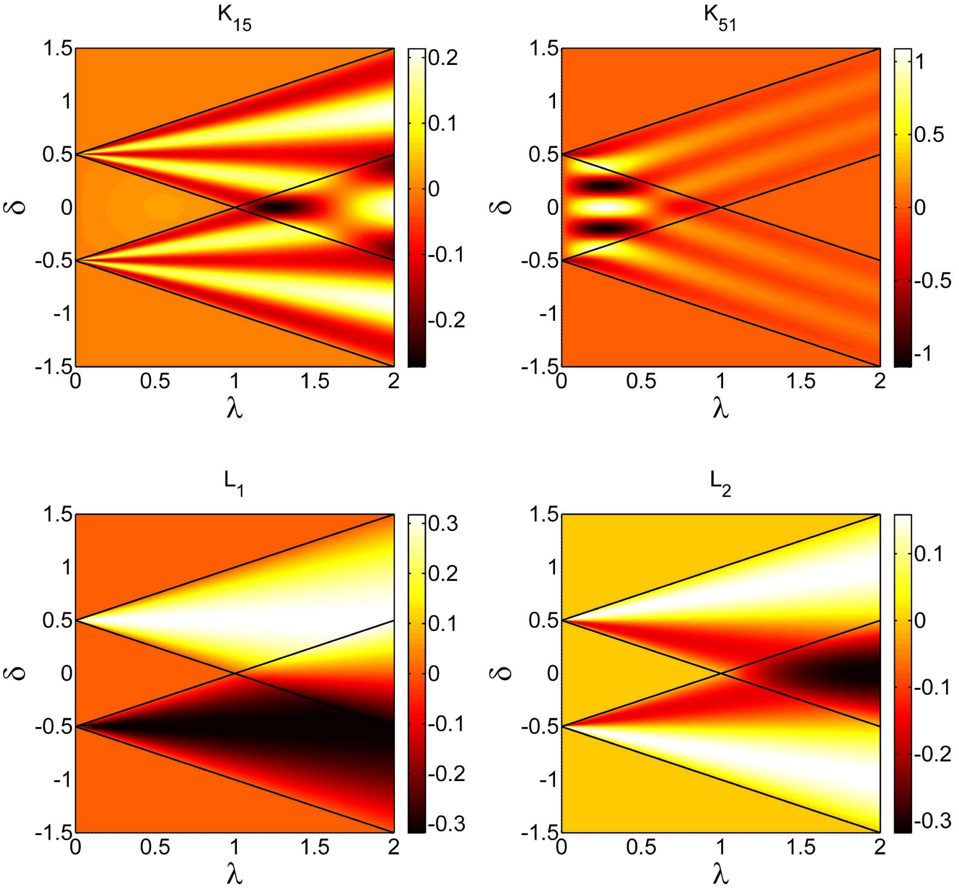

Figure 6.3: The plasmon-vibron K_{nm} and the charge-vibron L_m coupling constants are plotted in the geometrical parameters space. Top row: On the left (right) the coupling between the first (fifth) plasmonic and the fifth (first) vibronic modes. Bottom row: Examples of the charge-vibron coupling L_m are given for the first (left) and the second (right) vibronic mode. Black solid lines indicate in all figures the borders of the regions A, B, C, D indicated in Fig. 6.2 and explained in the text.

n. This specific configuration has been chosen in [89] to describe a system in which the renormalization of the lowest vibronic mode due to the coupling to the plasmons produces a strongly inhomogeneous Franck Condon coupling in the tunneling matrix elements to the carbon nanotube. In order to illustrate the arguments presented so far, we plot in Fig. 6.3 the plasmon-vibron couplings K_{15} and K_{51} as a function of λ and δ. Clearly visible are the maxima of the coupling close to $\lambda = m/n$ and the fan-shape structure of the coupling close to the points $\{0, \pm 1/2\}$, more visible in the case K_{15} due to the conditions given above.

6.2.2 Charge-vibron couplings

The second line of the electron-vibron Hamiltonian Eq. (6.15) describes the charge-vibron interaction and is proportional to the function L_m defined in Eq. (6.18). Also the coupling L_m is defined on the parameters space $\{\lambda, \delta\}$ by different functions in the four different regions already introduced for K_{nm}:

$$\begin{aligned}
L_m^{(A)}(\lambda,\delta) &= \frac{1}{m\pi}\left[\sin\left(m\pi\frac{1-2\delta+\lambda}{2\lambda}\right)+\sin\left(m\pi\frac{1+2\delta-\lambda}{2\lambda}\right)\right],\\
L_m^{(B)}(\lambda,\delta) &= \frac{1}{m\pi}\sin\left(m\pi\frac{1-2\delta+\lambda}{2\lambda}\right),\\
L_m^{(C)}(\lambda,\delta) &= 0,\\
L_m^{(D)}(\lambda,\delta) &= \frac{1}{m\pi}\sin\left(m\pi\frac{1+2\delta-\lambda}{2\lambda}\right).
\end{aligned} \tag{6.25}$$

A symmetry relation can also be derived for this coupling, namely

$$L_m(\lambda,\delta) = (-1)^m L_m(\lambda,-\delta). \tag{6.26}$$

The function L_m vanishes identically in the region C, thus implying no charge-vibron coupling for systems in which the vibron is entirely contained inside the dot. The finite local coupling is in fact averaged away by the sinusoidal shape of the vibron. The form of L_m in the region B is readily understood with the parametrization:

$$L_m\left(\lambda, \pm\frac{1}{2}+\alpha\lambda\right) = \frac{1}{m\pi}\sin\left[m\pi\left(\frac{1}{2}-\alpha\right)\right] \tag{6.27}$$

with $|\alpha| \leq 1/2$. As shown in Fig. 6.3, $|L_m|$ has indeed in the small vibron limit a fan-shape with m maxima of magnitude $1/(m\pi)$ separated by $m-1$ nodes. Thus, the charge-vibron coupling decreases for higher vibron modes and is also very sensitive to the geometry of the system. The geometry of the system even introduces selection rules: for example, for a system with $\lambda = 0.1$ and $\delta = 1/2$, $(\alpha = 0)$ only odd modes $(m = 2a-1,\ a \in \mathbb{N}^+)$ exhibit charge-vibron coupling.

The maximum charge-vibron coupling for the mode m is reached when $|L_m| = 2/(m\pi)$ and is obtained only for vibrons larger than the dot (A region, $\lambda > 1$) and centered with respect to it ($\delta = 0$). Only even vibronic modes couple to the charge if $\delta = 0$ and $|L_m|$ exhibits $m/2$ maxima in the positions $\lambda = m/(1+2r)$ where $0 \leq r < (m-1)/2$, $r \in \mathbb{N}$.

In conclusion, the electron-vibron coupling is very sensitive to the geometry of the junction, both its plasmon-vibron and charge-vibron components. In general, for more symmetric systems ($\delta \approx 0$) the plasmon-vibron component dominates the short vibron limit ($\lambda < 1$, region C), whereas the large vibron limit ($\lambda > 1$, region A) is dominated by the charge-vibron interaction. Only for a strongly asymmetric system ($\delta \approx \pm 1/2$) in the short vibron limit ($\lambda \ll m/n$) can the two components have the same strength. Moreover, in general, the strength of the coupling decreases with the vibron mode.

Yet, the position of the nodes of the functions K_{nm} and L_m depends on the vibron and plasmon mode numbers n and m, generating selection rules that depend sensitively on the geometry of the system.

6.3 Diagonalization and spectrum

Because the electron-vibron coupling only involves the total charge operator $\hat{N}_{c+}$ and the plasmon excitations, the part of the system Hamiltonian that is still to be diagonalized is

$$\begin{aligned}\hat{H}'_{\mathrm{sys}} &= \sum_{n\geq 1} n\frac{\hbar\Omega}{2}\left(\hat{X}_n^2+\hat{P}_n^2\right)+\sum_{m\geq 1} m\frac{\hbar\omega}{2}\left(\hat{x}_m^2+\hat{p}_m^2\right)\\ &+I\sqrt{g_{c+}}\sum_{n,m\geq 1}\sqrt{nm}K_{nm}2\hat{X}_n\hat{x}_m+I\sum_m\sqrt{m}L_m\sqrt{2}\hat{N}_{c+}\hat{x}_m,\end{aligned} \tag{6.28}$$

where we have introduced the frequencies $\Omega = \pi v_{\mathrm{F}}/(g_{c+}L_{\mathrm{d}})$ and $\omega = \pi v_{\mathrm{st}}/L_{\mathrm{v}}$. The exact diagonalization of the Hamiltonian Eq. (6.28) can be achieved in two steps: (i) a set of canonical transformations eliminates the plasmon-vibron component; (ii) a polaron transformation eliminates the charge-vibron component. The final result is a collection of shifted plasmon-vibron oscillators.

The first step in the diagonalization is better understood by setting the plasmon-vibron part of the Hamiltonian into a quadratic form:

$$\hat{H}'_{\mathrm{sys}} = \begin{pmatrix}\hat{\mathbf{X}}\\ \hat{\mathbf{x}}\\ \hat{\mathbf{P}}\\ \hat{\mathbf{p}}\end{pmatrix}^{\mathrm{T}}\begin{pmatrix}H_{\mathrm{pp}} & H_{\mathrm{pv}} & 0 & 0\\ H_{\mathrm{vp}} & H_{\mathrm{vv}} & 0 & 0\\ 0 & 0 & H_{\mathrm{pp}} & 0\\ 0 & 0 & 0 & H_{\mathrm{vv}}\end{pmatrix}\begin{pmatrix}\hat{\mathbf{X}}\\ \hat{\mathbf{x}}\\ \hat{\mathbf{P}}\\ \hat{\mathbf{p}}\end{pmatrix}+\hat{H}_{\mathrm{cv}}, \tag{6.29}$$

where the components of matrix H_{M} defining the quadratic form are given by: $(H_{\mathrm{pp}})_{nn'} = n\hbar\Omega/2\,\delta_{nn'}$, $(H_{\mathrm{vv}})_{mm'} = m\hbar\omega/2\,\delta_{mm'}$ and $(H_{\mathrm{pv}})_{nm} = (H_{\mathrm{vp}})_{mn} = I\sqrt{g_{c+}}\sqrt{nm}K_{nm}$. Moreover, we have introduced the vector of operators $\hat{\mathbf{X}} = [\hat{X}_1, \hat{X}_2, \ldots]^{\mathrm{T}}$ and analogously for $\hat{\mathbf{x}}$, $\hat{\mathbf{P}}$, and $\hat{\mathbf{p}}$. Finally, we have defined the charge-vibron Hamiltonian $\hat{H}_{\mathrm{cv}}$. The quadratic form in Eq. (6.29) is simplified via the following set of canonical transformations: the first is the contraction

$$\begin{aligned}\hat{X}'_n &= 1/\sqrt{n\hbar\Omega}\,\hat{X}_n, & \hat{x}'_m &= 1/\sqrt{m\hbar\omega}\,\hat{x}_m,\\ \hat{P}'_n &= \sqrt{n\hbar\Omega}\,\hat{P}_n, & \hat{p}'_m &= \sqrt{m\hbar\omega}\,\hat{p}_m,\end{aligned} \tag{6.30}$$

that transforms the momentum block of H_{M} into the matrix $\mathbf{1}/2$. Note that the commutation relations between position and momentum operators are conserved for each mode: $[\hat{X}'_n, \hat{P}'_{n'}] = \mathrm{i}\delta_{nn'}$ and $[\hat{x}'_n, \hat{p}'_{n'}] = \mathrm{i}\delta_{nn'}$. Afterwards we perform the rotation

$$\begin{aligned}\hat{\xi}'_l &= \sum_{n=1}^{N_{\mathrm{p}}} U^{\mathrm{T}}_{ln}\,\hat{X}'_n+\sum_{m=1}^{N_{\mathrm{v}}} U^{\mathrm{T}}_{lN_{\mathrm{p}}+m}\,\hat{x}'_m,\\ \hat{\pi}'_l &= \sum_{n=1}^{N_{\mathrm{p}}} U^{\mathrm{T}}_{ln}\,\hat{P}'_n+\sum_{m=1}^{N_{\mathrm{v}}} U^{\mathrm{T}}_{lN_{\mathrm{p}}+m}\,\hat{p}'_m\end{aligned} \tag{6.31}$$

that diagonalizes the position block of H_{M} written in the primed variables. We have also introduced the total number of vibron (plasmon) modes N_{v} (N_{p}). This can be done without loss of generality due to the presence of physical cut-offs for both the plasmonic and the vibronic mode numbers. This transformation is physically most important since it generates the position and momentim operators $\hat{\xi}'_l$ and $\hat{\pi}'_l$ which identify $N_\mathrm{p} + N_\mathrm{v}$ mixed plasmon-vibron modes. The matrix defining the quadratic form reads, in this mixed basis,

$$H_\mathrm{M} = \left(\begin{array}{c|c} \boldsymbol{\Delta} & 0 \\ \hline 0 & \mathbf{1}/2 \end{array}\right) \tag{6.32}$$

where $\boldsymbol{\Delta}$ is a diagonal matrix whose diagonal element Δ_l defines the energy of the plasmon-vibron mode $\hbar\omega_l = \sqrt{2\Delta_l}$. This relation becomes clear after the last canonical transformation, the expansion

$$\begin{aligned} \hat{\xi}_l &= \sqrt{\hbar\omega_l}\,\hat{\xi}'_l, \\ \hat{\pi}_l &= 1/\sqrt{\hbar\omega_l}\,\hat{\pi}'_l \end{aligned} \tag{6.33}$$

that brings the system Hamiltonian into the form

$$\hat{H}'_\mathrm{sys} = \sum_l \frac{\hbar\omega_l}{2}(\hat{\xi}_l^2 + \hat{\pi}_l^2) + H_\mathrm{cv}. \tag{6.34}$$

The effect of the transformations Eq. (6.30), Eq. (6.31) and Eq. (6.33) on the charge-vibron Hamiltonian $\hat{H}_\mathrm{cv}$ is readily obtained:

$$\hat{H}_\mathrm{cv} = I\sqrt{2}\sum_{lm} mL_m\sqrt{\frac{\omega}{\omega_l}}U_{N_\mathrm{p}+m,\,l}\,\hat{\xi}_l\hat{N}_{c+}. \tag{6.35}$$

The presence of $\hat{H}_\mathrm{cv}$ requires a second step in the diagonalization procedure: the polaron transformation $\hat{\hat{H}}'_\mathrm{sys} = \mathrm{e}^{-\hat{S}}\hat{H}'_\mathrm{sys}\mathrm{e}^{+\hat{S}}$, where

$$\hat{S} = \mathrm{i}\sqrt{2}\sum_{lm}\frac{I}{\hbar\omega_l}mL_m\sqrt{\frac{\omega}{\omega_l}}U_{N_\mathrm{p}+m,\,l}\,\hat{\pi}_l\hat{N}_{c+}, \tag{6.36}$$

yielding

$$\hat{\hat{H}}'_\mathrm{sys} = \sum_l \frac{\hbar\omega_l}{2}(\hat{\xi}_l^2 + \hat{\pi}_l^2) - \sum_l \frac{I^2}{\hbar\omega_l}\left(\sum_m L_m\sqrt{\frac{\omega}{\omega_l}}U_{N\,\mathrm{p}+m,\,l}\right)^2 \hat{N}_{c+}^2. \tag{6.37}$$

Thus, the low energy spectrum of the suspended SWCNT reads

$$E_{\vec{N},\vec{m}} = E_{\vec{N}} + \sum_l \hbar\omega_l\left(m_l + \frac{1}{2}\right) + \sum_{n,j\neq c+} n\varepsilon_0 m_{n,j}, \tag{6.38}$$

where $\vec{N} = [N_{c+}, N_{c-}, N_{s+}, N_{s-}]$ is the vector defining the electronic configuration and $E_{\vec{N}}$ the associated energy as can be computed from Eq. (6.5) and Eq. (6.37). The vector $\vec{m}$, instead, contains the occupation numbers m_l of the plasmon-vibron modes and those ($m_{n,j}$, $j \neq c+$) of the other relative charge and spin bosonic modes.

The diagonalization procedure presented here reproduces known results in some limiting cases. In the totally symmetric case ($\delta = 0$, $\lambda = 1$) where the length and centre of the dot and vibrons coincide, only the coupling between plasmons and vibrons with the same number of modes is allowed ($K_{nm} = \delta_{nm}$). One finds that the matrix to be diagonalized by the rotation Eq. (6.31) is

$$n^2 \begin{pmatrix} \frac{\hbar^2\Omega^2}{2} & I\hbar\sqrt{\omega\Omega g_{c+}} \\ I\hbar\sqrt{\omega\Omega g_{c+}} & \frac{\hbar^2\omega^2}{2} \end{pmatrix}, \tag{6.39}$$

yielding the spectrum [93]

$$\hbar\omega_l = \sqrt{2\Delta_l} = n\hbar\sqrt{\frac{\Omega^2+\omega^2}{2} \pm \sqrt{\left(\frac{\Omega^2-\omega^2}{2}\right)^2 + \frac{4g_{c+}I^2\omega\Omega}{\hbar^2}}} \tag{6.40}$$

where $l = \{n, \alpha\}$ and $\alpha = \pm$. For this symmetric configuration, there is also no polaron shift since the charge-vibron coupling vanishes identically ($L_m = 0$). Also the case considered in [89] of a single vibron mode is reproduced by our general theory. Under the only assumption that $\omega \ll \Omega$, one obtains

$$\omega_1 = \omega\sqrt{1 - \frac{4I^2 g_{c+}}{\hbar^2\omega\Omega}\sum_{n=1}^{\infty} K_{n1}^2} \tag{6.41}$$

which is always real for the parameters considered in the present work. Moreover, the case of short asymmetric vibrons ($\lambda \ll 1, \delta = 1/2$) is particularly interesting since by means of Eq. (6.24) one obtains also that the lowest plasmons ($n \ll 1/\lambda$) equally contribute to soften the frequency of the lowest vibron mode.

In the generic case, however, only a numerical evaluation of the spectrum is viable. In Fig. 6.4, we present the relative frequency shift (*i.e.* $(\omega_m - m\omega)/m\omega$) for the first (left panel) and the fifth (right panel) plasmon-vibron mode. The calculation is performed for a $(10, 10)$ armchair nanotube of $L_\mathrm{d} = 1$ μm. The coupling of the vibrons to the plasmons softens the vibronic modes, yielding a negative shift for every configuration. The renormalization is stronger and almost constant in the region C, where the coupling between the low vibronic modes and the plasmonic ones is larger. An estimate of the maximum renormalization can be obtained by its direct calculation in the symmetric point ($\lambda = 1$, $\delta = 0$):

$$\frac{\omega_m - m\omega}{m\omega} \approx -\frac{2g_{c+}I^2}{\hbar^2\omega\Omega}, \tag{6.42}$$

where we made the expansion of Eq. (6.40) in powers of ω/Ω and $I/(\hbar\Omega)$. Interestingly, as far as the bare vibron frequency ω and the fundamental electron-vibron coupling constant $I/\hbar$ are both much smaller than the bare plasmon frequency Ω, the relative frequency normalization, if present, is independent of the mode number m. It is also clear that, in the absence of strong screening, ($g_{c+} \approx 0.2$) the relative normalization is very moderate and does not exceed 1%, independently of the geometry of the junction.

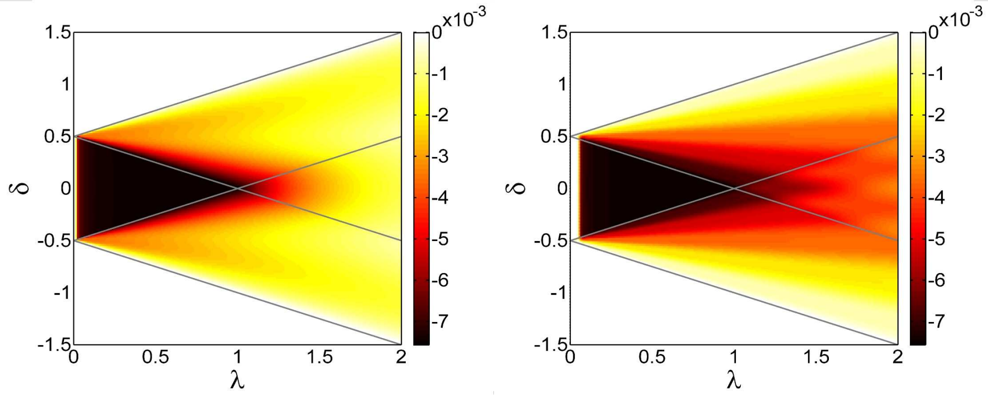

Figure 6.4: Relative normalization of the first (left) and the fifth (right) vibron mode due to the plasmon-vibron coupling. Note that the relative normalization is always negative; it reaches its maximum in the point $\lambda = 1$, $\delta = 0$ and is essentially constant in the entire region C (defined in Fig. 6.2). The parameters used are $L_{\mathrm{d}} = 1\,\mu\mathrm{m}$, $R = 6.68\,\text{Å}$, $v_{\mathrm{F}} = 8 \times 10^5\,\mathrm{m/s}$, $v_{\mathrm{st}} = 2.4 \times 10^4\,\mathrm{m/s}$, $M = 3.8 \times 10^{-7}\,\mathrm{kg/m^2}$, $g = 30\,\mathrm{eV}$, $g_{c+} = 0.2$.

6.4 Tunneling amplitudes and Franck-Condon couplings

So far we studied the isolated nanotube. Our interest, however, is the transport of electrons through a SWCNT in tunneling coupling with possibly extended source and drain leads, see Fig. 6.1. The tunneling Hamiltonian $\hat{H}_{\mathrm{T}}$ is given by:

$$\hat{H}_{\mathrm{T}} = \sum_{\alpha=\mathrm{s,d}} \sum_{\sigma} \int \mathrm{d}\vec{r} \left[T_{\alpha}\left(\vec{r}\right) \hat{\Psi}_{\sigma}^{\dagger}\left(\vec{r}\right) \hat{\Phi}_{\sigma\alpha}\left(\vec{r}\right) + \mathrm{H.c.} \right], \tag{6.43}$$

where $\hat{\Psi}_{\sigma}^{\dagger}$, see Eq. (5.20), and $\hat{\Phi}_{\sigma\alpha}^{\dagger}\left(\vec{r}\right) = \sum_{\vec{q}} \phi_{\vec{q}}^{*}\left(\vec{r}\right) \hat{c}_{\vec{q}\sigma\alpha}^{\dagger}$ are electron creation operators in the SWCNT and in the lead α, respectively, and $T_{\alpha}\left(\vec{r}\right)$ describes the transparency of the tunneling contact α.

The spatial dependence of the transparency $T_{\alpha}\left(\vec{r}\right)$ depends on the specific geometrical configuration of the junction and on the tube-lead hybridization. For the sake of simplicity, we refer again to the configurations introduced in Fig. 6.1. In both the A and A$'$ cases we expect $T_{\alpha}\left(\vec{r}\right)$ to be strongly localized at the interface between the extended lead and the dot, while in the case C the tunneling region extends over the entire fraction of the tube, which is covered by the leads. For the case B, an intermediate situation is envisaged with an extended tunneling region (weak hybridization) at the source and a localized one at the drain (strong hybridization).

In the weak tunneling limit, the dynamic of the system can be described as a series of sequential tunneling events connecting different many-body eigenstates of the system. For this reason, a central role is played in the theory by the spectrum that we calculated in the previous section and by the tunneling amplitudes between the corresponding many-body energy eigenstates, which is the focus of the present one.

Following [116], the 3D electron annihilator in the quantum dot $\hat{\Psi}_{\sigma}(\vec{r})$ can be expressed in terms of the slow varying 1D operators $\hat{\psi}_{rF\sigma}(x)$ which, in their bosonized form, read:

$$\hat{\psi}_{rF\sigma}(x) = \hat{\eta}_{r\sigma}\hat{K}_{rF\sigma}(x)\mathrm{e}^{\mathrm{i}\hat{\phi}^{\dagger}_{rF\sigma}(x)}\mathrm{e}^{\mathrm{i}\hat{\phi}_{rF\sigma}(x)} \tag{6.44}$$

where $\hat{\eta}_{r\sigma}$ is the Klein factor which reduces by one the occupation of the branch $r\sigma$, $\hat{K}_{rF\sigma}(x)$ is the operator

$$\hat{K}_{rF\sigma}(x) = \frac{1}{\sqrt{2L_{\mathrm{d}}}}\mathrm{e}^{\mathrm{i}(\pi/L_{\mathrm{d}})\mathrm{sgn}(F)(r\hat{N}_{r\sigma}+\Delta)x}, \tag{6.45}$$

which essentially adds a phase proportional to the occupation number of the branch $r\sigma$, and $\hat{\phi}_{rF\sigma}(x)$ is the bosonic field associated with the bosonic excitation of the SWCNT. It is useful to express $\hat{\psi}_{rF\sigma}(x)$ in terms of the position and momentum operators of the plasmonic modes $\hat{X}_n$ and $\hat{P}_n$. After a lengthy but straightforward calculation, one obtains

$$\hat{\psi}_{rF\sigma}(x) \propto \hat{\eta}_{r\sigma}\hat{K}_{rF\sigma}(x)\prod_{n\geq 1}\mathrm{e}^{+\mathrm{i}P_n(x)\hat{X}_n-\mathrm{i}X_n(x)\hat{P}_n} \tag{6.46}$$

where we have introduced the functions

$$\begin{aligned} X_n(x) &= \sqrt{\frac{2}{ng_{c+}}}\cos\left[\frac{n\pi}{L_{\mathrm{d}}}\left(x - x_{\mathrm{d}} + \frac{L_{\mathrm{d}}}{2}\right)\right], \\ P_n(x) &= \sqrt{\frac{2g_{c+}}{n}}\mathrm{sgn}(Fr)\sin\left[\frac{n\pi}{L_{\mathrm{d}}}\left(x - x_{\mathrm{d}} + \frac{L_{\mathrm{d}}}{2}\right)\right] \end{aligned} \tag{6.47}$$

and the proportionality in Eq. (6.46) is due to the frozen $c-$, $s+$ and $s-$ branches. They only contribute in fact with an overall constant to the tunneling matrix elements between the low energy eigenstates.

An explicit representation of these low energy eigenstates is readily obtained from Eqs. (6.5) and (6.37). Due to the already mentioned energy scale separation between on one side the vibronic and on the other side the plasmonic and electronic excitations, we can restrict ourselves, without loss of generality, to the case $m_{n,j} = 0, j \neq c+$ and obtain

$$|\vec{N}, \vec{m}\rangle = \mathrm{e}^{\hat{S}}|\vec{N}, \vec{m}\rangle_0, \tag{6.48}$$

where

$$|\vec{N}, \vec{m}\rangle_0 = \prod_l \frac{(\hat{\xi}_l - \mathrm{i}\hat{\pi}_l)^{m_l}}{\sqrt{2m_l!}}|\vec{N}, 0\rangle_0 \tag{6.49}$$

with $\vec{N} = [N_{c+}, N_{c-}, N_{s+}, N_{s-}]$ being the vector defining the electronic configuration and $\vec{m}$ representing here the occupation numbers of only the lowest vibron-plasmon modes (with an excitation energy lower that ε_0). The low energy eigenstates of a metallic suspended SWCNT are, thus, polaron shifted plasmon-vibron excitations over its electronic ground state $|\vec{N}, 0\rangle_0$. We are now ready to evaluate the matrix element:

$$\langle\vec{N}, \vec{m}|\hat{\psi}_{rF\sigma}(x)|\vec{N}', \vec{m}'\rangle = {}_0\langle\vec{N}, \vec{m}|\mathrm{e}^{-\hat{S}}\hat{\psi}_{rF\sigma}(x)\mathrm{e}^{+\hat{S}}|\vec{N}', \vec{m}'\rangle_0. \tag{6.50}$$

Since the operator $\hat{S}$ defined in Eq. (6.36) commutes with $\hat{K}_{rF\sigma}$:

$$\mathrm{e}^{-\hat{S}}\hat{\psi}_{rF\sigma}(x)\mathrm{e}^{+\hat{S}} \propto \hat{\eta}_{r\sigma}\hat{K}_{rF\sigma}\prod_l \mathrm{e}^{+\mathrm{i}\pi_l(x)\hat{\xi}_l-\mathrm{i}\xi_l(x)\hat{\pi}_l}, \tag{6.51}$$

where the proportionality accounts for the constant terms deriving by the application of the Baker-Hausdorff theorem and we defined the functions:

$$\begin{aligned}\xi_l(x) =& -\frac{\sqrt{2}I}{\varepsilon_l}\sum_{m=1}^{N_\mathrm{v}}\sqrt{\frac{\hbar\omega}{\varepsilon_l}}mL_mU_{N_\mathrm{p}+m,\,l}\\ &+\sum_{n=1}^{N_\mathrm{p}}\sqrt{\frac{2\varepsilon_l}{n^2g_{c+}\hbar\Omega}}U_{nl}\cos\left[\frac{n\pi}{L_\mathrm{d}}\left(x-x_\mathrm{d}+\frac{L_\mathrm{d}}{2}\right)\right],\\ \pi_l(x) =& \sum_{n=1}^{N_\mathrm{p}}\sqrt{\frac{2g_{c+}\hbar\Omega}{\varepsilon_l}}U_{nl}\sin\left[\frac{n\pi}{L_\mathrm{d}}\left(x-x_\mathrm{d}+\frac{L_\mathrm{d}}{2}\right)\right].\end{aligned} \tag{6.52}$$

By means of Eq. (6.51) it is now clear that the tunneling matrix element factorizes into an electronic component and a product of Franck-Condon factors, one for each plasmon-vibron mode:

$$\langle\vec{N},\vec{m}|\hat{\psi}_{rF\sigma}(x)|\vec{N}',\vec{m}'\rangle \propto \langle\vec{N}|\hat{\eta}_{r\sigma}\hat{K}_{rF\sigma}|\vec{N}'\rangle\prod_l F(m_l,m_l',\lambda_l) \tag{6.53}$$

where

$$\lambda_l = -\frac{\xi_l-\mathrm{i}\pi_l}{\sqrt{2}} \tag{6.54}$$

is the effective coupling between the charge and the plasmon-vibron mode and

$$\begin{aligned}F(m,m',\lambda) =& \left[\theta(m'-m)\lambda^{m'-m}+\theta(m-m')(-\lambda^*)^{m-m'}\right]\\ &\times\sqrt{\frac{m_\mathrm{min}!}{m_\mathrm{max}!}}\sum_{i=0}^{m_\mathrm{min}}\frac{(-|\lambda|^2)^i}{i!(i+m_\mathrm{max}-m_\mathrm{min})!}\frac{m_\mathrm{max}!}{(m_\mathrm{min}-i)!}\end{aligned} \tag{6.55}$$

is the explicit expression of the Franck-Condon factor. Eqs. (6.52)-(6.55) together with Eq. (6.31) for the definition of the transformation U represent the main analytical result of this work. They are a very general expression of the tunneling matrix elements between the low energy eigenstates of a suspended SWCNT in the presence of multiple plasmon and vibron modes. Special limits of these formulae are already available in the literature [89, 93]. Particularly, interesting to our point of view is the contribution of the geometrical configuration of the junction, which determines selection rules in the tunneling processes and in turn the magnitude of the dimensionless electron-vibron Franck-Condon couplings λ_l. In Fig. 6.5, we present $|\lambda_l|$ for the first (left) and the second (right) plasmon-vibron modes.

The values in the figure correspond to a tunneling matrix element calculated at the beginning of the tube ($x = x_\mathrm{d} - L_\mathrm{d}/2$). By a comparison with the corresponding

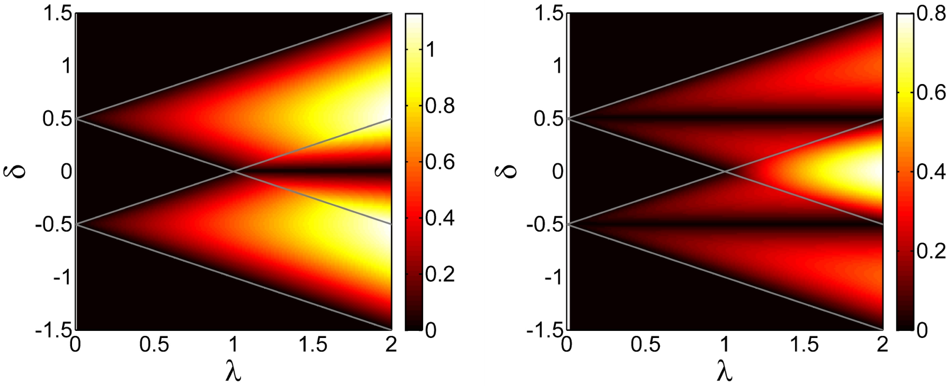

Figure 6.5: The Franck-Condon couplings $|\lambda_l|$ as a function of the length ratio $\lambda = L_\mathrm{v}/L_\mathrm{d}$ and relative centre position $\delta = (x_\mathrm{v} - x_\mathrm{d})/L_\mathrm{d}$. The coupling for the first and second vibron-plasmon modes are shown in the left and right panel, respectively. The parameters are the same as those reported in Fig. 6.4. The couplings are calculated for a tunneling event at the beginning of the dot.

charge-vibron coupling constant L_m in the lower panels of Fig. 6.3, one can argue that $|\lambda_m| \propto |L_m|$. This observation is essentially correct, at least in the A, B and D regions of the parameters space where the energy renormalization of the vibronic modes is negligible and the same holds for the mixing introduced in Eq. (6.31) between the vibronic and plasmonic modes. Consequently, we expect that $|\lambda_l|$ does not depend on the tunneling point, at least in the long vibron region ($\lambda > 1$) for any geometrical configuration. This result is illustrated in Fig. 6.6 where the Franck-Condon couplings for the first and second plasmon-vibron modes are plotted as a function of the dimensionless tunneling point ($\xi = x/L_\mathrm{d}$) and relative position of the vibron (δ) for the configuration $L_\mathrm{v}/L_\mathrm{d} = 2$. Interestingly, the selection rules derived in the previous section for L_m directly apply to the Franck-Condon couplings in the long vibron regime: for example, for a symmetric junction ($\delta \approx 0$) only even modes can be excited by a tunneling event, whereas the odd ones will remain in their ground state. Finally, it is also notable that $\max(|\lambda_l|) \approx 1$ in the long vibron regime even in the absence of strong screening ($g_{c+} \approx 0.2$).

A different result characterizes the short vibron limit ($\lambda < 1$). In the C region, the charge-vibron coupling vanishes identically due to symmetry considerations. Even if small, the vibron-plasmon mixing becomes there the dominant effect. In Fig. 6.7, we present the Franck-Condon coupling of the lowest vibron-plasmon mode for the configuration $\lambda = L_\mathrm{v}/L_\mathrm{d} = 0.1$. In particular, in the upper left panel we show $|\lambda_1|$ and in the remaining panels its components: i.e. in the upper right panel the charge-vibron component (the first line of ξ_l in Eq. (6.52)), in the lower left panel the plasmon-vibron component of ξ_l and π_l in the lower right panel. The dashed white lines represent in all panels the borders of the C region, i.e., the region in which the vibron is completely inside the dot. Outside the C region the charge-vibron coupling is stronger and λ_1 does not depend on the tunneling point. Inside the C region, instead, the dominant contribution is given (in the lower left panel) by the plasmon-vibron component of ξ_l. The latter follows the position of the vibron and mimics its shape. The last obser-

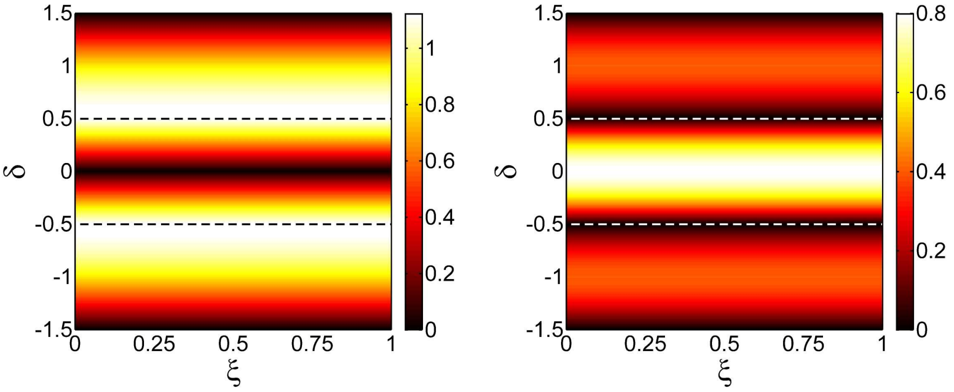

Figure 6.6: The Franck-Condon couplings of the first (left) and second (right) vibron-plasmon mode in the long vibron regime ($\lambda = 2$) plotted against the dimensionless tunneling point $\xi = x/L_\mathrm{d}$ and the relative position δ of the dot and vibron centres. Dashed lines indicate the borders between the B (top), A (center), and D (bottom) regions of the parameters space, see Fig. 6.2.

vation is also confirmed by the lower left panel of Fig. 6.8, where the corresponding component of the Franck-Condon coupling for the fifth mode is plotted. Finally, for higher modes in the short vibron limit, a position-dependent Franck-Condon coupling is still appreciable also in the B and D regions, see Fig. 6.8.

The relevance of these results for the tunneling Hamiltonian and the associated tunneling rates between the many-body eigenstates depends by their interplay with the spatially dependent transparency $T(\vec{r})$ introduced in the beginning of this section. In fact, we expect to detect a position-dependent Franck-Condon factor in the tunneling rates only for the cases illustrated in Figs. 1A, 1A′ and (B) where the vibron also extends beyond the dot region, but not for the case in Fig. 1(C). This observation, together with the results presented in Figs. 6.6-6.8, allows us to conclude that the position-dependent rates can be observed, among the configurations considered in this work, only in the asymmetric short vibron one ($\lambda \ll 1,\ \delta \approx \pm 1/2$), i.e. a configuration of type B (or D), also in agreement with the results presented in [89]. In a recent publication [139], an alternative setup has been proposed for the direct visualization of the position-dependent Franck-Condon couplings in which one of the two metallic electrodes is substituted by the tip of a scanning tunneling microscope.

In the absence of electron-vibron coupling, the frequency of the nth stretching mode is an nth multiple of the frequency ω of the fundamental mode. Hence, naturally, there are several energetic degenerate vibronic configurations (involving two or more modes) that may contribute to transport at finite bias. As we just proved, for realistic values of the parameters, the softening of the stretching modes introduced by the electron-vibron coupling does not really lift these degeneracies. This fact has profound implications for the transport properties of the system. Interference effects have been, in fact, predicted even for systems in the Coulomb blockade regime [72, 85, 91, 92] in the presence of quasi-degenerate states.

Technically, this degeneracy determines the method of choice for the description of the dynamics of the system. At low biases, such that only the lowest vibronic mode

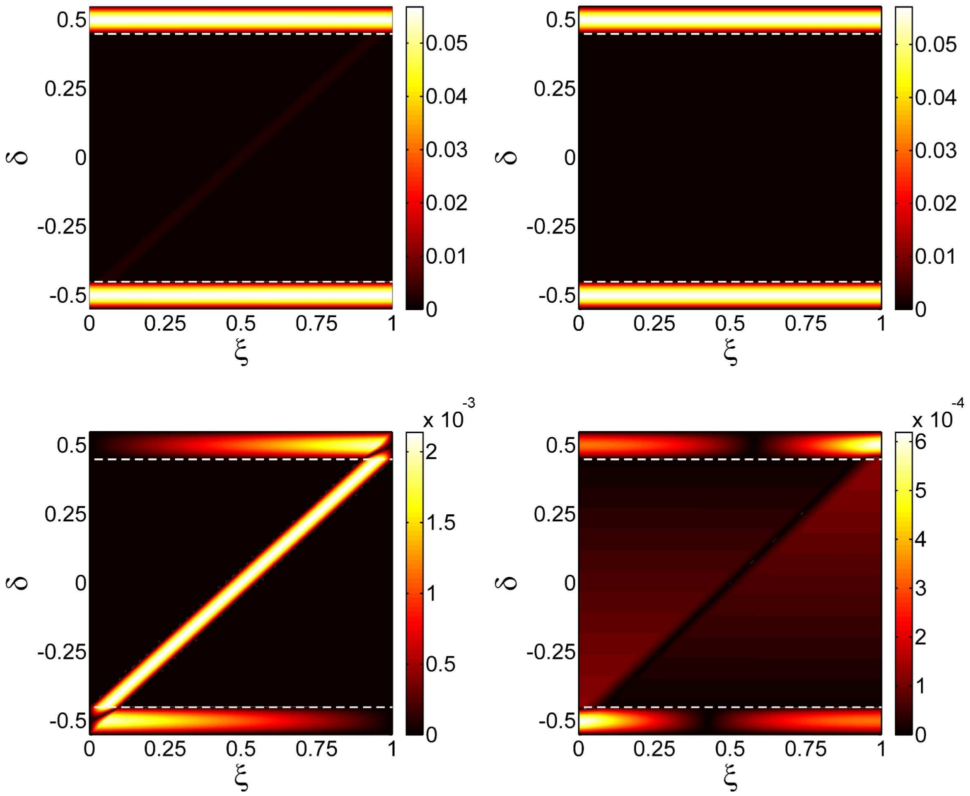

Figure 6.7: Position dependence of the Franck-Condon coupling of the first vibron-plasmon mode in the short vibron regime ($\lambda = 0.1$). In the upper left panel, the full coupling $|\lambda_1|$ is plotted, while in the remaining panels its different components are plotted: i.e. in the upper right panel, the charge-vibron component (the first line of ξ_l in Eq. (6.52)), in the lower left panel, the plasmon-vibron component of ξ_l and π_l in the lower right panel. The dashed white lines represent in all panels the borders of the C region, i.e., the region in which the vibron is completely inside the dot.

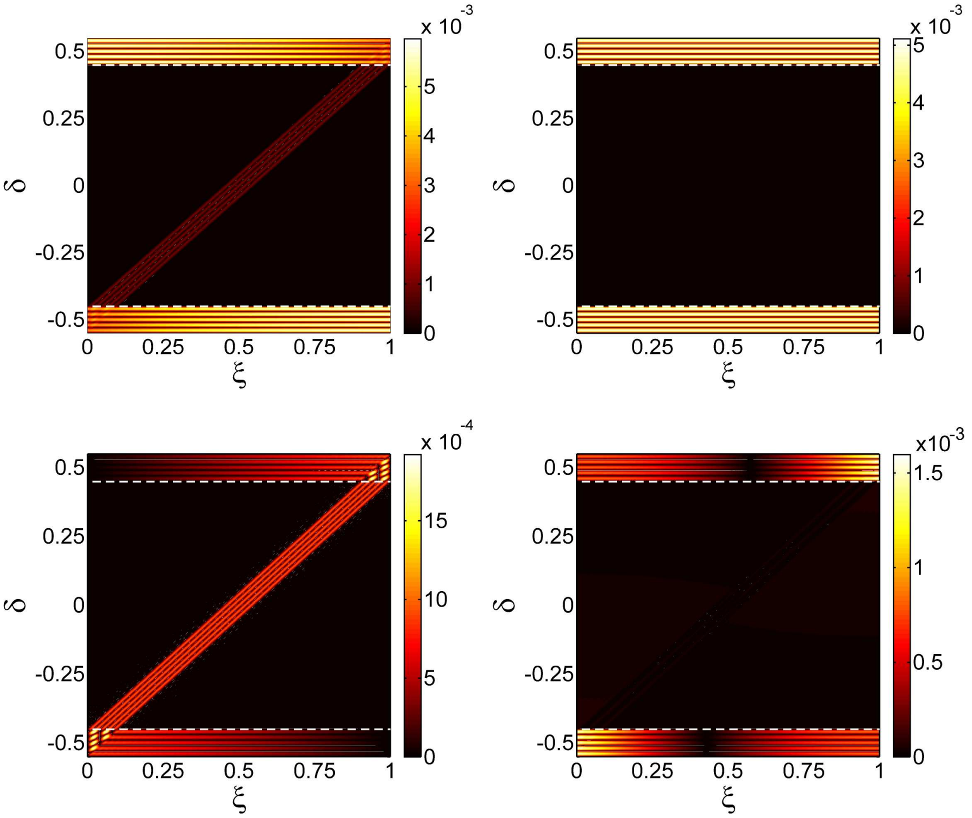

Figure 6.8: Position dependence of the Franck-Condon coupling of the fifth vibron-plasmon mode in the short vibron regime ($\lambda = 0.1$). In the upper left panel, the full coupling $|\lambda_5|$ is plotted. As in Fig. 6.7 the other panels represent its different components.

is excited, a description of the dynamics only in terms of rate equations involving occupation probabilities of the many-body states of the quantum dots is appropriate. However, at higher bias, when several vibron modes are excited, a generalized master equation (GME) coupling diagonal (populations) and off-diagonal (coherences) elements of the quantum dot reduced density matrix should be used, see e.g., [69, 70, 72, 75, 76, 79, 80, 85, 90, 91].

The sensitive dependence of the tunneling matrix elements on the mode number for a given geometry of the system also suggests the existence of symmetrically coupled slow channels such as the ones described in [83] and consequently of similar NDC effects in the stability diagrams of a suspended SWCNT junction.

In summary, energy spectrum and Franck-Condon couplings strongly depend on the geometry of the junction of suspended SWCNT. In this system, two kinds of couplings arise, plasmon-vibron and charge-vibron couplings. The analysis of the coupling constants K_{nm} and L_m and of the Franck-Condon couplings λ_l on the entire geometrical parameters space allowed us to identify different regimes.

In the short symmetric vibron regime ($\lambda < 1$, $\delta \approx 0$), the charge-vibron component vanishes and the Franck-Condon couplings are extremely small ($|\lambda_m| \approx 10^{-3}$) due to the energy scale separation between the plasmonic and vibronic modes ($\Omega/\omega \gg 1$ and $\hbar\Omega/I \gg 1$) that hinder the plasmon-vibron mixing. The Franck-Condon coupling is position-dependent and is located around the position of the vibron.

In the long vibron regime ($\lambda \gg 1$), the charge-vibron coupling dominates the scenario giving substantially larger Franck-Condon couplings ($|\lambda_m| \approx 1$) and independent of the position as in the simple Anderson-Holstein model. The Franck-Condon couplings are strongly dependent on the relative position of the vibron and the dot, leading to selections rules: for example, only even vibron-plasmon modes can be excited by electron tunneling in a symmetric ($\delta = 0$) long vibron junction, see Fig. 6.6.

In the asymmetric short vibron regime ($\lambda < 1$, $\delta \approx \pm 1/2$), the charge-vibron and plasmon-vibron contribution are of the same order and correspondingly one can distinguish (at least in the higher modes, see Fig. 6.8) the position-dependent contribution due to the plasmon-vibron mixing superimposed to the uniform polaron shift typical of the charge-vibron component of the coupling. In the absence of screening (dimensionless electron-electron interaction strength $g_{c+} = 0.2$), however, the absolute value of the Franck-Condon coupling remains negligibly small compared to the one estimated from the experiments [43–45]. Reasonable values have been obtained in this regime by [89] assuming a very strong screening ($g_{c+} \approx 1$) that essentially removes the energy scale separation between the plasmon modes and the much shorter vibron mode.

Finally, for reasonable values of the nanotube parameters the spectrum of the nanotube is only slightly modified by the electron-vibron coupling thus preserving the high degeneracy of the different vibronic configurations. This, in combination with the sensitive dependence of the tunneling matrix elements on the mode number and on the geometry of the system, also suggests the existence of symmetrically coupled slow channels such as the ones described in [83] and consequently of similar NDC effects in the stability diagrams of a suspended nanotube junction.

The results presented in this chapter were worked out in collaboration with Andrea Donarini, and Milena Grifoni. They were published in
[140] Andrea Donarini, Abdullah Yar and Milena Grifoni, New J. Phys. 14, 023045(2012).

Chapter 7

Conclusions

In this thesis, we studied different characteristic properties of nanoelectromechanical systems. Negative differential conductance (NDC) features, memory effects, and strong Franck-Condon couplings were investigated. In more detail:

In Chapter 1, the general aspects and technological perspectives of nanoelectromechanical systems were introduced. We discussed that due to their novel electronic and mechanical properties, they can serve as ideal candidates for technological applications and fundamental science.

The first part of the thesis has been dedicated to the investigation of electronic transport properties mediated by vibrational modes for a quantum dot system. Specifically:

In Chapter 2, a transport theory of generic interacting quantum dots of nanoelectromechanical systems has been put forward. We started with a short review of quantum dots. The electron-vibron interaction effects on the quantum transport through nanojunction were introduced because the low bias transport is significantly influenced by the presence of strong electron-vibron interaction. In order to study the dynamics of the system, we applied a density matrix approach which starts with the Liouville equation for the total density operator and enables the treatment of degenerate and quasidegenerate states. Afterwards the generalized master equation (GME) coupling diagonal (populations) and off-diagonal (coherences) elements of the generic quantum dot system in the weak tunnel coupling limit was solved. We derived in detail all the essential dynamical factors like population of the many-body states or the current.

In Chapter 3, we analyzed the spectrum and transport properties of a nanostructure where two degenerate or quasidegenerate levels are coupled to several vibronic modes. Our model presented in this chapter can capture features of transport properties of suspended carbon nanotubes and of molecules with a fourfold degenerate electronic level coupled to many vibrational modes. The transport theory is based on vibron-assisted tunneling. The generalized master equation approach was considered for the dynamics of the system taking into account all the degeneracies arising from the electronic level (spin and orbital degeneracies) and vibrational modes. However, the coherences between vibronic degenerate states do not play a significant role in the transport addressed in this work. Despite the fact that we considered a fully symmetric setup, the stability diagram for the differential conductance shows striking negative differential conductance (NDC) features which hints at peculiar features of our nanoelectromechanical system. We showed that NDCs appear due to the slow channels originating from spin and/or orbital degeneracies and the suppression of Franck-Condon channels. With source-drain symmetry being preserved but an asymmetry between orbitally degenerate states being allowed, we could explain the alternating PDC and NDC features observed in Refs. [43] and [45]. Eventually, with the further introduction of the left and right asymmetry suggested in Ref. [89], we confirmed the appearance, also in presence of multimodes, of the NDC lines with the same slope for both positive and negative biases. We also gave an analytical interpretation of the numerical results in the low-bias regime.

In the second part (Chapter 4), the main focus was on the hysteretic switching dynamics of a simple Anderson-Holstein model system where a single level is weakly coupled to two metallic leads with the latter being subject to an adiabatic periodic change of the bias voltage. The quantum dot is also coupled to a vibrational mode. We analyzed in some detail the quantum switching, bistability and memory effects. We showed that the bistability arises if the quantum switching between neutral and charged states involved is suppressed, e.g., due to Franck-Condon blockade. In the case of an asymmetric junction, the neutral and charged states can be unstable at one polarity but stable at the other polarity of bias voltage. Under an appropriate choice of parameters, the stability regions of the two states overlap, which results in a bistable region in a certain interval of bias voltage. Hence, asymmetric voltage drop across the junction and strong enough electron-vibron interaction drives the system to a bistable configuration which is a necessary situation for the hysteretic dynamics of the system. The dynamics of the system was calculated within the framework of a generalized master equation (GME) approach in the weak tunnel coupling limit. The time-dependent solution of the GME was taken into account and important time-scale relations, which essentially govern the switching dynamics, were derived. Taking into account non-stationary effects, in particular the interplay between time scales of variation of the external perturbation and the switching time of the system, we demonstrated electrically controlled hysteretic behavior of the system. Furthermore, we showed that vibronic states and vibron energies also exhibit hysteretic features like the ones shown by the population-voltage and current-voltage curves. At the end, we also discussed the case of a DC-bias. In this case, the population-voltage and current-voltage curves get single valued. Interestingly, one can observe current peaks in the I-V characteristics of the system when given vibronic channels contribute to transport. Moreover, we found that in the AC-case the vibronic excited states can be highly populated, whereas in the stationary case the population of the excited states is strongly decreased.

In the third part of this thesis (Chapters 5 and 6), we analyzed the electronic properties of interacting metallic armchair single wall carbon nanotubes (SWCNTs) in the low energy regime. We briefly presented the physics of noninteracting p_z electrons in SWCNTs. In particular, the finite size effects were properly treated by imposing open boundary conditions. The low energy eigenstates and the spectrum of suspended SWCNTs quantum dots were analyzed in the presence of electron-electron

and electron-vibron interactions. Particularly:
In Chapter 5, we discussed in detail the electronic band structure of graphene and SWCNTs. The low-energy theory of metallic SWCNT was briefly reviewed. We showed that this theory is appropriate in the linear dispersion regime above half-filling where the low-energy physics is most relevant in the “gapless” subband touching at the Fermi Dirac points. The character of the tube, being armchair, zigzag or chiral is entirely captured by the Bloch waves originating from the underlying graphene lattice, and which satisfy boundary conditions appropriate for a given SWCNT class. In particular, for armchair nanotubes the condition that the wave function vanishes at the tube ends naturally requires a mixing of contributions from the two different Dirac points $\pm K_0$ (valley mixing), see Eq. (5.15). This yields the occurrence of pseudo-spin degrees of freedom which we associated with “left” and “right” moving electrons. On the other hand, for zigzag nanotubes the wave function must vanish on one given graphene sublattice at one nanotube end but on the opposite sublattice at the other hand. In this case, not treated here, the valley degrees of freedom is a good quantum number and can be associated again with a pseudo-spin degree of freedom. We also presented the different vibrational modes that strongly influence the transport properties of suspended SWCNTs. It was outlined that the low-energy vibrational excitations of the nanotube can be described in terms of low-energy acoustic modes which are coupled to the electronic degrees of freedom via a deformation potential.
In Chapter 6, We presented a low-energy theory of suspended SWCNTs including several vibronic modes as well as different dot-vibron geometrical configurations. The long-wavelength acoustic-vibron modes were described within an elastic continuum model and the electron-vibron interaction in terms of a deformation potential. We considered the longitudinal stretching mode as it is the most relevant candidate in the low bias regime. Since the deformation potential does not depend on the tube’s chirality, the electron-vibron interaction, Eq. (6.10), can safely be applied to non-armchair carbon nanotubes as well. We derived an effective low-energy Hamiltonian within the framework of a Tomonaga-Luttinger liquid description of the SWCNT where the electron-vibron coupling was separated into a plasmon-vibron and a charge-vibron interaction. The system Hamiltonian was diagonalized via a series of canonical transformations including polaron unitary transformation to obtain the spectrum and Frank-Condon couplings of the system. As a consequence, the low-energy description of the suspended SWCNTs reduced to a set of displaced plasmon-vibron excitations. The tunneling matrix elements between the many-body eigenstates of the system are the product of Franck-Condon factors, one for each plasmon-vibron mode. In the asymmetric short vibron regime, the renormalization of the lowest vibronic mode due to the coupling to the plasmons produces a strongly inhomogeneous Franck Condon coupling in the tunneling matrix elements to the carbon nanotube. Interestingly, the Franck-Condon coupling in suspended SWCNT can be position-dependent and is located around the position of the vibron. Moreover, selection rules for the excitations of different plasmon-vibron modes via electronic tunneling events were analyzed in detail.

Perspectives

In this work, we resolved some issues in nanoelectromechanical systems but still there are many open problems to be addressed in future research:

- The exact description of vibrational effects for arbitrary strength of electron-vibron interaction in determining the transport properties of nanoelectromechanical systems is an open issue, specifically, in the intermediate coupling regime.
- It will be interesting to study the vibrational effects on the dc-current through a carbon nanotube and the switching between different stable modes addressed in Ref. [15].
- So far we have considered the electron-vibron coupling via longitudinal stretching modes associated with the deformation potential, ignoring the one induced by the bond length modifications in suspended SWCNTs. It will be interesting to take into account both and find the electron-vibron interaction effects on transport. This may lead to interesting novel physics.
- In the transport theory of suspended SWCNTs, we have considered only the longitudinal stretching modes. The transport calculations with all possible vibrational modes in suspended carbon nanotube will be a nice step towards connecting with real world experiments.
- The investigation of vibrational effects on the transport properties in the Kondo regime also needs to be addressed.
- Strong enough electron-vibron interaction can drive a system into a superconducting state. This may also be a possible new direction of research.
- One peculiarity of armchair SWCNTs is that the pseudo-spin degrees of freedom are expected to be equally coupled to the source or to the drain leads [71]. In other words, the asymmetry involved in Ref. [85,89] and in Chapter 3 of this thesis to explain some alternating negative-positive differential conductance features as observed, e.g., in Ref. [43] is not present for armchair SWCNT quantum dots. We expect, however, that other SWCNT families could perhaps lead to this asymmetry of the tunnel coupling, whose existence has also been invoked in Ref. [141]. This issue is a matter of future research.
- We have explicitly calculated the Franck-Condon (FC) couplings of suspended SWCNTs in the case of possibly extended source and drain leads. It would be interesting to carry out also the transport calculations taking into account the different geometries described in [140]. It may lead to uncovering new physics in the transport properties of suspended SWCNTs quantum dot systems.

Acknowledgements

I wish to express my immense gratitude to my PhD supervisor Prof. Milena Grifoni for her professional guidance and encouragement throughout this research work. Without her valuable help it would have been almost impossible for me to accomplish this job. I am also grateful to Dr. Andrea Donarini for sharing his excellent knowledge on different aspects of nanoelectromechanical systems. His professional support in analytical and computational part of my PhD work made it possible to complete this task. I acknowledge the valuable help of Georg Begemann and Leonhard Mayrhofer in the numerical calculations regarding the transport part of this work. I thank Sonja Koller, Magdalena Marganska, Bhaskaran Muralidharan, Sergey Smirnov, Johannes Hausinger, Sandra Sobczyk, Johannes Kern, and all other colleagues in our group (AG Grifoni) for having discussions with them on different subjects of my thesis. I thank my former mates Silvia Garelli, Esmerindo Bernardes and the present mates Sandra Sobczyk, Johannes Kern for providing a productive environment in the office. I also thank Dr. D. A. Ryndyk for useful discussion on switching dynamics of NEM based systems. At the end, I would certainly like to acknowledge my family whose best wishes and moral support always strengthened me whenever I felt myself weak and alone being thousands of kilometers away from them.

* * *

I gratefully acknowledge the financial support from HEC under HRD program
through Kohat University of Science & Technology, KPK, Pakistan
and
from DFG under the program GRK 1570.

Bibliography

[1] http://www.zyvex.com/nanotech/feynman.html.

[2] H. Park *et al.*, Nature (London) **417**, 722 (2002).

[3] L. H. Yu and D. Natelson, Nano Lett. **4**, 79 (2004).

[4] X. H. Qiu, G. V. Nazin, and W. Ho, Phys. Rev. Lett. **92**, 206102 (2004).

[5] H. Park *et al.*, Nature (London) **407**, 57 (2000).

[6] R. H. M. Smit *et al.*, Nature (London) **419**, 906 (2000).

[7] E. M. Weig *et al.*, Phys. Rev. Lett. **92**, 046804 (2004).

[8] H. S. Kim, H. Gin, and R. H. Blick, New J. Phys. **12**, 033008 (2010).

[9] A. Eichler *et al.*, Nature Nanotechnology **6**, 339 (2011).

[10] A. H. Safavi-Naeini *et al.*, Phys. Rev. Lett. **108**, 033602 (2012).

[11] K. L. Ekinci and M. Roukes, Rev. Sci. Instrum. **76**, 061101 (2005).

[12] N. Nefedov, J. Phys.: Condens. Matter **21**, 144213 (2009).

[13] M. C. Butler and D. P. Weitekamp, Phys. Rev. A **84**, 063407 (2011).

[14] S. Sengupta, H. S. Solanki, V. Singh, S. Dhara, and M. Deshmukh, Phys. Rev. B **82**, 155432 (2010).

[15] G. A. Steele *et al.*, Science **325**, 1103 (2009).

[16] J. E. Jang *et al.*, Nature Nanotechnology **3**, 26 (2008).

[17] G. Herzberg, *Molecular Spectra and Molecular Structure* (Dover Publ., New York, 1945).

[18] A. Erbe, C. Weiss, W. Zwerger, and R. H. Blick, Phys. Rev. Lett. **87**, 096106 (2001).

[19] J. C. Cuevas and E. Scheer, *Molecular Electronics* (World Scientific Publishing Co. Pte. Ltd., Singapore, 2010).

[20] F. H. L. Koppens *et al.*, Nature **442**, 766 (2006).

[21] J. R. Petta *et al.*, Science **309**, 2180 (2005).

[22] Z. Hua, Z. Xiao-Wei, C. Tuo, and Z. Guang-Hui, Commun. Theor. Phys. **55**, 359 (2011).

[23] C. Iacovita *et al.*, Phys. Rev. Lett. **101**, 116602 (2008).

[24] F. Meier, L. Zhou, J. Wiebe, and R. Wiesendanger, Science **320**, 82 (2008).

[25] D. A. Ryndyk, P. D'Amico, and K. Richter, Phys. Rev. B **81**, 115333 (2010).

[26] G. Binnig, H. Rohrer, C. Gerber, and E. Weibel, Phys. Rev. Lett. **49**, 57 (1982).

[27] F. Chen, J. Hihath, Z. Huang, X. Li, and N. J. Tao, Ann. Rev. Phys. Chem. **58**, 535 (2007).

[28] E. A. Osorio, T. Bjørnholm, J.-M. Lehn, M. Ruben, and H. S. J. van der Zant, J. Phys.: Condens. Matter **20**, 374121 (2008).

[29] H. Park, A. K. L. Lim, A. P. Alivisatos, J. Park, and P. McEuen, App. Phys. Lett. **75**, 301 (1999).

[30] A. Champagne, A. Pasupathy, and D. Ralph, Nano Lett. **5**, 305 (2005).

[31] K. S. Böhler, A. Edtbauer, and E. Scheer, Phys. Rev. B **76**, 125432 (2007).

[32] R. H. M. Smit *et al.*, Nature (London) **419**, 906 (2002).

[33] K. Stokbro, J. Taylor, M. Brandbyge, and G. Hong, p. 117, in Cuniberti *et al.* [142].

[34] A. Di Carlo, A. Pecchia, L. Latessa, T. Frauenheim, and G. Seifert, p. 153, in Cuniberti *et al.* [142].

[35] S. Sanvito and A. Reily Rocha, J. Comput. Theor. Nanosci. **3**, 624 (2006).

[36] G. Stefanucci, S. Kurth, E. K. U. Gross, and A. Rubio, *Molecular and Nano Electronics: Analysis, Design, and Simulation* (Elsevier, Amsterdam, 2006).

[37] Y. Alhassid, Rev. Mod. Phys. **72**, 895 (2000).

[38] G. Ingold and Z. V. Nazarov, *Charge tunneling rates in ultrasmall junctions, in Single charge tunneling* (Plenum Press, New York, 1992).

[39] J. M. Thijssen and H. S. J. v. d. Zant, Phys. Stat. Sol. (b) **245**, 1455 (2008).

[40] H. Yi and C. L. Kane, Phys. Rev. B **53**, 12956 (1995).

[41] I. L. Aleiner, P. W. Brouwer, and L. Glazman, Phys. Rep. **358**, 309 (2002).

[42] S. Amasha *et al.*, Phys. Rev. Lett. **107**, 216804 (2011).

[43] S. Sapmaz, P. Jarillo-Herrero, Y. Blanter, C. Dekker, and H. S. J. v. d. Zant, Phys. Rev. Lett. **96**, 026801 (2006).

[44] A. K. Hüttel, B. Witkamp, M. Leijnse, M. R. Wegewijs, and H. S. J. v. d. Zant, Phys. Rev. Lett. **102**, 225501 (2009).

[45] R. Leturcq *et al.*, Nature Physics **5**, 327 (2009).

[46] E. A. Osorio *et al.*, Adv. Matter. **19**, 281 (2007).

[47] M. L. Roukes, Phys. World **14**, 25 (2001).

[48] A. N. Cleland, *Foundations of Nanoelectronics* (Springer, Berlin, 2002).

[49] M. Blencowe, Phys. Rep. **395**, 159 (2004).

[50] M. Galperin, M. A. Ratner, and A. Nitzan, J. Phys.: Condens. Mattet **19**, 103201 (2007).

[51] D. A. Ryndyk, M. Hartung, and G. Cuniberti, Phys. Rev. B **73**, 045420 (2006).

[52] A. Mitra, I. Aleiner, and A. J. Millis, Phys. Rev. B **69**, 245302 (2004).

[53] T. Mii, S. G. Tikhodeev, and H. Ueba, Phys. Rev. B **68**, 205406 (2003).

[54] M. Galperin, M. A. Ratner, and A. Nitzan, J. Chem. Phys. **121**, 11965 (2004).

[55] M. Galperin, M. A. Ratner, and A. Nitzan, Nano Lett. **4**, 1605 (2004).

[56] G. D. Mahan, *Many-Particle Physics* (Kluwer, New York, 2000).

[57] J. Koch and F. v. Oppen, Phys. Rev. Lett. **94**, 206804 (2005).

[58] J. Koch, F. v. Oppen, and A. V. Andreev, Phys. Rev. B **74**, 205438 (2006).

[59] H. Grabert and M. H. Devoret, *Single Charge Tunneling: Coulomb Blockade Phenomena in Nanostructures* (Plenum Press, New York, 1992).

[60] J. Koch, M. E. Raikh, and F. v. Oppen, Phys. Rev. Lett. **95**, 056801 (2005).

[61] K. C. Nowack and M. R. Wegewijs, aXiv:cond-mat/0506552, unpublished, 2005.

[62] M. Wegewijs and K. C. Nowack, New. J. Phys. **7**, 239 (2005).

[63] A. Perelomov, *Generalized Coherent States and Their Applications* (Springer-Verlag, Berlin, 1986).

[64] M. Brandbyge, J.-L. Mozos, P. Ordejo´n, J. Taylor, and K. Stokbro, Phys. Rev. B **65**, 165401 (2002).

[65] U. Schollwöck, Rev. Mod. Phys. **77**, 259 (2005).

[66] H. Bruus and K. Flensberg, *Many-Body Quantum Theory in Condensed Matter Physics* (Oxford University Press, New York, 2004).

[67] H. Kreuzer, *Nonequilibium Thermodynamics and its Statistical Foundations* (Oxford University Press, New York, 1981).

[68] M. V. Fischetti, Phys. Rev. B **59**, 4901 (1999).

[69] B. Wunsch, M. Braun, J. König, , and D. Pfannkuche, Phys. Rev. B **72**, 205319 (2005).

[70] U. Harbola, M. Esposito, and S. Mukamel, Phys. Rev. B **74**, 235309 (2006).

[71] L. Mayrhofer and M. Grifoni, Phys. Rev. B **74**, 121403(R) (2006).

[72] G. Begemann, D. Darau, A. Donarini, and M. Grifoni, Phys. Rev. B **77**, 201406(R) (2008).

[73] A. Donarini, G. Begemann, and M. Grifoni, Nano Lett. **9**, 2897 (2009).

[74] A. Donarini, M. Grifoni, and K. Richter, Phys. Rev. Lett. **97**, 166801 (2006).

[75] S. Braig and P. W. Brouwer, Phys. Rev. B **71**, 195324 (2005).

[76] M. Braun, J. König, , and J. Martinek, Phys. Rev. B **70**, 195345 (2004).

[77] W. Wetzel, G. E. W. Bauer, and M. Grifoni, Phys. Rev. B **74**, 224406 (2006).

[78] I. Weymann and J. Barnas, Phys. Rev. B **75**, 155308 (2007).

[79] S. Koller, L. Mayrhofer, and M. Grifoni, New J. Phys. **9**, 348 (2007).

[80] R. P. Hornberger, S. Koller, G. Begemann, A. Donarini, and M. Grifoni, Phys. Rev. B **77**, 245313 (2008).

[81] D. Darau, G. Begemann, A. Donarini, and M. Grifoni, Phys. Rev. B **79**, 235404 (2009).

[82] F. Bloch, Phys. Rev. **70**, 460 (1946).

[83] A. Yar, A. Donarini, S. Koller, and M. Grifoni, Phys. Rev. B **84**, 115432 (2011).

[84] G. Begemann, D. Darau, A. Donarini, and M. Grifoni, Phys. Rev. B **77**, 201406 (2008), Erratum: Phys. Rev. B **78**, 089901(E) (2008).

[85] M. G. Schultz, Phys. Rev. B **82**, 155408 (2010).

[86] K. Blum, *Density Matrix Theory and Applications* (Plenum Press, New York, 1996).

[87] L. Mayrhofer, *Spectrum and Transport Properties of interacting Carbon Nanotubes*, Dissertation, Universität Regensburg, 2007.

[88] M. Grifoni and P. Häggi, Phys. Rep. **304**, 229 (1998).

[89] F. Cavaliere, E. Mariani, R. Leturcq, C. Stampfer, and M. Sassetti, Phys. Rev. B **81**, 201303 (R) (2010).

[90] L. Mayrhofer and M. Grifoni, Eur. Phys. J. B **56**, 107 (2007).

[91] M. G. Schultz and F. von Oppen, Phys. Rev. B **80**, 033302 (2009).

[92] A. Donarini, G. Begemann, and M. Grifoni, Phys. Rev. B **82**, 125451 (2010).

[93] W. Izumida and M. Grifoni, New J. Phys. **7**, 244 (2005).

[94] J. Lu *et al.*, Appl. Phys. Lett. **96**, 262107 (2010).

[95] C. P. Collier *et al.*, Science **285**, 391 (1999).

[96] D. I. Gittin, D. Bethell, D. J. Schiffrin, and R. J. Nichols, Nature (London) **408**, 67 (2000).

[97] M. Despont *et al.*, Sensors and Actuators **80**, 100 (2000).

[98] P. D. Amico, D. A. Ryndyk, G. Cuniberti, and K. Richter, New J. Phys. **10**, 085002 (2008).

[99] M. Galperin, M. A. Ratner, and A. Nitzan, Nano Lett. **5**, 125 (2005).

[100] A. Alexandrov, A. M. Bratkovsky, and R. S. Williams, Phys. Rev. B **67**, 075301 (2003).

[101] A. S. Alexandrov and A. M. Bratkovsky, Phys. Rev. B **67**, 235312 (2003), Erratum: Phys. Rev. B **72**, 129901(E) (2005).

[102] D. A. Ryndyk, P. D'Amico, G. Cuniberti, and K. Richter, Phys. Rev. B **78**, 085409 (2008).

[103] D. Mozyrsky, M. B. Hastings, and I. Martin, Phys. Rev. B **73**, 035104 (2006).

[104] S. Datta *et al.*, Phys. Rev. Lett. **79**, 2530 (1997).

[105] A. Donarini, A. Yar, and M. Grifoni, aXiv:cond-mat/1205.4927v1, unpublished, 2012.

[106] R. Saito, G. Dresselhaus, and M. S. Dresselhaus, *Physical Properties of Carbon Nanotubes* (Imperial College Press, London, 1998).

[107] S. Iijima, Nature **354**, 56 (1991).

[108] A. H. Castro-Neto, F. Guinea, N. M. R. Peres, K. S. Novoselov, and A. K. Geim, Rev. Mod. Phys. **81**, 109 (2009).

[109] S. D. Sarma, S. Adam, E. H. Hwang, and E. Rossi, Rev. Mod. Phys. **83**, 407 (2011).

[110] S. Koller, *Spin transport in carbon nanotubes*, Dissertation, Universität Regensburg, 2006.

[111] T. Ando, J. Phys. Soc. Jpn **74**, 777 (2005).

[112] S. Koller, *Spin phenomena and higher order effects in transport across interacting quantum-dots*, Dissertation, Universität Regensburg, 2009.

[113] X. Blase, L. X. Benedict, E. L. Shirley, and S. G. Louie, Phys. Rev. Lett. **72**, 1878 (1994).

[114] R. Egger and A. O. Gogolin, Phys. Rev. Lett. **79**, 5082 (1997).

[115] C. Kane, L. Balents, and M. P. A. Fisher, Phys. Rev. Lett. **79**, 5086 (1997).

[116] L. Mayrhofer and M. Grifoni, Eur. Phys. J. B **63**, 43 (2008).

[117] D. Garcia-Sanchez *et al.*, Nano Lett. **8**, 1399 (2008).

[118] P. Poncharal, Z. L. Wang, D. Ugarte, and W. A. de Heer, Science **283**, 1513 (1999).

[119] B. Babic, J. Furer, S. Sahoo, S. Farhangfar, and C. Schönenberger, Nano Lett. **3**, 1577 (2003).

[120] V. Sazonova *et al.*, Nature (London) **431**, 284 (2004).

[121] J. C. Meyer, M. Paillet, and S. Roth, Science **309**, 1539 (2005).

[122] B. Witkamp, M. Poot, and H. S. J. van der Zant, Nano Lett. **6**, 2904 (2006).

[123] K. Jensen, C. Girit, W. Mickelson, and A. Zettl, Phys. Rev. Lett. **96**, 215503 (2006).

[124] S. T. Purcell, P. Vincent, C. Journet, and V. T. Binh, Phys. Rev. Lett. **89**, 276103 (2002).

[125] B. J. LeRoy, S. G. Lemay, J. Kong, and C. Dekker, Nature (London) **432**, 371 (2004).

[126] A. K. Hüttel, M. Poot, B. Witkamp, and H. S. J. van der Zant, New J. Phys. **10**, 095003 (2008).

[127] K. Flensberg, New J. Phys. **8**, 5 (2006).

[128] E. Mariani and F. von Oppen, Phys. Rev. B **80**, 155411 (2009).

[129] L. M. Woods and G. D. Mahan, Phys. Rev. B **61**, 10651 (2000).

[130] H. Suzuura and T. Ando, Phys. Rev. B **65**, 235412 (2002).

[131] A. D. Martino and R. Egger, Phys. Rev. B **67**, 235418 (2003).

[132] W. A. Harrison, *Solid State Theory* (McGraw-Hill, New York, 1970).

[133] E. Mariani and F. von Oppen, Phys. Rev. Lett. **100**, 076801 (2008), Erratum: Phys. Rev. Lett. **100**, 249901(E) (2008).

[134] Y. Oreg, K. Byczuk, and B. I. Halperin, Phys. Rev. Lett. **85**, 365 (2000).

[135] L. D. Landau and E. M. Lifshitz, *Theory of Elasticity* (Pergamon Press Ltd., Oxford, 1970).

[136] A. Zazunov, D. Feinberg, and T. Martin, Phys. Rev. B **73**, 115405 (2006).

[137] X. Y. Shen, B. Dong, X. L. Lei, and N. J. M. Horing, Phys. Rev. B **76**, 115308 (2007).

[138] S. Braig and K. Flensberg, Phys. Rev. B **68**, 205324 (2003).

[139] N. T. Ziani, G. Piovano, F. Cavaliere, and M. Sassetti, Phys. Rev. B **84**, 155423 (2011).

[140] A. Donarini, A. Yar, and M. Grifoni, New J. Phys. **14**, 023045 (2012).

[141] J. V. Holm *et al.*, Phys. Rev. B **77**, 161406 (2008).

[142] G. Cuniberti, G. Fagas, and K. Richter, editors, *Introducing Molecular Electronics* (Springer, Berlin, 2005).